NTNU
Norwegian University of
Science and Technology

Pile tip deformation caused by obstacles

Menno Maarten Jorna

Wind Energy
Submission date: July 2018
Supervisor: Zhen Gao, IMT
Co-supervisor: Gudmund Eiksund, IMT

Norwegian University of Science and Technology
Department of Marine Technology

Pile tip deformation caused by obstacles

MSc thesis

M.M. Jorna

TU Delft Delft University of Technology

Van Oord Marine ingenuity

NTNU Norwegian University of Science and Technology

PILE TIP DEFORMATION CAUSED BY OBSTACLES

MSc THESIS

As a partial requisite for obtaining the degree of MSc in Offshore and Dredging Engineering at the Delft University of Technology and the MSc in Technology-Wind Energy at the Norwegian University of Science and Technology.

by

M.M. Jorna

at the Delft University of Technology,
July 15, 2018

University supervisors:	Prof. dr. ir. G.R. Eiksund
	Prof. dr. ir. A. Metrikine
	Dr. ir. F. A. Tsouvalas
	Dr. ir. R. Abspoel
Supervisors at Van Oord:	Ir. W. Op den Velde
	Ir. R. van Luiken

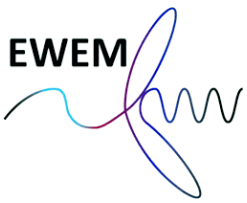

TU Delft Delft University of Technology

Van Oord Marine ingenuity

NTNU Norwegian University of Science and Technology

ABSTRACT

Monopiles will be installed in more difficult terrain since space in the 'ideal' locations is reduced by the rapidly increasing development of wind farms in the ideal areas. In difficult terrain, the amount of obstacles or hard layers increase, leading to an increased risk of pile tip damage. Also the ever increasing D/t ratio of the pile leads to piles more vulnerable to damage to the pile tip. Already, damage to the pile tip was encountered in projects such as the Goodwyn A and Valhall projects, resulting in financial burdens. The design codes show close to zero design guidance regarding pile tip deformation when hard driving is expected. There is a demand for research to understand these deformations at the pile tip. The main goal of this research is to obtain insight in the potential deformations at the pile tip as a result of collision with an obstacle.

To identify the pile tip deformation, a finite element model is established. Six volume elements over the thickness are required at the contact zone to model the pile-boulder interaction accurately. Axial- and lateral soil support is included in the model by using non-linear Winkler springs. Lateral soil support inside the pile is included by transferring the results of a volume element model into linear springs.
A parametric study is performed to investigate the influence of different parameters on damage to the pile tip. It is noticed that a fully geometric- and material nonlinear analyses is required to performs these simulations. Also, it is shown that in contrast with what is frequently done and also mentioned in design standards, the D/t ratio of the pile cannot be used as single parameter to design monopiles. Both D and t should be independently taken into account. Furthermore, it is seen that relatively large pile-boulder contact angles or low steel-rock friction causes the pile to slip over the boulder's surface. Higher friction or smaller contact angles are likely to result in rippling or local in- or outward (local ovalisation) deformation of the wall. Although the larger contact angles and lower friction causes the pile to slip over the boulder's surface, the horizontal reaction is shown to be large enough to push the boulder away, reducing the damage to the tip.

Based on a pile drive-ability analyses it is pointed out that current offshore hydraulic hammers are able to deliver the load that is needed to initiate the investigated local tip damage. Furthermore, based on Terzaghi's bearing formulation and the Brazilian Tensile Test it is demonstrated that local penetration of the pile into the boulder is likely to happen for softer rocks and that splitting the boulder is not likely to occur. Finally, one dynamic simulation is run to compare the static and dynamic simulation. It seems possible to investigate failure mechanisms using statics. Accurate results and propagation should be obtained in dynamic analyses. Detailed dynamic analyses is left for future work.

PREFACE

This MSc thesis is submitted as part of obtaining the master Offshore Engineering and Dredging at the Technical University of Delft (TU Delft) in Delft, the Netherlands, and in Technology-Wind Energy at the Norwegian University of Science and Technology (NTNU) in Trondheim, Norway. Research has been conducted in collaboration with the geotechnical and maritime department at the NTNU, the offshore department at the TU Delft, and the engineering & estimating department at Van Oord in Gorinchem, the Netherlands. Dr.ir. Apostolos Tsouvalas provided weekly supervision at the TU Delft. Also Dr.ir. R. Abspoel and Prof.dr.ir. A. Metrikine were part of the supervision committee at the TU Delft. Prof.dr.ir. Gudmund Eiksund provided supervision at the NTNU and Ir. Wouter Op den Velde together with Ir. R. van Luiken supervised at Van Oord.

I consider myself extremely lucky to be under the supervision of very knowledgeable supervisors. I would first like to thank Van Oord and Ir. Wouter Op den Velde and Ir. R. van Luiken to give me the opportunity to carry out research on pile tip deformations caused by boulders at the engineering & estimating department. Gratitude towards Ir. Wouter Op den Velde for his supervision, opinion and view on the topic. Thank you Ir. R. van Luiken for the meetings that provided me a lot of insight in ANSYS and technical aspects of the topic. Also thank you Sander and Jory, colleagues at Van Oord, they where always ready to answer the questions I asked and open for discussions about a variety of aspects in the topic. Thanks Henno and Vincent for letting me use your laptop overnight to do some ANSYS runs.
Secondly, thank you Dr.ir. Apostolos Tsouvalas for the meetings and the helpful feedback you have provided. Thank you Dr.ir.R. Absoel and Prof.dr.ir. A. Metrikine for the feedback during the progress meetings and being part of the committee.
Lastly, I would like to thank Prof.dr.ir. Gudmund Eiksund at the NTNU. Having your supervision during the specialization project and the MSc thesis gave me a lot of insight in the geotechnical aspects of pile-boulder interaction. You let me think critically about the topic and gave me ideas on how to proceed the research. Moreover, you were always ready to answer questions and this is something I appreciated a lot.

M.M. Jorna
Delft, July 15, 2018

CONTENTS

LIST OF ABBREVIATIONS AND TERMINOLOGY

Abbreviation	Description
EDC	Embedded data collectors
FEM	Finite element method
UCS	Unconfined compression strength

To clarify certain terminology used throughout this research, it should be noticed that the term 'radial' direction indicates the direction normal to the cylindrical wall. The term 'axial' direction is used for the direction along the length of the monopile. Instead of 'axial', sometimes the word 'vertical' is used for the direction along the monopile length.

Furthermore, the term 'static load limit' is used to indicate the asymptotic value at the force-displacement curves in static analyses.

The term 'conservative' is mentioned several times in this report. With conservative a decrease in damage to the pile tip is meant.

The term 'monopile' and 'pile' are used interchangeably.

Finally, 'radius' is mentioned several times in this report. By 'radius', the outer radius is meant.

NOMENCLATURE

Symbol	Description	Units
Greek		
α	Vertical PY division per 1 m	[-]
β	Damage scale	[%]
β	Dimensionless shaft friction factor	[-]
β_{damp}	Rayleigh beta damping	[-]
δ	Deflection	[m]
γ	Unit weight of material	[N/m^3]
ν	Poisson ratio	[-]
ϕ	Soil internal angle of friction	[°]
ρ	Density	[kg/m^3]
σ_t	Tensile strength	[Pa]
σ_y	Yield strength	[Pa]
ζ	Damping ratio	[-]
Roman		
A	Cross section	[m^2]
a	Contact radius in Hertz contact formulation	[m]
c	Wave velocity	[m/s]
D	Diameter of the pile	[m]
D_z	Embedment depth	[m]
E	Youngs modulus	[Pa]
f_e	Eigen-frequency	[Hz]
F	Force	[N]
F_a	Allowable compressive strength	[Pa]
F_{xe}	Elastic local buckling stress	[Pa]
F_{xc}	Inelastic local buckling stress e	[Pa]
F_y	Yield strength	[Pa]
$f(z)$	Unit shaft friction at a depth z	[Pa]
G	Shear modulus	[Pa]
$I_{...}$	Second moment of inertia	[m^4]
j_s	Damping factor	[-]
k	Spring stiffness	[N/m]
L	Length of the pile	[m]
$N_{c,q,\gamma}$	Bearing capacity factors	[-]
p	Lateral resistance of the soil	[N]
$p'_0(z)$	The effective vertical stress at depth z	[Pa]
$p'_{0,tip}$	The effective vertical stress at the pile tip	[Pa]
p_{cr}	Critical Bresse pressure	[Pa]
p_u	Lateral force-displacement	[Pa]
q	The effective vertical stress at depth z	[Pa]
q_u	Unconfined compression strength	Pa
r_i	Inner radius of the pile	[m]
r or r_o	Outer radius of the pile	[m]
R_b	Resistance of the boulder	[N]
S_u	Undrained shear strength	[Pa]
t	Pile wall thickness	[m]
T_p	Pile wave period	[s]

v	Velocity	[m/s]
y	Lateral deflection at depth z	[m]
Z	Impedance of the pile	[N s/m]
Z_{bat}	Batdorf parameter	[-]
z	Depth below the original seafloor	[m]

1

INTRODUCTION

Offshore wind turbines are getting ever bigger, requiring ever larger monopile diameters without the proportional increase in wall thickness. This in-proportional increase in monopile size leads to increasing the D/t ratio leading to weaker piles. Also, all the “good” locations have been taken leading to deeper waters and harder soil conditions for driving the piles. These seabed’s can have significant variations in hardness including obstacles such as boulders or rock inclusions that can provide asymmetric reaction forces on the pile tip during driving.

1.1. BOULDER

A boulder is a rock fragment which exist in all sort of sizes and composition. Men typically speak of boulders when there are relative large rock formations. More precise, boulders are classified in the National Engineering Hanbook (U.S. Department of Agriculture, 2012) as ’very course-grained’ rock of at least 30 cm in diameter. Boulders are usually smooth and round or oval shaped due to a lifetime of exposure to erosion (Figure 1.1). Due to the lifetime of exposure to erosion the strong part is left over and in this study it is assumed that the boulder contain little to no imperfections. Boulders are located in for example the North Sea. Studies (Laban & van der Meer, 2011) show that pieces of rock that differ in size and type from non-native area rock types were found by drilling expeditions in the North Sea. These so called ‘glacial erratics’ vary from large boulders to small pebbles and were carried by glacial ice or were transported by ice rafting during long periods of ice coverage. The latest ice periods are of interest for this research since these sediment layers might interact with the depth range of driven piles. Hence, the older ice periods are not of too much interest due to their deeper located layers. Considering Northwest Europe, the late and middle Pleistocene period are the youngest ice covered periods. The Pleistocene period is characterized by interchanging warm and cold periods. Within the Pleistocene, the Weichsel (116 - 11.7 ka), Saalian (238 - 126 ka), and Elsterian (465-418 ka) are the cold sub-periods were a large part of Northern-Europe was covered with ice. This was shown in a study by Cohen et al (Cohen et al., 2014) and is seen in Figure 1.2. Glacial ice in Northwest Europe led to the presence of boulders in soil sediments.

Figure 1.1: Sandstone erratic found on Mitrahalvøya, Spitsbergen (Landvik et al., 2012)

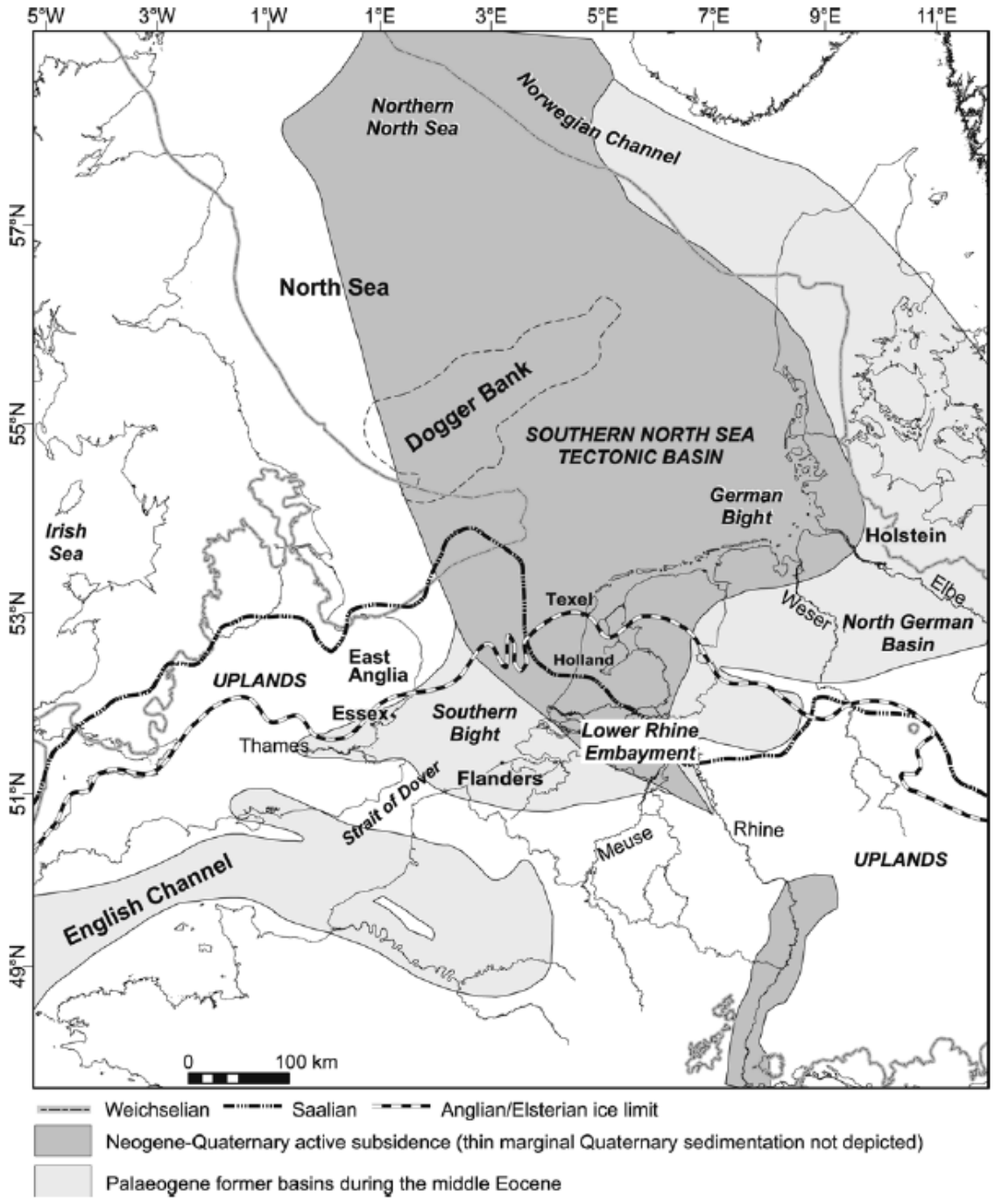

Figure 1.2: Quaternary tectonic and glaciation setting of the North Sea area (Cohen et al., 2014)

1.2. DAMAGE HAS OCCURRED

There are several known projects were damage at the pile tip occurred. During installation of the Goodwyn A platform on the North West Shelf of Australia in 1992, damage at the pile tip was discovered for 15 of the 20 driven piles (Erbrich et al., 2011). These first driven piles appeared to be significantly crushed at 80 meters below seabed (Figure 1.3a). The second case of discovered pile tip damage was reported during installation of the Valhall Water Injection Platform jacket in the North Sea in August 2002 (Alm et al. 2004). Premature pile refusal for five of the eight skirt piles was experienced at approximately 50 meters depth, while the penetration target was approximately 70 meters. After retrieving the piles the pile tips showed inwards collapse, closing the pile toe almost entirely. Another recent example of pile damage was clearly seen when the piles of a quay

wall were removed in Rotterdam in 2017 (Figure 1.3b). The retrieved short piles had a D/t of 75 and most of the tips were closed. D/t ratios larger than 100 are nowadays the standard and it tends to increase even further. These cases highlight the necessity to understand pile tip deformation and to take it into design considerations.

(a) (b)

Figure 1.3: (a) Goodwyn A primary pile collapse details (Erbrich et al., 2011). (b) Removal of a quay wall in Rotterdam (cited by Cathie associates, 2017). Piles driven into dense Pleistocene sand with a D/t of 75.

1.3. MOTIVATION

Excluding the described Goodwyn A, Valhall and Rotterdam projects, piles seemed to be installed successfully. However, this cannot be stated as a fact due to uncertainty about the pile integrity after installation. Whilst there are standard procedures to investigate pile damages during fabrication and handling, investigation of damage to the pile tip during driving is not typically performed. Furthermore, the increasing pile D/t ratios and potential pile-obstacle collision in harder soils motivates the need to understand the potential pile tip deformation and its consequences. This research is performed in this MSc thesis.

1.4. SCOPE AND RESEARCH OBJECTIVE

The main goal of this research is to obtain insight on the potential deformations at the pile tip as a result of collision with an obstacle. The word 'obstacle' is used because this work might as well be applicable to collision with other hard objects or stiff soil layers. In this MSc thesis however, boulders are chosen to represent collision damage and to specify the research. In order to obtain insight in the pile-boulder collision process, the MSc thesis will focus mainly on the numerical model of the pile-boulder interaction. The purpose of the numerical model is to answer the main research question:

What are the potential pile tip deformation mechanisms as a result of collision with an obstacle?

To solve the main research question, three sub-questions are addressed:

1. *What is the influence of pile geometry, obstacle size and position, the steel-rock friction, pile driving loading, and the soil-characteristics on damage to the pile tip?*
2. *Can the pile-boulder interaction be related to failure of the boulder?*
3. *What is the influence of dynamic pile driving on damage to the pile tip?*

1.5. RESEARCH APPROACH

To answer the main research question and sub-questions, four research objectives were set.

1. Understanding the pile driving mechanism and soil-structure interaction by
   - performing literature research on pile driving and soil-structure interaction
2. Understanding different aspects of finite element modelling by
   - working through tutorials in the finite element software ANSYS
   - reading through the ANSYS help environment and consult Van Oord employees
3. Design a static Finite Element model to
   - investigate how to efficiently and as accurate as possible model the pile-obstacle interaction
   - self-verify model aspects (soil springs, etc.)
   - investigate the influence of pile characteristics (geometry, material), soil aspects, driving force, obstacle characteristics (size, position) on damage to the pile tip
4. Set-up a single dynamic pile-boulder FEM simulation to
   - compare dynamic results with static results

1.6. RESEARCH CONSTRAINS

In order to constrain the thesis topic, several condition apply to the problem:

1. The boulder is assumed to be spherical
2. The focus of the MSc thesis is on the structural aspects, not so much on the geotechnical aspects and not at all on risk-management and financial aspects of pile damage
3. The pile is straight and vertically installed, for example a monopile or a tower-structure
4. The pile has an uniform thickness
5. The soil is a uniform medium-dense sand soil and the pile is assumed unplugged
6. The soil is stiff enough for boulder not to move vertically

1.7. OUTLINE

First, the theory behind pile driving is explained and background in boulder detection, size, and shape is provided. Second, potential pile deformations are described and explained. The first chapter ends by describing an approach to model the soil. Failure of the soil and boulder was investigated and discussed in Chapter 3. The initial set-up of the model and correlated modelling aspects are then described in Chapter 4. The static numerical model is investigated in detail in Chapter 5 as this is the main focus of this thesis research. Different parameters are investigated on their influence on pile-boulder interaction. A link between the static numerical model, pile drive-ability in GRLWEAP and failure of the boulder is made in Chapter 6. A dynamic run is finally performed to inspect the impact of a stress-wave on the model and compare the results with the static model. This is described in Chapter 7. Finally, this MSc thesis research is discussed, concluded and several interesting follow-up studies are proposed.

In this study, numerical values are given to either three significant figures or two decimal places as appropriate.

2

THEORETICAL BACKGROUND

2.1. INTRODUCTION

Part of the theoretical background was performed as the literature research during the specialization project at the NTNU. This theory is expanded with the focus on the numerical model.

2.2. PILE DRIVING

The impact of pile driving is recognised as stress waves travelling up and down the pile. Sophisticated numerical models are used in the industry to predict pile driving behaviour. Proper drive-ability studies should be carried out to reduce risk and know what to expect. Unexpected pile driving behaviour might have tremendous financial consequences. It is therefore important to have an understanding of the theory behind pile driving models and behind pile driving in general.

2.2.1. WAVE EQUATION

The one dimensional wave equation has been with us for quite some time. There are different ways to derive the wave equation. A relative simple to grasp derivation of the wave equation is to consider a taut string under tension or a rod and applying Newton's second law. This derivation can be found in many text books. For convenience the derivation of the wave equation for a rod under motion is seen in the appendix, Section A.1. This was derived in the Structural Dynamics course at the TU Delft, (Metrikine & Vrouwenvelder, 2017). The wave equation is shown in Equation 2.1.

$$\frac{\partial^2 u}{\partial x^2} = \frac{1}{c^2}\frac{\partial^2 u}{\partial t^2} \tag{2.1}$$

Where the wave speed for a rod is calculated according to Equation 2.2.

$$c = \sqrt{\frac{E}{\rho}} \tag{2.2}$$

Several important assumptions are made behind the derivation of the wave equation:

- The material is assumed elastic and homogeneous
- There are no body forces acting on the body
- Lateral inertial effects are neglected
- There are no variations in the cross-section
- The stress is uniformly distributed over the rod

This indicates that the wave equation can be applied only for specific theoretical problems that fulfill these assumptions.
Substituting typical values for steel into Equation 2.2, it is seen that waves travel through steel at a speed of approximately 5000 m/s:

$$c = \sqrt{\frac{210\,GPa}{7850\,m/kg^3}} = 5172 \text{ m/s}$$

D'Alembert derived the solution to the wave equation for a linear elastic system in the 18th century and this solution is shown in Equation 2.3.

$$u(x,t) = f(x-ct) + g(x+ct) \tag{2.3}$$

In this solution $f(x-ct)$ represent a wave pulse propagating to the end of the rod, and $g(x+ct)$ represents the reflective pulse from the boundary at the tip of the rod.
The relation between the particle velocity and the stress is formulated in Equation 2.4. This can be easily derived using linear elasticity and taking the derivative of the D'Alambert solution. It can be showed that the particle velocity is different from the wave velocity. For example if $c \approx 5.1 \cdot 10^3$ m/s, $\sigma = 1.0 \cdot 10^9$ N/m^2, and $E = 2.1 \cdot 10^{11}$ N/m^2, this results into a particle velocity of $v \approx 2.4$ m/s.

$$v(x,t) = -\frac{c}{E}\sigma(x,t) \tag{2.4}$$

Considering a pulse travelling to the end of a fixed rod, it can be showed that a compression wave will reflect upwards with the same sign from a fixed end. This means that a compression wave is reflected as compression as well, which causes the stress to double at the fixed boundary. This phenomenon is called 'stress multiplication'. The velocity will reflect as an upward negative velocity. Therefore the velocity will be zero at the boundary. The doubling of the force at a fixed end can produce large forces at the pile toe when driving to hard rock. The initial- and reflective force and velocity pulse on a pile with a fixed-end is seen in Figure 2.1.

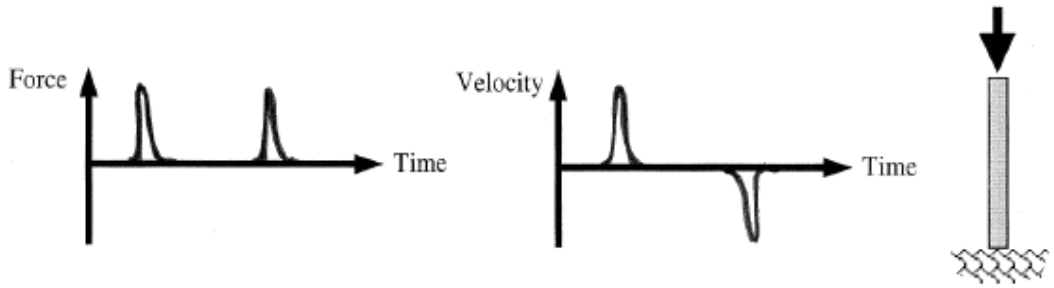

Figure 2.1: Force and velocity time series of a pile with a fixed-end and without soil support. This first pulse represents the initial stress wave and the second the reflective stress wave

Considering an elastic rod, from the stress-strain relationship the force and velocity are linked by the impedance Z of the pile (Equation 2.5).

$$F(t) = \frac{EA}{c}v(t) = Z \cdot v(t) \tag{2.5}$$

The impedance of the pile is an important quantity in pile driving because it is a measure of the way in which a pile transfers force. A high impedance pile can transmit forces with relatively low strains, stresses and velocities. A low impedance pile requires higher strains, stresses and velocities for the same force. Furthermore, if we consider two sections on a monopile, a difference in impedance of the two sections will cause a reflective wave to occur at the junction. Monopiles are typically not uniform and therefore differences in impedance are present. Also splices or defects changes the impedance and the detection of these irregularities are discussed in Section 2.3. The transmitted wave will have the same sign as the incoming stress pulse, however the sign of the reflective wave depends on the impedance ratio of the two sections. If the impedance of the second section is larger than the first one, the stress pulse keeps the sign of the incoming pulse and vice versa. In addition to changes in impedance, also the soil will influence the wave propagation. This is discussed in the next section.
Another frequently used term in the pile driving industry is the pile period T_p formulated in Equation 2.6 (Warrington & Wynn, 2000). In semi-infinite pile theory there are no reflective waves which simplifies the D'Alembert solution. Longer piles show semi-infinite pile behaviour in terms of that the pile is usually hit by another blow before the reflective wave reaches the pile heat. This means that at the top of the pile does not feel large wave activities in the time $2T_p$ which is in engineering known as 2L/c. 2L/c is thus the time that the wave needs to travel from the top of the pile to the tip and back.

$$T_p = \frac{L}{c} \tag{2.6}$$

Where

- T_p is the period of the pile in seconds
- c is the wave speed
- L is the length of the pile

2.2.2. PILE-SOIL INTERACTION

The previous described D'Alembert solution gives insight in wave transmission in a pile. However, this solution is only valid for a linear-elastic system and is not applicable when the interaction of the pile with the soil is taken into account. The soil can be represented by a series of springs and dash-pots. This is seen in Figure 2.2. The stiffness and damping of the soil on the pile are taken into account and they produce two additional terms in the equation of motions (Equation 2.7) which causes the D'Alembert solution to be invalid and causes propagating waves to experience distortion. *The physical phenomenon causing the wave distortion is known as dispersion and plays a major role in the wave theory and its practical applications* (Metrikine & Vrouwenvelder, 2017).

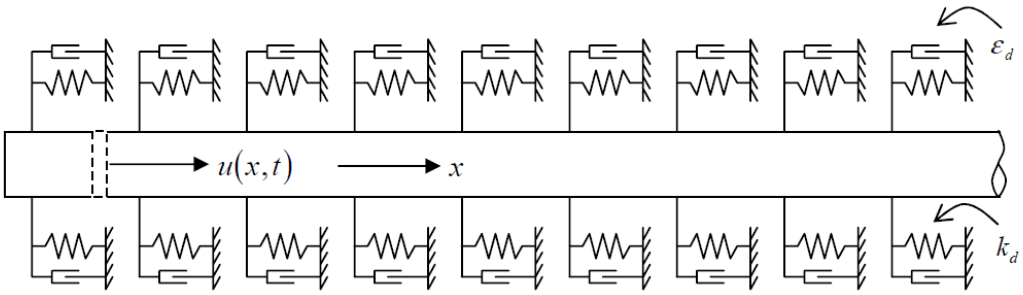

Figure 2.2: Distributed model for pile-soil interaction (Metrikine & Vrouwenvelder, 2017)

Without body forces acting on the rod, the equation of motion is formulated in Equation 2.7.

$$c^2 \frac{\partial^2 u}{\partial x^2} = \frac{\partial^2 u}{\partial t^2} + \frac{k_d}{\rho A} u + \frac{\epsilon_d}{\rho A} \frac{\partial u}{\partial t} \tag{2.7}$$

Where k_d [N/m] is the stiffness of the foundation and ϵ_d the viscosity [N s/m]. By substituting the D'Alambert solution into Equation 2.7 it can be seen that D'Alambert does not satisfy this formulation anymore. Typical force and velocity time series of the initial and reflective wave for one hammer blow are shown in Figure 2.3. It is seen that the force and velocity decrease due to the reflective waves of the soil. If the shaft friction along the pile would be large, the decrease in force and velocity would be less steep and more smoothed since reflections take place all along the shaft pile. It is furthermore seen that the force increases slightly at the time 2L/c, which indicates the reflective wave from the tip. The velocity reflected from the tip is indicated by a larger negative dip at the time 2L/c.

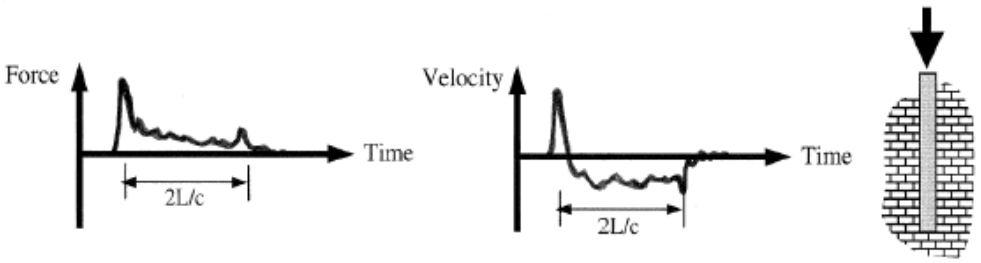

Figure 2.3: Force and velocity time series of a pile with a fixed-end embedded into soil. A decrease in force and velocity is seen due to the reflective waves caused by the soil resistance

Analytical solution to pile driving exist (e.g. Deeks & Randolph, 1993), but in practice more accurate numerical methods are used to predict pile behaviour. A reason for using numerical methods is that it is not easy

to get the damping and stiffness parameters right. This varies per location. Analytical solutions also cannot take important (e.g. non-linearities, non-uniformities) properties into account. Numerical methods are calibrated using real data based on pile driving analyses and experiments. Numerical methods are available in software like GRLWEAP, TTI or TNOWAVE.

2.2.3. PILE DRIVEABILITY ANALYSES IN GRLWEAP

As mentioned, numerical models are used in pile driving analysis. A well known program to perform pile driveability analyses is GRLWEAP by Pile Dynamics Inc. (Pile Dynamics Inc., 2010). In GRLWEAP the soil is represented by elasto-plastic springs and viscous dashpots as was described in previous section. Furthermore, the pile and hammer are modelled by springs and viscous dashpots describing their dynamic interaction. A typical used GRLWEAP model for a hydraulic hammer is shown in Figure 2.4.

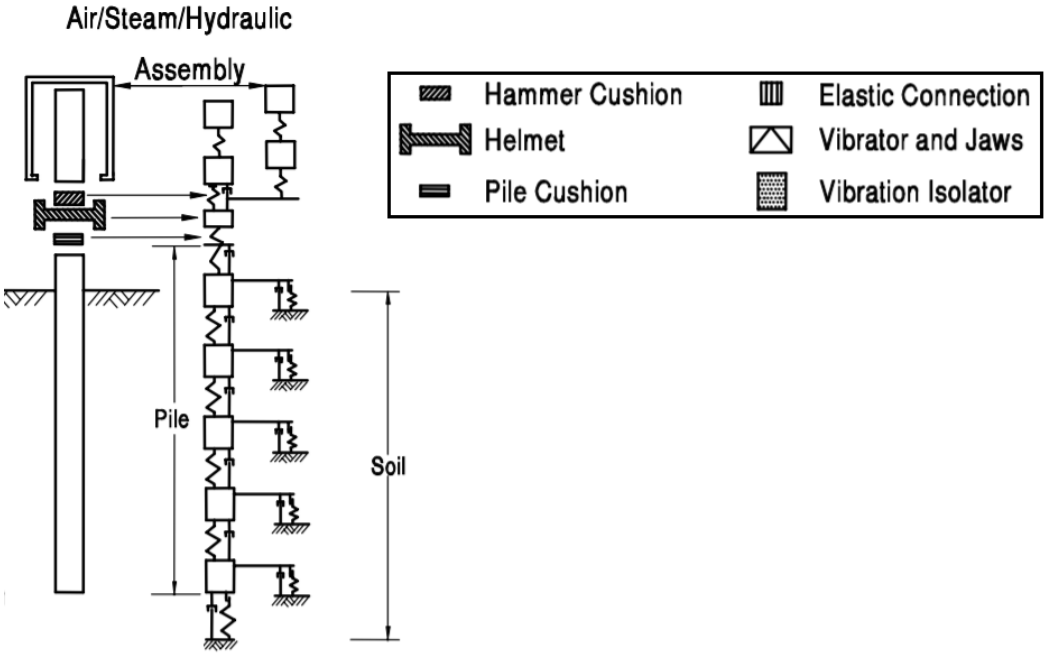

Figure 2.4: Pile-soil model for a hydraulic hammer used in driveability software GRLWEAP (Rausche et al., 2017)

The numerical model is similar as in dynamic pile monitoring (Section 2.3), however the wave input is directly obtained from the hammer instead of the measurements. Also wave matching is not performed since the soil is simply assumed. This introduces uncertainty in the model, as the driveability of the pile is largely dependent on the assumed soil. Based on industry experience, GRLWEAP provides several predetermined soil characteristics for well-known soils, however the user is allowed to characterize their own soil properties. The most important soil input parameters are the quake, damping and resistance values.
The basic required input for all pile driveability analyses software consist of hammer selection, pile geometry and soil type. An appreciated feature of GRLWEAP is that it contains a large database of hammer types which are easy to implement in the model. Pile driveability analyses is performed with maximum stroke, thus maximum energy (taking hammer efficiency into account). In the field the hammer energy is normally lower at the beginning of the driving and increases as the pile penetrates deeper because the soil resistance increases. In pile driveability analyses you need to make sure that the maximum available hammer energy will be enough to get the pile through the soil to the required depth, without refusal. Pile refusal simply means that the impact force of the hammer is insufficient to overcome the driving resistance. In the industry this if often associated with 10 blows per 25 mm. This does not mean that the pile will not refuse in the field. Sometimes our estimation of soil resistance may be wrong, or there is a very high strength soil layer that was previously not detected and then the pile refuses (even with maximum hammer energy).
The numerical model used in GRLWEAP can output velocity and force traces per hammer blow. The force and velocity are related to the hammer energy according to Equation 2.8.

$$E(t) = \int F(t) \cdot v(t) dt \tag{2.8}$$

To get familiar with GRLWEAP, very simplified driveability analyses for different hammer-, pile- and soil-settings were performed. A driveability example is shown in the appendix, Section A.2. Hammer, pile, and soil parameters are specified in the appendix as well. An uniform pile is driven 30 meters into a linear resistance increasing medium dense sand layer and afterwards into 5 meters of uniform limestone (undrained shear strength of 30.0 MPa). From the analyses it is seen that the monopile sinks into the soil the first 12 meters due to its own weight. This sinking phenomenon is typically observed in pile driving projects. The pile is then hammered very easily (≈ 10 blows/min) further into the sand layer. Pile refusal occurs when the pile is driven into the limestone layer. It is seen that the compressive stresses in the pile are very close to the allowable 0.9 f_y compressive strength criteria for steel piles (AASHTO, 2010). GRLWEAP gives values of 9999.0 blow/minute to indicate that pile refusal has occurred. By inspecting the force and velocity curves, it is seen that the reflective force pulse is as large as the initial pulse which indicates that the stress wave is almost entirely reflected by the pile itself and the waves are not dissipated into the soil. This indicates high end bearing of the pile.

2.3. DYNAMIC PILE INTEGRITY TESTING

Damage to the pile toe might be caused by driving piles into for example hard soils or boulders. Also damage along the pile might occur due to initial cracks or other anomalies. It is important to monitor the damage to assess the integrity of piles. Different ways to investigate the integrity of piles are described in this section.
Dynamic pile monitoring is nowadays the main pile integrity test used to assess the structural integrity of the pile and to verify the pile design. Dynamic pile monitoring is performed using a data acquisition system (typical a small computer) connected to the sensors. A schematic for a typical set-up is shown in Figure 2.5a. Pile Dynamic Inc. is nowadays the main provider of dynamic test equipment and their approaches are becoming standard practice in industry. Their pile driving acquisition system is called the Pile Driving Analyzer® (PDA) (Pile Dynamics Inc., 2017) and this term has become the standard when referring to the data acquisition system of dynamic pile monitoring. The PDA is a computer equipped with analysing software which receives data from the sensors and then computes the closed-form solution of the pile-soil-hammer system in real time.
The sensors consist strain gauges and accelerometers. The sensors are typically mounted close to the hammer. A minimum of two strain gauges per pile is needed to compensate for bending. The strain gauges and accelerometers measure respectively the strains and accelerations from the stress waves travelling up and down the pile during driving. An example of the sensors installed on a pile is seen in Figure 2.5b. From the strain measurements and the known stiffness of the pile, the force is calculated. The velocity is obtained by integrating the accelerations. The velocity and force time series are the output for each blow. The velocity and forces are used to obtain the soil resistance to driving (SRD). Typical force and velocity traces were shown in Figure 2.3.

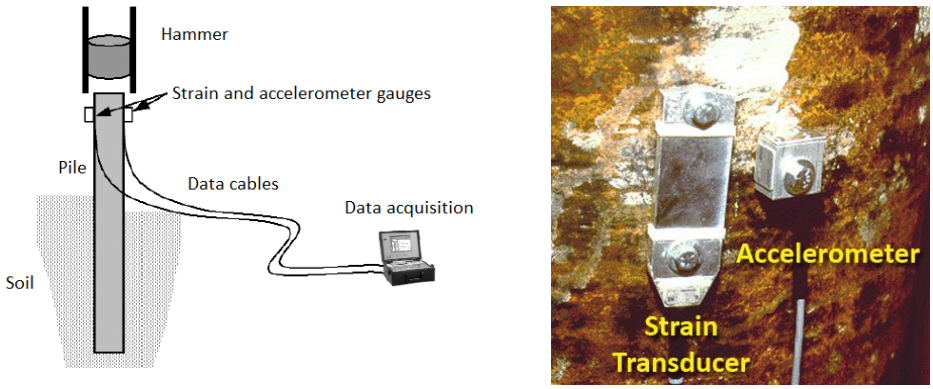

(a) (b)

Figure 2.5: (a) Schematic overview of a typical dynamic pile monitoring set-up. (b) Sensors mounted to monopile (Rausche, 2013).

2.3.1. CAPWAP

A similar numerical pile-soil model used for driveability testing, as was described in Section 2.2.3, is used in dynamic pile monitoring. The hammer is in most cases however not modelled because most of the time we are interested in the pile and soil only. The nowadays most common method of interpreting the informa-

tion obtained from dynamic pile monitoring is another Pile Dynamics Inc. tool called CAPWAP (CAPWAP, 2000), which is short for Case Pile Wave Analysis Program. In CAPWAP, the force-time and velocity time series obtained from the measurements are fed into a wave equation model of the pile. The CAPWAP method is iterative: the model computes a force-time curve at the pile head and compares it with the actual data. The engineer readjusts the model soil parameters and their distribution along the pile until the two force-time histories match. An example of this iteration process is shown in the Appendix, Figure A.5. If failures in the pile are required to be detected, also the pile model can be iterated to match the measured wave data. Again, for a trained engineer this might be a quick process, but if not it might take days to fine-tune the parameters satisfactorily. Finally the soil model is obtained which contains the soil resistance, stresses and movement due to hammer impact.

2.3.2. THE CASE METHOD

Alternatively to CAPWAP, the Case Method is a frequently used method used to compute the total pile resistance based on velocity and force measurements at the pile head (Long et al., 2009). The Case Method is very simplified compared to CAPWAP and therefore less accurate. Benefits of the Case Method is that the pile capacity can be estimated on the back of an envelop and hence is not as computational demanding as CAPWAP. Therefore the Case Method is used a lot for rough estimations and since it is fast to compute, the Case Method is applied during pile driving in real time. The Case Method uses the closed form solution of the wave equation and is based on three assumptions (Vulcan Iron Work Inc., 2017):

- The pile resistance is concentrated at the pile toe
- The static toe resistance is completely plastic
- The dynamic toe resistance is proportional to the velocity of the pile toe, similar as was described in the dynamic soil resistance in Chapter 3

The Case Method equation is formulated in Equation 2.9.

$$R_{tot} = \frac{F_1 + F_2}{2} + Z\frac{V_1 - V_2}{2} \tag{2.9}$$

Where:

- R_{tot} = the total pile resistance [N]
- F_1 = the measured force at time t_1 at the pile head [N]
- F_2 = the measured force at the pile head a period 2L/c later than t_1 [N]
- V_1 = the measured velocity at t_1 at the pile head [m/s]
- V_2 = the measured velocity at the pile head a period 2L/c later than t_1 [m/s]
- Z = the impedance of the pile [N·s/m]

The dynamic component is formulated in Equation 2.10. Here J is the case damping constant [-].

$$R_d = J \cdot (F_1 + Z \cdot V_1 - RTL) \tag{2.10}$$

As was described in Chapter 3, a lot of research is still performed to determine appropriate dynamic damping factors J. Selecting an accurate damping factor is difficult and depends on pile geometry, hammer, and soil characteristics and can be more accurately determined by CAPWAP. The Case Method determines the total pile resistance based on the summation of a static and dynamic resistance component as shown in Equation 2.11.

$$R_{tot} = R_s + R_d \tag{2.11}$$

Equation 2.9, 2.10, and 2.11 lead to the expression for the static resistance as formulated in Equation 2.12.

$$R_s = \frac{F_1 + F_2 + Z(V_1 - V_2)}{2} - J\left(\frac{F_1 - F_2 + Z(V_1 + V_2)}{2}\right) \tag{2.12}$$

There are basically two methods to calculate the Case ultimate capacity: the RMX and RSP method. The only difference between these two methods is the selection of the time t_1. In the RSP method t_1 is the first peak point in the force-time curve. In the RMX method t_1 is the peak initial force plus a time shift, generally 30 msec (Vulcan Iron Work Inc., 2017). The RSP and RMX method are visualized in the Appendix, Figure A.6 and A.7 respectively.

2.3.3. DAMAGE DETECTION

Damage can be detected by the interpretation of test data from PDA measurements. By inspecting the force and velocity trace one can diagnose the driving process, as was described previously. It is possible to obtain anomalies in driving, e.g. cracks or other discontinuities. Damage along the pile can be detected in the force and velocity traces since damage leads to a reflective wave earlier then if the wave would reach the pile tip and travelled back in the the time span of 2L/C. An example is shown in Figure 2.6. A crack is shown at a pile length x, considering the pile top as usual as zero in x-direction. The crack is seen by observing a negative force at time 2x/c caused by the reflective wave. Also the velocity shows an upwards pulse due to same reflective wave.

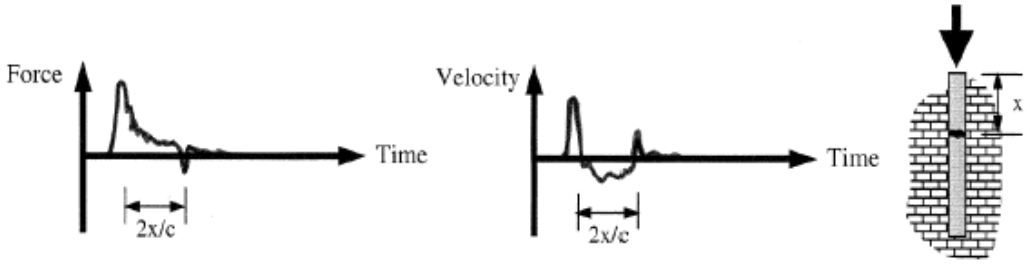

Figure 2.6: Typical force and velocity traces for a pile with an imperfection at the distance x

If at some time before 2L/c a downward force pulse and an upward velocity pulse is detected in the pile monitoring, this is thus a good indicator for indicating damage such as necking, a splice, or a crack. It is furthermore mentioned by Likins et al. (Likins et al., 2014) that damage is generally indicated by a sharp increase in velocity relative to the force at any point earlier than 2L/c.

THE BETA METHOD

The Beta Method was introduced by Rausche and Goble in 1979 and has become the standard in pile damage assessment (Verbeek & Goble, 2012). This method is based on PDA measurements where you basically search for abrupt changes in the stress waves in the 2L/c period, which can be caused by damage to the pile. β is easily derived using 1D wave theory as was described by Rausche and Goble (Rausche & Goble, 1979) and is formulated in Equation 2.13.

$$\beta = \frac{1-\alpha_b}{1+\alpha_b} \tag{2.13}$$

Where α_b is obtained as:

$$\alpha_b = \frac{\mu_\Delta}{2(F_i - R_\Delta)} \tag{2.14}$$

Where:

- μ_Δ= the relative increase of the proportional velocity at the point of damage
- F_i = the impact force
- R_Δ = the resistance force when the relative velocity increase due to the defect becomes noticeable

β is then the indicator of the significance of the damage occurred. β is also referred to as BTA, which is computed in software like CAPWAP. Rausche and Goble (Rausche & Goble, 1979) classified beta on a damage scale which is shown in Table 2.1. The broken pile criteria at a β value of 60 percent is justified by PDA observations that the reflection of the pile toe cannot be observed for values of β less than 60 percent.

Table 2.1: Damage scale (Rausche & Goble, 1979)

BTA, β (%)	**Assessment**
100	No damage
80-99	Slightly damaged
60-79	Damaged
<60	Broken

It it interesting, or perhaps worrying, that the Beta Method is so widely used in industry nowadays. The benefit is that it is a simple, straight forward procedure. The sensors at the top are relatively easy to install and beta factors are automatically computed by data acquisition systems like the Pile Drive Analyzer. There are however disadvantages to the Beta Method. First of all, Rausche and Goble mention in their original report from 1979 that "*There is no experimental proof available justifying the Beta classification, it was set up under the presumption that β actually indicates how much pile cross section is left*". This introduces uncertainty of the validity of the β damage scale. Furthermore, Verbeek and Goble describe that the signals are measured solemnly at the top of the pile and therefore cannot calculate the value of α accurately. Also, if the soil resistance is high and the damage small, the actual damage might be reduced in the results or not seen at all. Besides, the resolution of the equipment plays a role. A typical data sampling frequency of 10,000 Hz is used in dynamic measurements. This gives a resolution in distance to damage location evaluation of 0.2 m (Likins et al., 2014).

PILE TOE DAMAGE

Of special interest in this MSc thesis is the detection of damage at the pile toe caused by boulders. It is mentioned by Likins et al. (Likins et al., 2014) that a major defect near the pile toe is classified as toe damage, although there is no strict definition as to the distance of the damage from the toe. Similar to the previously mentioned damage detection, pile damage at the toe might be detected by a reflective stress wave. The reflective stress wave due to damage at the pile toe should reflect slightly earlier than the toe reflection. This will make it more difficult to detect damage at the pile toe since the damage might be observed as the reflective wave from the pile toe. Careful observation is required to differentiate between them. The velocity and force traces can provide the location of the damage close to the pile toe, however it will not give you information about the extent of the damage.
On the contrary, Likins et al. mention that applying the Beta Method for monitoring damage at the pile toe is likely to be unsuccessful. If the damage is located within a distance above the toe that corresponds to one rise time, the reflection will include tension waves from both damage and pile toe and compression waves from the end bearing plus shaft resistance near the toe. The effects will superimpose which makes it impossible to sort out the three individual components.
Due to the difficulties of detecting damage at the pile toe and the limitations of the Beta Method as was described previously, other methods are being developed to increase the accuracy if pile monitoring. More recently, the Embedded Data Collectors (EDC) (Florida Department of Transportation, 2014) system was developed. EDC uses strain gauges and accelerometers which are installed at the pile top and at the pile toe. This allows to monitor the pile toe directly, instead of interpreting the reflective stress waves at the top of the pile. Consequently, an alternate damage assessment method was developed, the so called Measured Pile Integrity (MPI) method introduced by Smart Structures. Using EDC's, pile damage is detected by measured changes in pre-stress level. This means that tension cracks cannot be observed. In the same study by Likins and al., data from EDC systems installed in multiple driven concrete piles was analysed. Damaged piles were retrieved and where the EDC tests showed clearly that the pile toes were damaged, the Beta Method did not show any damage at all. This clearly shows that the Beta Method is not reliable in assessing pile toe damage and that alternative monitoring systems should be used.

2.4. DETECTION OF OBSTACLES

Essential to the process of determining if pile-obstacle might become a problem is the investigation of the soil. Nowadays, typical soil investigation expeditions consist of cone penetration test (CPT) at the location of each monopile. CPT's are performed by pushing an instrumented cone into the soil. The cone will then provide soil information in terms of certain soil parameters. CPT's, however, are point measurements and do not provide soil characteristics close to the cone. Therefore, these measurements cannot predict the presents of an obstacle right next to the cone. Also drilling expeditions are performed to obtain soil information. These drilling expedition however are usually performed at only a few locations in a wind farm and therefore again cannot predict the presents of an local obstacle. To know the locations and sizes of obstacles in the soil, the complete soil characteristics of the wind farm site should be known. It is not uncommon to perform sonar measurements of the soil bed profile using a ship, however volume measurements inside the soil are not usually performed. The reason behind this is that existing technology is rather new and the measurements are expensive to perform. Inspecting soil volumes by sonar scans is performed by PanGeo Subsea (PanGeo Subsea, 2016). They claim to be able to provide 3D soil images in a 12 m diameter range with a depth up 30 m. The device they designed and use is shown in Figure 2.7. This or similar solutions might be worthy to

incorporate into soil expeditions when the presents of obstacles in the soil is expected.

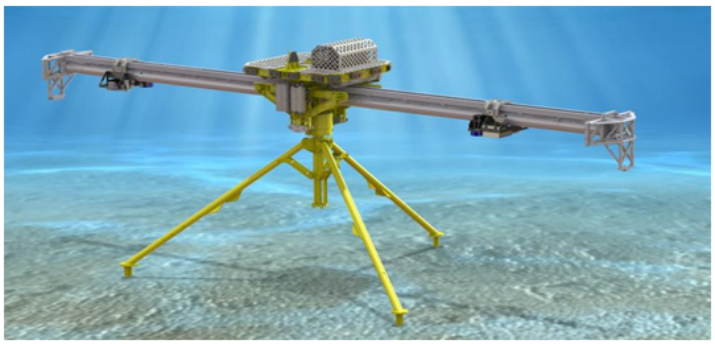

Figure 2.7: Acoustic Corer, a device that uses sound waves to provide 3D soil images in a 12 m diameter range up to 30 m depth (PanGeo Subsea, 2016)

2.5. BOULDER SHAPES AND SIZES

In the introduction it was already mentioned that a boulder is a rock fragment which exist in all sort of sizes and compositions. During a field trip in the province Drenthe in the Netherlands, remainders of old tombs built approximately five-thousand years ago were inspected. These tombs were made out of boulders where the death of the new stone age were buried. The boulders traveled by glaciers from Scandinavia to Drenthe during periods of thousands of years and emerged out of the ice when the glaciers melted. A picture of these boulders is seen in Figure 2.8. It was seen that the boulders were quite smooth which is caused by thousands of years exposed to corrosion. As can be clearly seen in the picture, the shapes and sizes of the boulders varied significantly. Not a single boulder had the same shape or size. The largest measured boulder size was 3.2 m. On-shore boulders like the ones in Drenthe are quite large since they were pushed by glaciers and were not submerged into the soil and hence less prone to severe corrosion. An indication of the offshore boulder sizes is mentioned in an environmental assessment by the British Geological Survey (Balson et al., 2002). It is mentioned that 'boulders do not usually exceed 2 m diameter at the modern seabed'. The difference in shape and size should be taken into account in design consideration.

Figure 2.8: Field trip to boulder formation 'de Hunebedden' in Havelterberg, The Netherlands

2.6. MONOPILE GEOMETRY

As was mentioned in the research constrains, a uniform pile was chosen to be modelled. In reality however, monopiles are build out of cans with different diameters and thicknesses that are welded together. During pile driving these difference in diameter and thicknesses are likely to influence the stresses in the pile. Furthermore, the lowest can of the monopile is usually thicker (D/t of maximum 100) than the other cans to

prevent damage to pile driving. This is referred to as the driving shoe. In further studies it is recommended to take these geometrical deviations along the pile length into account to increase the accurancy of the model.

2.7. PILE TIP DEFORMATION MECHANISMS

In The Recommended Code of Practice for the Planning, Design and Constructing of Fixed Offshore Platforms of the American Petroleum Institute (API RP-2A, 2000) it is written that when 'hard driving' is expected, the wall thickness should be larger than (Equation 2.15):

$$t > 6.35 + \frac{D}{100} \tag{2.15}$$

Where all units are in mm.

This means that when installing a 6.0 m diameter monopile, the recommended minimal wall thickness equals 66,35 mm. This corresponds to a D/t ratio of approximately 90. Nowadays, monopile design in wind parks exceed D/t ratios of 100, which indicates that the standard is exceeded and that in practice there is no design guidance regarding the deformation at the pile tip.
That there is no mythology in the public domain for examining the possibility for pile tip collapse during pile driving is also concluded by HSE (Health and Safety Executive, HSE (2001)). The Recommended Code of Practice for the Planning, Design and Constructing of Fixed Offshore Platforms of the American Petroleum Institute (API RP-2A, 2000) provides D/t guidelines considering local buckling caused by overall pile axial and bending stresses, but does not consider buckling of the tip due to local forces. Also the European standard (EN 1993-1-6, 2007) provides design guidelines for local buckling considering overall axial and bending stresses of the pile, but again does not provide any guidance respect to deformations at the tip.

Possible mechanisms of pile tip deformation during pile driving are listed below and described individually.

1. *Local buckling due to axial loading*
   Classical pile tip local buckling is known as pile tip failure or yielding due to an axial force acting on the entire pile tip that occurs when hitting a hard rock or stratum. For shells this phenomenon is often referred to as shell buckling.
2. *Local buckling due to non-axial loading*
   Inwards and outwards buckling of the pile due to a local force caused by asymmetric loading of pile-tip due to collision with a boulder. This local force will act on a specific section of the pile tip.
3. *Ovalisation of initially imperfect tube under lateral pressure*
   Ovality is the initial out-of-circularity of the pile wall. These ovality imperfection might be included in the fabrication process and ovalisation of tubulars might accumulate when bending stresses are higher than the yield stress. Yield collapse than becomes the critical criterion.
4. *Ring buckling under lateral pressure*
   Ring buckling (also known as circumferential buckling) is known as yielding due to radial pressures. It is expected that ring buckling is not of concern during normal pile driving, since collision with a hard object will not produce pure radial external pressure along the entire wall section and the soil plug will support the small lateral load that might occur.
5. *Column buckling*
   Column buckling (also referred to as global buckling) is the phenomenon of sudden sideways deflection of the pile along its length. Column buckling is not a local failure mode, but a global one, and might occur when hitting a big boulder or stone layer. In this case refusal is likely to occur and this is not of further interest in this thesis. When a small boulder is hit, column buckling is not likely to occur since local failure will dominate the damage initiation. Column buckling might however occur when a boulder is located close to the mud-line and the pile is not laterally supported by the soil.
6. *Denting damage and propagation buckling*
   Progressive yielding of the pile during driving is considered as propagation buckling. An initial imperfection might develop into pile failure due to propagation buckling.
7. *Yielding*
   Potential plastic deformation of the pile when the yield strength of the material is exceeded.

Classical elastic equations can be used for pure axial or shell buckling of a pile. However, the soil response should be taken into account to assess damage to the pile due to pile driving and also for propagation buck-

ling. It should be noticed that several of these deformations could occur simultaneously. Axial buckling together with ring buckling is for example a typical deformation combination.

2.8. SOIL MODELLING

Modelling the behaviour of the soil and its effect on pile deflections correctly is difficult and research is nowadays performed to improve the accuracy of modelling the soil-pile interaction. Different methods exist to model the soil behaviour. For example volume element or discrete springs can be used. Representing the soil by volume elements is an option, but is very time consuming and computational demanding. There are several reasons that lead to the decision to represent the soil by non-linear springs:

- The computational and modelling time of volume elements in not available ans this is also not the focus of this research
- Representing the soil by non-linear springs is the main method in research, industry and also at Van Oord. Due to their experience, results from non-linear springs seem more reliable than from introducing volume elements

As a consequence, the non-linear spring method is considered relevant and this method is described in detail in this section. First the relevant background information is provided.

2.8.1. LATERAL SOIL RESISTANCE

A common approach to model the soil-pile interaction in lateral direction is to collect curves at specific depths that relate the soil resistance to the lateral deflection of the pile, the so called p-y curves, and represent these curves by non-linear Winkler springs. Graphs differ obviously depending on soil type. The soil stiffness value of the soil obtained from the p-y curves is then applied as the stiffness of the spring. The lateral deflection of the pile and the reaction of the soil is seen in Figure 2.9. Figure 2.9(a) shows the pile with a deflection δ_x at depth z_1. Unloaded, there is a uniform distribution of unit stresses normal to the wall of the pile as shown in 2.9(b). When the pile deflects as in Figure 2.9(a), the normal stress distribution looks as shown in Figure 2.9(c). The stresses decreased on the backside and increased at the front of the pile. The displaced soil tries to sort of move around the pile, which introduces shear stresses and normal stresses.

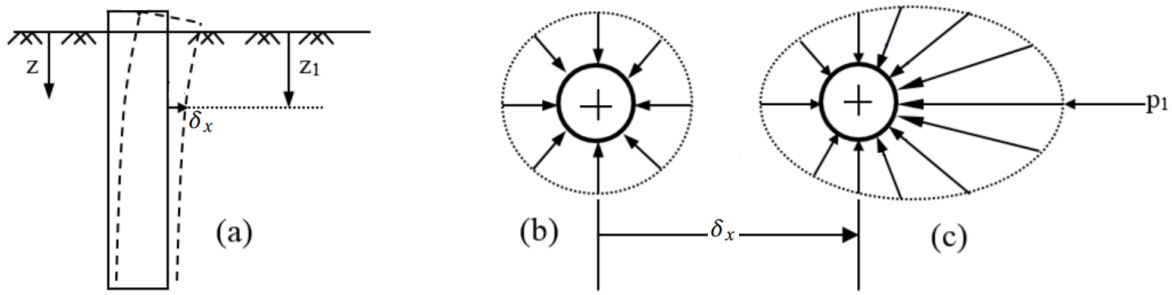

Figure 2.9: Normal stress distribution on a laterally loaded pile

The stresses around the pile are then integrated to obtain the p-y curves. An important assumption here made is that the shear stresses are small compared to the normal stresses and therefore neglected. A general p-y curve is shown in Figure 2.10. On the y-axis is shown the soil resistance per unit length and on the x-axis the pile deflection. Having obtained a p-y curve at a specific depth, the main parameters of interest is the reaction modulus E_{py}, which is obtained by dividing the soil resistance by the deflection. Different reaction modulus can be obtained at points along the p-y curve and used to represent the stiffness of the non-linear spring.

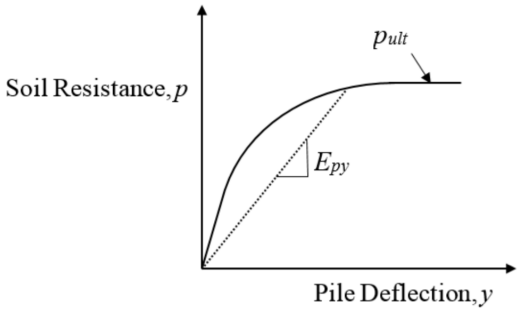

Figure 2.10: General p-y curve defining soil reaction modulus

P-y curves are available for typical soils like sand, stiff- and soft- clays. These typical p-y curves are described in standards, e.g. API (API-R2-GEO, 2011). The is summarized in the Appendix, section C.1. These standardized curves are well calibrated for offshore applications. Non-standardized soils however have to be derived from strain-stress characteristics of the soil.
One should be careful applying p-y curves since obtaining good p-y curves for complex soils can be difficult. Improving the accuracy of p-y curves for different soil types is still being researched nowadays. Limitations of the p-y curves should be considered when modelling the soil with these curves. Potential limitations are described by Ir. M.A. Pando (Pando, 2013).

- Standards do not consider larger pile diameters. Various methods are used in the industry to correct for these larger pile diameters. These corrections are normally based on laboratory tests.
- The continuity of the soil is not modelled using non-linear Winkler springs
- Results are very sensitive to the p-y curves. It is therefore important to obtain accurate p-y curves.
- P-y curves are influenced by several pile related factors as the pile geometry, flexural stiffness, installation conditions, and the type of loading

The consequences of these limitations are that applying p-y curves to your model should be done carefully and results should be validated. Validation can be done by comparing the pile-soil model with real field data.

2.8.2. AXIAL SOIL RESISTANCE

After modelling the lateral soil resistance by p-y curves, a similar approach can be applied to model axial soil resistance. In general we consider three axial load mechanism:

- Shaft friction inside pile
- Shaft friction outside of wall
- Soil end-bearing resistance

These three mechanism are typically modelled using non-linear springs as well. The shaft friction is represented by T-z curves and the end-bearing resistance by Q-z curves. An overview of how a pile can be modelled is shown in Figure 2.11 (J. Hoving, 2017). Again, if good quality curves are available this is good to apply, however one should be careful with more complex soils. Also the complexity of the model increases with applying all these different load mechanism. Furthermore, assumptions are made in this model: eccentric loads are not considered and the pile should be straight.

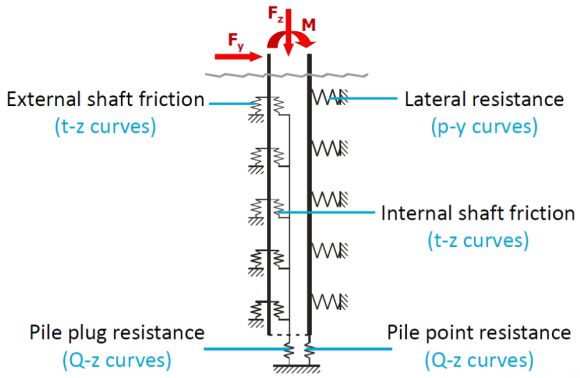

Figure 2.11: Foundation model

In this pile-soil model, the soil is represented by non-linear springs. This can be a good model for a static analysis. If dynamics are considered, the model becomes more complicated. One should account for dynamic effects and this can be done for example by including dash-pots in the model that account for the dynamics. As for P-y curves, T-z and Q-z can be generated according to the standards (API RP-2A, 2000). This is summarized in the Appendix, Section C.2.

PLUGGED VERSUS UNPLUGGED PILES

In modelling it is important to distinguish between plugged and unplugged piles. A plugged pile is considered literally 'plugged', which means that there is soil packed inside the pile that is unable to move. Therefore the resisting load acts on the whole pile tip area and the inside shaft friction disappears. In the unplugged situation the soil inside the pile is able to move and therefore the resisting load acts only on the pile edge. A schematic overview of these two mechanism is seen in Figure 2.12. Typically, piles with a small diameter are prone to plugging due to large inside shaft friction in clays or stiff soils. In this study, large diameter piles are considered and therefore the pile is assumed unplugged.

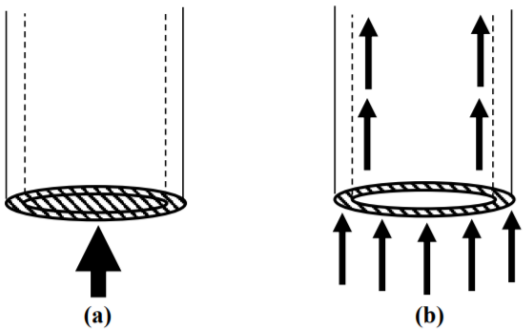

Figure 2.12: Plugged condition (a) and unplugged condition (b)

2.8.3. LATERAL EARTH PRESSURE

Soil exerts lateral load on the structure. This is the so called lateral earth pressure. This pressure is a function of several soil parameters and changes dependent on the movement of the structure. Regarding the structure's movement, three situations may be considered that lead to different lateral pressure distributions.

- The wall does not move. This is called the 'at-rest earth pressure'
- The wall moves away from the soil, hence decreasing the lateral soil pressure. This is called the 'active earth pressure'
- The wall is moved into the soil, thus increasing the lateral soil pressure. In this case, the lateral pressure is called the 'passive earth pressure'

AT-REST EARTH PRESSURE

According the book Principles of Foundation Engineering (Das, 2011), the lateral pressure σ_h at a depth z is equal to (Equation 2.16):

$$\sigma_h = K_0 \cdot \sigma_0' + u \tag{2.16}$$

Where
- u is the pore water pressure [Pa]
- K_0 is the at-rest earth pressure coefficient [-]
- σ_0' is the vertical effective stress [Pa]

The vertical effective stress σ_0' in Equation 2.16 is calculated according to Equation 2.17 and for normal consolidated soils the at-rest earth pressure coefficient is formulated in Equation 2.18. This is an empirical approximation.

$$\sigma_0' = q + \gamma z \tag{2.17}$$

$$K_0 \approx 1 - \sin(\phi') \tag{2.18}$$

Where
- q is a surcharge load at the surface [N/m^2]
- γ is the unit weight of the soil [N/m^3]
- ϕ' is the effective angle of friction of the soil [°]

For overconsolidated soil like stiff glacial till, the at-rest coefficient is formulated in Equation 2.19. Here OCR is the overconsolidation ratio.

$$K_0 = (1 - \sin(\phi') OCR^{\sin(\phi')} \tag{2.19}$$

ACTIVE- AND PASSIVE EARTH PRESSURE

Rankine and Coulomb determined solutions that include the effect of movement of the wall on the lateral soil pressure (Das, 2016). The main difference between Rankine's and Coulomb's solutions is that Coulomb includes the friction of the wall. Including a friction factor increases Coulomb's coefficient. For a zero friction coefficient, Rankine and Coulomb's coefficients converge. Since there are already uncertainties in Coulomb's friction factor and a theoretical uniform soil profile is used in this research, Rankine's method was chosen to be sufficient to model the influence of the the active and passive earth pressure on damage to the pile tip. Rankine's formulation is described briefly.
Besides a smooth wall, Rankine's theory assumes a vertical soil-wall interface. In this case horizontal back-fill is assumed, leading to Rankine's active and passive lateral pressures at a depth z formulated in Equation 2.20 and 2.21 respectively.

$$\sigma_a = \sigma_0' K_a - 2c_u \sqrt{K_a} \tag{2.20}$$

$$\sigma_p = \sigma_0' K_p + 2c_u \sqrt{K_p} \tag{2.21}$$

Where
- c_u is the undrained shear strength of the soil [Pa]
- σ_0' is the vertical effective stress [Pa]
- K_a and K_p are the active- and passive lateral pressure coefficients shown in Equation 2.22 and 2.23 respectively [-]

$$K_a = \tan^2(45 - \frac{\phi}{2}) \tag{2.22}$$

$$K_p = \tan^2(45 + \frac{\phi}{2}) \tag{2.23}$$

3

DISPLACEMENT AND FAILURE OF THE BOULDER

3.1. INTRODUCTION

When the monopile collides with the boulder, there are several possible situations to consider regarding the boulder:

- The boulder is displaced into the soil
- The boulder fails locally at the surface or entirely by tensile fracture (splitting)
- The boulder remains intact and fixed on its position

In the analyses in this research it was initially assumed that the boulder will not fail and that the boulder will not move due to contact with the pile since this will cause damage to the pile tip. In the ideal case however, the boulder or soil would fail before pile failure is initiated. Therefore in this chapter, the ultimate bearing capacity of the soil and failure of the boulder is investigated. Displacing the boulder is investigated in the static model in Section 5.9.

3.2. DISPLACEMENT OF THE BOULDER INTO THE SOIL

In the model it was initially assumed that the boulder is fixed, hence will not move into the soil. This is conservative, since it is likely that the boulder will displace into the soil due to impact of the monopile. This however depends on the boulder geometry, depth, and soil characteristics as is shown in this section. Displacement of the boulder into the soil is due to general shear failure of the soil which occurs when the ultimate bearing capacity q_u of the soil is exceeded. This is valid for a uniform soil. For layered soil types different failure mechanism might occur. Since the boulder is likely to be located in a uniform soil layer, general shear failure is investigated. If pile-boulder collision is initiated and the boulder is displaced into the soil, the reaction force acting on the monopile decreases since part of the energy goes to the displacement of the boulder into the soil. It is thus beneficial for the boulder-pile collision process to displace the boulder. The ultimate bearing capacity of the soil therefore acts as a upper boundary for potential damage to the pile tip. In this section, the ultimate bearing capacity of the boulder into both sand and clay soils is investigated.

3.2.1. PRANDTL AND TERZAGHI'S BEARING CAPACITY THEORY

Prandtl (Prandtl, 1921) published his study in 1921, where the penetration of hard bodies into a softer material was investigated. Thereby plastic deformation of the soil was considered with deformation failure formed into zones as shown in Figure 3.1.

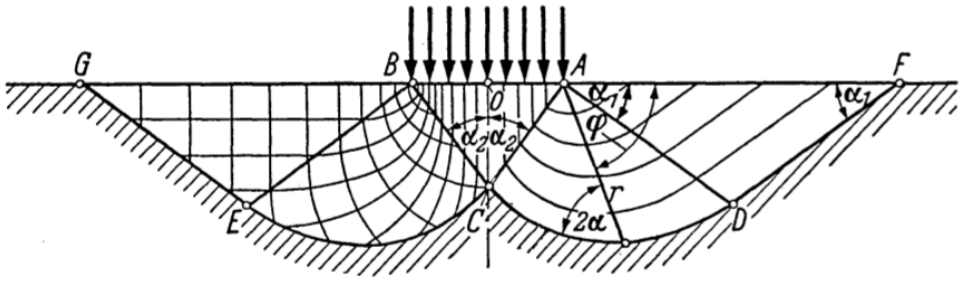

Figure 3.1: Prandtl's (Prandtl, 1921) analysis (summarized by W Trolllmien et al., 1961)

Prandt's formulation is based on the following assumptions (Sitharam, 2013):

- The soil is homogeneous and isotropic
- The soil mass is weightless
- The shear strength of soil can be expressed by Mohr-coulomb equation.
- 2D problem based and a smooth strip footing

Prandtl's formulation of the ultimate soil bearing capacity q_u is shown in Equation 3.1. N_c is the ultimate bearing capacity factor, formulated in Equation 3.2. Here c_u is the undrained shear strength and ϕ the internal angle of friction of the soil.

$$q_u = c_u \cdot N_c \tag{3.1}$$

$$N_c = \cot\phi \cdot (N \cdot e^{\pi \tan\phi} - 1) \tag{3.2}$$

Where

$$N = \frac{1+\sin(\phi)}{1-\sin(\phi)} \tag{3.3}$$

Terzaghi adopted Prandtl's theory (Terzaghi, 1943) for shallow structure foundations. Shallow means depths of about 3-4 times the footing size (Das, 2011). With Terzaghi's theory, the effects of the foundation width and the embedment depth are also taken into account. A schematic of Terzaghi's theory is seen in Figure 3.2. Based on experimental data, Terzaghi included shape factors for different shape of footings (Das, 2011). In this study the assumptions and limitations of this model are described and are not further elaborated in this MSc thesis.

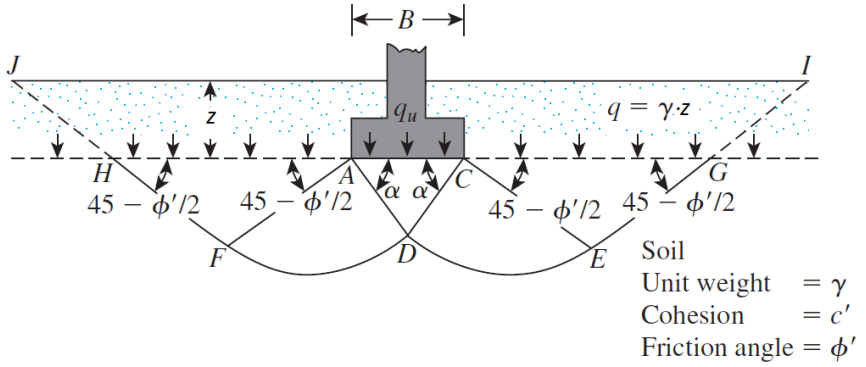

Figure 3.2: Schematic of Terzaghi's bearing capacity theory in soil under a rough rigid strip foundation (Das, 2011)

As seen in Figure 3.2, the failure zone beneath the footing can be separated into three parts:

1. A triangular zone ACD
2. Radial shear zones ADF and CDE
3. Triangular Rankine passive zones AFH and CEG

Note that the angle α in Figure 3.2 is equal to 45-ϕ/2. Furthermore, the shear resistance along line GI and HJ is neglected by replacing the soil above the footing by an effective over burden stress q. Terzaghi's ultimate

bearing capacity for the general shear mode of failure for a circular foundation is given in Equation 3.4.

$$q_u = 1.3 \cdot c_u \cdot N_c + q \cdot N_q + 0.3\gamma \cdot B \cdot N_y \tag{3.4}$$

Where:

- $N_{c,q,y}$ are bearing capacity factors and are function of the soil friction angle ϕ only [-]
- B is the diameter of the circular foundation [m]
- γ is the unit weight of the soil [N/m^3]
- c_u is the undrained shear strength of the soil [Pa]
- q is the effective over burden stress = $\gamma \cdot z$ [Pa]
- z is the depth of the foundation [m]

Terzaghi's bearing capacity factor N_c is equal to the one established by Prandtl (Equation 3.2) and the other bearing capacity factors are formulated in Equation 3.5 and 3.6.

$$N_q = \tan^2(45 + \frac{\phi}{2}) \cdot e^{\pi \tan\phi} \tag{3.5}$$

$$N_\gamma = 2(N_q + 1)\tan\phi \tag{3.6}$$

Terzaghi's theory applies to a flat, circular foundation footing, resulting in shear failure of the soil as shown in Figure 3.2, while the shape of a boulder is assumed to be spherical. However, pushing a flat footing into the soil will cause sand to accumulate in the area below the footing which is then pushed downwards. This process is likely to be very similar as pushing down a spherical shaped footing. Furthermore, a flat footing is seen as a conservative approach compared to a spherical footing. This is justified by that fact that initially, more soil will be displaced around a spherical footing than a flat footing, leading to a higher resistance of the flat footing.

3.2.2. DISPLACEMENT OF THE BOULDER INTO A SAND AND CLAY LAYER

Typical sand and clay soil data is shown in Figure 3.1. For sand, a medium dense sand with a corresponding friction angle ϕ of 35 ° (Das, 2011) was selected together with a submerged unit weight of 10 kN/m^3. For clay, a 100-800 kPA (soft-very stiff) undrained shear strength range was selected with a submerged unit weight of 9 kN/m^3 (according to the NEN 9997-1, 2016). The bearing capacity factors for both soil layers are calculated using Equation 3.2, 3.5, and 3.6.

Table 3.1: Typical sand and clay soil data

Description	Parameter	Value Sand	Value Clay	Unit
Friction angle	ϕ	35	0	°
Bearing capacity factor	N_c	46.12	5.14	-
Bearing capacity factor	N_q	33.30	1	-
Bearing capacity factor	N_γ	45.23	0	-
Submerged unit weight	γ	10	9	kN/m^3
Undrained shear strength	c_u	0	100-800	kPa

Substituting the values for sand seen in Table 3.1 into Equation 3.4, it is seen that the first term drops out since the undrained shear strength is zero. Assuming a boulder diameter equal to one and varying the boulder depth this results into the plot shown in Figure 3.3a. For larger boulder diameters the soil bearing capacity does not increase significant enough to incorporate in this approach. It is seen in Figure 3.3a that by increasing embedment depth of the boulder (second term in the equation) the ultimate bearing capacity of the sand increases linearly. This means that the deeper the boulder is located, the less likely it will displace into the soil.

Substituting the values for clay seen in Table 3.1 into Equation 3.4, it is seen that the third term drops out of the equation since the friction angle of a clay layer is assumed to be equal to zero. It is furthermore seen that the first term (undrained shear strength) is much larger than the second term (effective over burden stress), so the equation can be approximated by Equation 3.7.

$$q_u = 1.3 \cdot c_u \cdot N_c \tag{3.7}$$

When ϕ in Equation 3.2 goes to 0, the limit value of N_c results in $\pi + 2 \approx 5.14$. For stiffer clay layers, the undrained shear strength of the soil increases. Varying the clay undrained shear strength for soft and stiffer clay layers this results into the plot shown in Figure 3.3b.

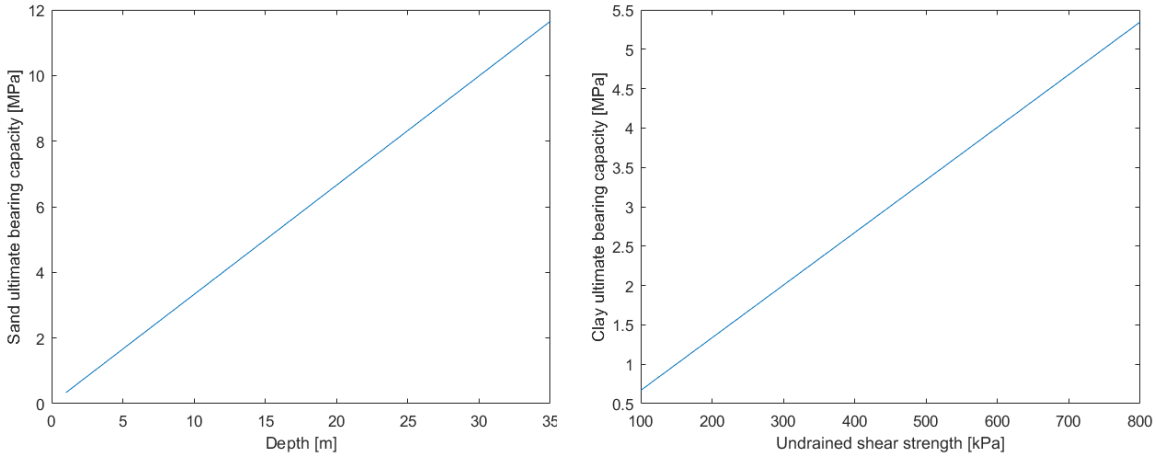

(a) (b)

Figure 3.3: (a) Plot of the soil bearing capacity versus the embedded depth of a boulder of unit diameter in a sand layer. (b) Plot of the soil bearing capacity versus the undrained shear strength of the boulder in a clay layer.

Considering a static approach and applying Equation 3.4 for a pile embedded in a medium-dense sand soil at a depth of 20 m, the ultimate bearing capacity read from figure 3.3a is approximately 6 MPa. Multiplying this by the area of spherical boulder, assuming a diameter of 1 m, this results in static resistance force $R_{b,s}$ of approximately 5 MN. If the force of the pile hitting the boulder exceeds this value, the boulder will penetrate into the soil. The static resistance of the soil is plotted against different boulder sizes and depths in Figure 3.4a.

When dynamics are involved, the dynamic resistance $R_{b,d}$ might be determined by applying Smith's linear model (Smith, 1960). Smith's model is based on the 1D wave equation for piles were the static resistance is modelled by an elasto-plastic spring and a quasi linear dashpot to model the damping resistance. This model was based on pile driving experience and was intended to obtain the dynamic resistance by adding a damping term j_s (correlation factor) to the static resistance. Smith's equation is formulated in Equation 3.8. Here v is the pile driving velocity. Smith proposes a correlation factor of 0.5 s/m for all soil types.

$$R_{b,d} = R_{b,s}(1 + j_s \cdot v) \tag{3.8}$$

Other methods were formulated to include the soil damping in the resistance calculations. Different models were defined by Gibson and Coyle (1968), Case Damping (1976), Heerema(1979) and Litkouhi and Poskitt (1980) as summarised by Barends (Barends, 1992). More detailed research is out of the scope of this MSc thesis.

A plot of the dynamic resistance versus the embedment depth for varying boulder diameters in a medium-dense sand profile shown in Figure 3.4b. The Smith damping j_s is equal to 0.5 s/m and a typical pile driving velocity v of 2.5 m/s was used as input. It is seen that the resistance increases rapidly for increasing diameters and deeper depths of the boulder location. This dynamic resistance should be compared to the force acting on the boulder. This force can be predicted by drive-ability analyses or more accurate obtained from PDA measurements.

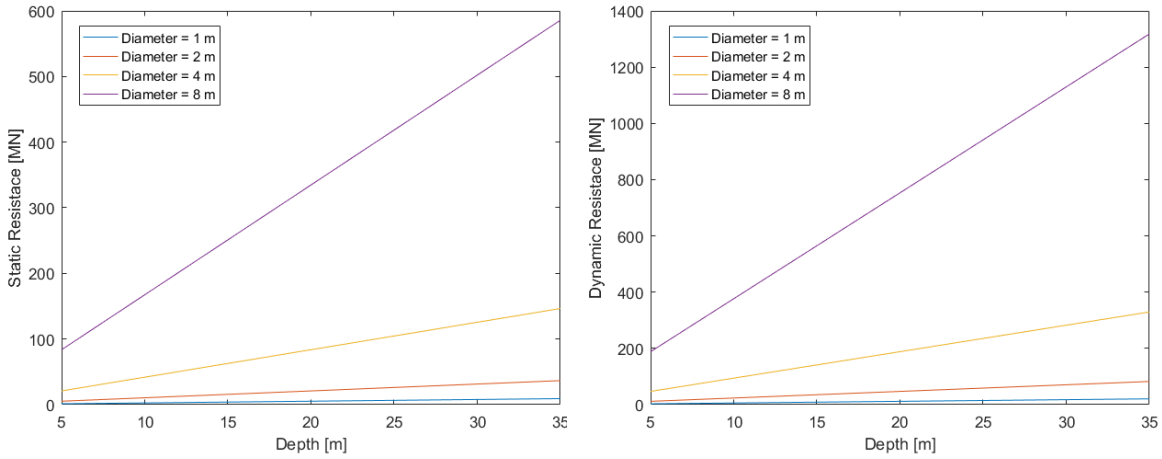

Figure 3.4: (a) Plot of the static resistance versus the embedment depth for different boulder diameters. (b) Plot of the dynamic resistance versus the embedment depth for different boulder diameters in a medium-dense sand profile with characteristics shown in Table 3.1.

A similar approach was performed for the clay layer, which results in a static and dynamic resistance as shown in Figure 3.5a and 3.5b respectively.

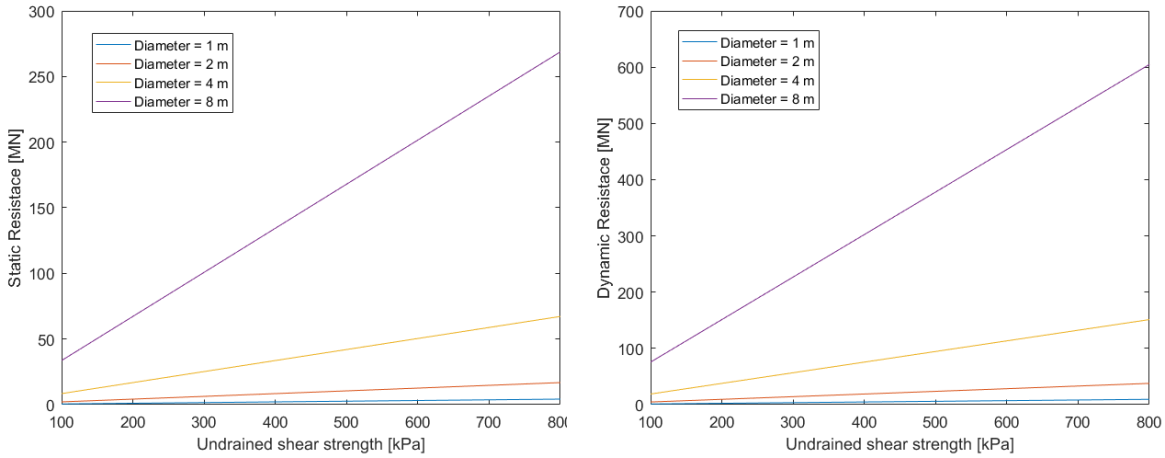

Figure 3.5: (a) Plot of the static resistance versus the undrained shear strength for different boulder diameters. (b) Plot of the dynamic resistance versus the undrained shear strength for different boulder diameters in clay with characteristics shown in Table 3.1.

Comparing the sand and clay ultimate resistance (Figure 3.4 and 3.5) it is seen that the ultimate resistance of clay is generally lower than for sand which indicates that the boulder is easier displaced into a clay layer than a sand layer. Furthermore the dynamic resistance is higher than the static resistance. Also the force acting on the boulder differs in static and dynamic analyses and both cases should therefore be investigated. The dynamic analyses is however likely to be the most realistic simulation with respect to possible pile damage.

3.3. FAILURE OF THE BOULDER

Two types of failure were investigated. First, local failure at the boulder contact surface was investigated using Terzaghi's general shear failure formulation. Second, splitting of the boulder was inspected using the Brazilian test criteria. Failure of the boulder is however a complicated process since boulders vary in shape, size, micro-structure, and are embedded in different sort of soils that influences the dynamic pile-boulder interaction process. Since there is a lot of uncertainty in applying Terzaghi's and the Brazilian test to the dynamic pile pulse hitting the boulder, it should therefore be noticed that these two methods are only applicable to obtain a rough estimation of the forces/stresses required to initiate local failure or cause splitting to the boulder. More detailed boulder failure investigation is out of the scope of this thesis project.

3.3.1. LOCAL FAILURE OF THE BOULDER

Terzaghi's theory considers failure of the medium into several zones. This theory might be applied to rocks as well (Figure 3.6) in order to estimate the kind of force needed to initiate local failure of the boulder. An important strength parameter of rock is the unconfined compression strength (UCS). Recalling Mohr's circle from soil mechanics, the unconfined compression strength is approximately twice the undrained shear strength for a material with stress independent strength. This results in a modification of Equation 3.7 as formulated in Equation 3.9.

$$q_u = 1.3 \cdot N_c \cdot \frac{UCS}{2} \tag{3.9}$$

A typical UCS value for siltstone is 89 MPa (Palmstrom & Singh, 2011) and for the stronger granite 214 MPa (Bewick et al., 2015). Furthermore, the bearing capacity factor for a friction angle of zero is again 5.14 (Table 3.1). Substituting the UCS values into Equation 3.9, this results into the bearing capacity values shown in Table 3.2.

Table 3.2: Parameters used for calculating the bearing capacity based on Terzaghi's equation (Terzaghi, 1943) and the splitting resistance.

	Description	Parameter	Value	Unit
Granite	Unconfined compression strength	UCS	214	MPa
	Bearing capacity	q_u	851	MPa
Sandstone	Unconfined compression strength	UCS	89.0	MPa
	Bearing capacity	q_u	297	MPa
Limestone	Tensile strength	σ_t	38.8	MPa

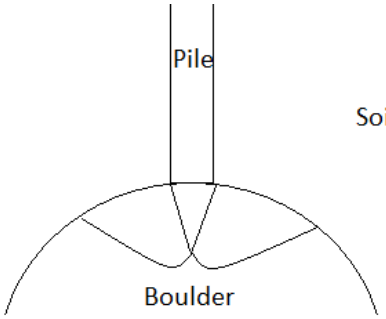

Figure 3.6: Prandtl's and Terzaghi's strip load theory applied to a boulder.

3.3.2. BOULDER SPLITTING RESISTANCE

Beside initiating local failure of the boulder into deformation zones shown in Figure 3.6, brittle splitting of the boulder might occur as a consequence of the compression load working on the boulder. The splitting resistance of the boulder is dominated by the tensile strength of the boulder.

The so called Brazilian test is a well-known and often applied test to determine the tensile strength of concrete and rock. This test consist of a disc-shaped specimen, vertically loaded in compression by two opposite located clamps. The load is continuously increased until failure occurs (Figure 3.7). Failure is assumed to

start at the center and is the result of the uniform tensile stress normal to the splitting diameter (Amadai, 2015). This tensile strength is formulated in Equation 3.10.

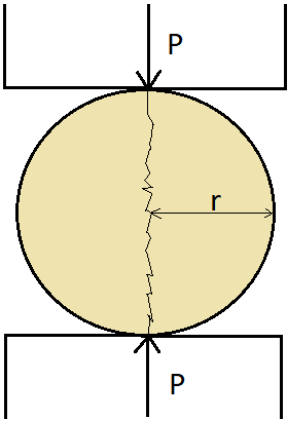

Figure 3.7: The Brazilian test

$$\sigma_t = \frac{P}{\pi \cdot r \cdot t} \tag{3.10}$$

Where

- σ_t is the tension stress [Pa]
- P is the applied line load [N]
- r is the radius of the specimen [m]
- t is the thickness of the specimen over which the load is applied [m]

The tension strength of Limestone equals 38.8 MPa (Amadai, 2015). The highest value of several experiments was selected to be conservative (lower tensile strengths lead to earlier splitting). Earlier splitting is seen as conservative here since this will reduce the initial damage to the pile. The tensile strength of stronger rocks are even larger. The value is also shown in Table 3.2. As mentioned, in the Brazilian test the load is continuously increased until tensile failure occurs. The test is hence applicable for low load rates. Pile driving however consist of high load rates, which leads to different loads required to initiate tensile failure. It is expected that in pile driving, lower loads are needed to cause splitting failure, and therefore applying the Brazilian test to the small load rates results in the numerical model is assumed to be conservative. Furthermore, splitting of a sphere requires a larger load than of a cylinder (disc-shapes) with a line load applied on the same contact area and this contributes to the assumption that the Brazilian test is conservative.

4

INTRODUCTION TO THE MODEL

4.1. INTRODUCTION

The model should be designed in a parametric way in order to run simulations in batch mode and vary parameters easily. The first design process of the model is described in this chapter. Modelling decisions such as mesh type, size and soil spring distributions are related to the design process and are described in this chapter as well.

4.2. PILE-BOULDER CHARACTERISTICS AND BOUNDARY CONDITIONS

A random offshore monopile was selected. This is a monopile used by Van Oord in the Borssele 3 and 4 wind parks to carry a 9.5 MW turbine. Geometrical details of this pile are confidential however the global sizes can be used and are presented in Table 4.1. The characteristics are schematically shown in Figure 4.1a. The bottom 10.0 m of the pile was selected to perform initial calculations in order to save computational time (Figure 4.1b). This means that the boulder is located at 10.0 m depth. Modelling only the embedded part of the pile was justified and discussed in the next 'boundary conditions' section. It should be mentioned that in several simulations the pile was embedded 15.0 m, since this depth was chosen initially and there was not enough computation time available to adapt all depths to 10.0 m. In every paragraph the used length is however clearly mentioned and in comparing different parameters the depth was not changed. By having the length fixed, other parameters could be varied and there influence investigated. Furthermore, the coordinate system used in ANSYS is seen in the figure. The z-axis is along the monopile's length and the centre of the spherical boulder is always located on the y-axis. Node 2 (at the top of the pile above contact point) and node 1 (0.1 m above contact point) are shown as well. These nodes are often used to compare results of the simulations.

Table 4.1: Pile characteristics

Description	Parameter	Value	Unit
Outer diameter	D	7.40	m
Wall thickness	t	0.074	m
Length	L	78.50	m
Embedment depth	D_z	29.25	m

Table 4.2: Material properties of S355NL/ML steel

Description	Parameter	Value	Unit
Density	ρ	7850	kg/m^3
Yield strength	σ_y	317	MPa
Youngs modulus	E	210	GPa
Shear modulus	G	80.8	GPa
Poisson's ratio	ν	0.3	[-]

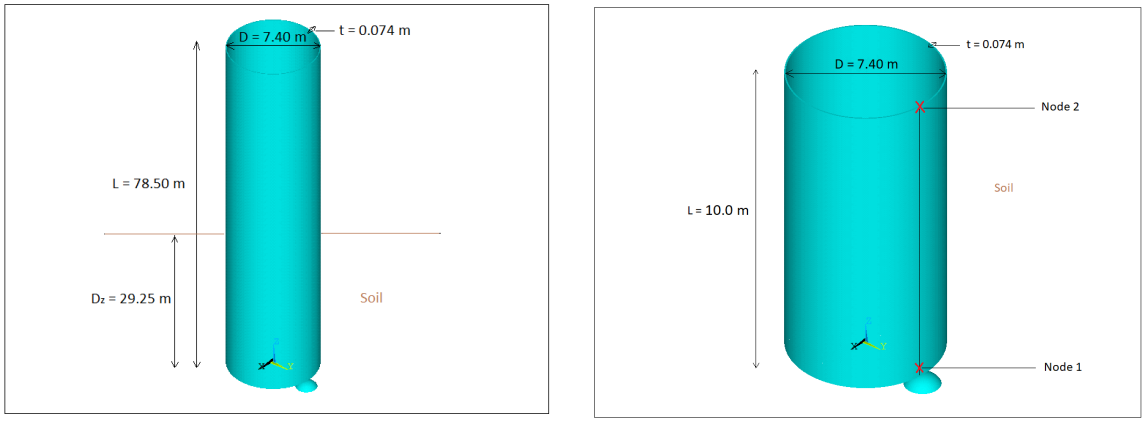

(a) (b)

Figure 4.1: (a) Full size monopile geometry and coordinate system. (b) Modelled 10.0 m monopile geometry

A common used material type for monopiles is S355-steel. Properties of S355-steel are shown in Table 4.2 (EN 1993-1-5 (2006) and DNV-RP-C208, 2016)). Furthermore, for material non-linear analyses the stress-strain curve of S355-steel should be considered. This curve is described in the DNV (DNV-RP-C208, 2016) and for a wall thickness between 63 and 100 mm the curve is plotted in Figure 4.2. Here the elastic part, yielding, and strain hardening of the steel can be clearly distinguished. This data is shown in more detail in the appendix (Figure B.1). It is important to notice that the yield stress reduces for increasing thicknesses.

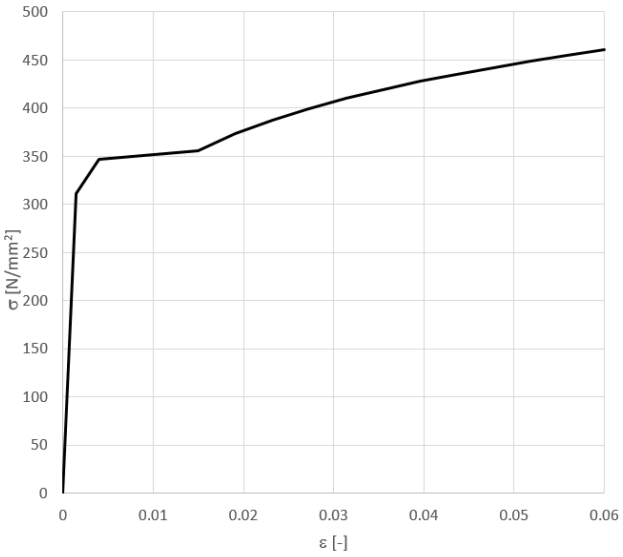

Figure 4.2: S355-steel stress-strain curve (DNV-RP-C208, 2016)

Typical strength parameters of granite (University College London, 2018) shown in Table 4.3 were applied to the boulder and a friction coefficient of 0.5 was used (described in Section 5.7). Granite was selected because its high stiffness properties compared to other other rock types. A high stiffness is conservative since rocks of lower stiffness are likely to absorb more pile driving energy, resulting in less deformation of the monopile.

Table 4.3: Boulder's standard characteristics used in simulations

Description	Value	Unit
Boulder diameter	2.00	m
Young's modulus of boulder	50	GPa
Poisson ratio of boulder	0.3	[-]
Friction coefficient steel-rock	0.5	[-]

4.2.1. BOUNDARY CONDITIONS

In the model the boulder is initially assumed to be fixed. Therefore all degrees of freedom at the bottom of the half modelled boulder were fixed such that the boulder was not allowed to translate or rotate. Including lateral and axial soil support in the model restrains the movement of the pile and these extra boundary conditions from the soil are necessary to stabilize the solution and find equilibrium.
The first reason that justifies the decision to model only the embedded part of the pile is that the vertical component of the stress at the top of the 10.0 m pile was shown to be uniform (Figure 4.3a). This indicates that the stress peak developed at the contact zone is not influenced by the top of the pile and hence the selected 10.0 m is long enough. Second, by constraining the horizontal degrees of freedom at the top of the pile, the pile is not able to rotate at its top as a result of the asymmetric reaction caused by the boulder at the bottom. A few simulations were performed with model parameters defined and described in the next chapter. In this section the goal is simply to show that statically, modelling the embedded part of the pile is sufficient to capture the local deformation initiation. Running a simulation with the full pile and the 10.0 m model pile, this resulted in the same local behaviour at the pile-boulder contact area, as is seen by a plot of the radial displacement at the contact area for both models in the Appendix, Figure E.9. The maximum radial displacement for the full and 10.0 m model read 60.3 and 54.8 mm respectively and hence the values are close. Finally, also by expecting the applied load versus the axial displacement (hence the global response of the system) of node 2 in Figure 4.4, also the global response of both models match very closely (blue and red line). Since the local and global displacement and stress was shown to match, the approach to model just the embedded part of the pile is justified.

Fixating the rotation at the top of the pile is probably accurate during the first few blows when the gripper prevents the pile from moving in horizontal direction. In reality however, the gripper is removed after the first few blows and by initiating contact with the boulder the pile might rotate a little and hence the horizontal fixed boundary condition at the top of the pile should not be present. Furthermore, constraining the top means that the shape of the pile at the top is fixed and this might also influence the shape of the pile along the pile. This is another reason to question the accuracy of constraining the top of the pile in horizontal direction. By running simulations for the pile only supported by the soil and hence free at the top, this resulted in the local responses shown in the Appendix in Figure E.10 and the global axial displacement shown in Figure 4.4 by the yellow and purple curves. By comparing the local deformation it was seen that at the same applied load of 28.5 MN, the radial displacement for the 10.0 m model and full model were 149 mm and 96.4 mm respectively. The local deformation shape seems similar, however from the values it can be concluded that the free rotation of the top of the pile does influence the local results. Globally however, the force versus the axial displacement curves match quite well as is seen by the purple and yellow curve in Figure 4.4. When you compare all the lines in Figure 4.4 it is seen that the curves are very similar, indicating that the boundary condition at the top does not matter much considering the global response of the pile. For the 10.0 m model, the horizontal displacement at the top of the pile was outputted for different pile-boulder contact angles runs and this result is seen in Table 4.4. This model was ran for lateral soil support included outside the pile. It was obtained that at the top of the 10.0 m modelled pile, the axial displacement is approximately constant for all the runs and this indicates that the 10.0 m model can be used to compare and investigate different model parameters. To conclude, due to the questionable assumption of the horizontally fixed boundary condition at the top of the pile, this boundary condition was not applied to the model and therefore in the following simulations the pile is only supported laterally and axially by the soil. It should be noticed that the local responses at the contact area that are obtained in the next chapter might be slightly different than for the full pile due to the difference in rotation caused by the smaller length of the pile. However, it was seen that for different contact angles the displacement at the top of the 10.0 m model is similar and this indicates that the 10.0 m model can be used to investigate in detail. It should be noticed that the rotation of the pile caused by the local pile-boulder collision is really a static phenomenon. For the dynamic simulation discussed in

Chapter 7 it was seen that this rotation of the top of the pile does not happen (Appendix, Figure E.14b).

Table 4.4: Axial displacement at top for different pile-boulder contact angles (Section 4.5). In this run the force applied to the pile was 13.5 MN, the friction 0.5 and lateral soil support was included outside the pile.

Contact angle [°]	-20	-10	10	20
Axial displacement top [mm]	21.3	21.2	21.2	21.5

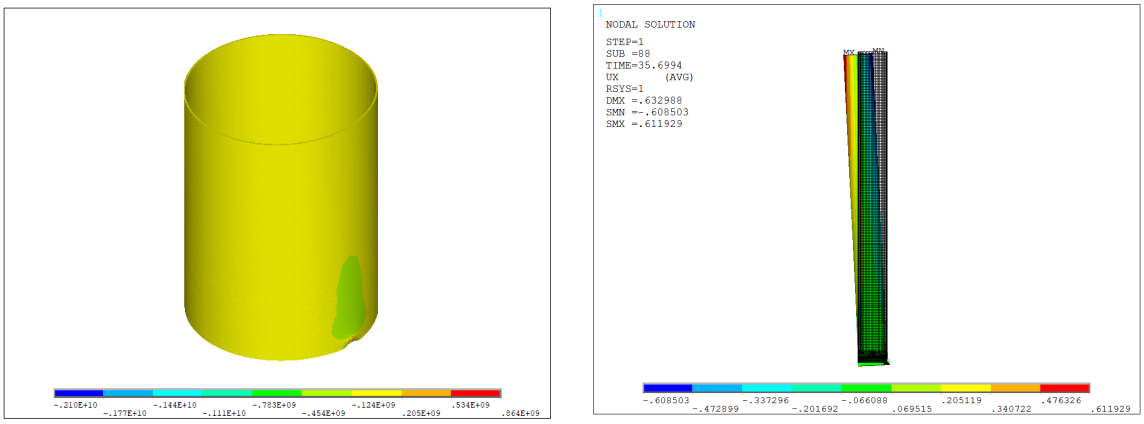

(a) (b)

Figure 4.3: (a) Stress component in axial (vertical) direction for the 10.0 m modelled pile. (b) Rotation of the full pile model is allowed since the boundary at the top of the pile is free. In (a) and (b) the steel-rock friction coefficient is 0.3, $\alpha_{contact} = -10°$, boulder diameter = 2.0 m, and lateral and axial soil support is included in- and outside the pile.

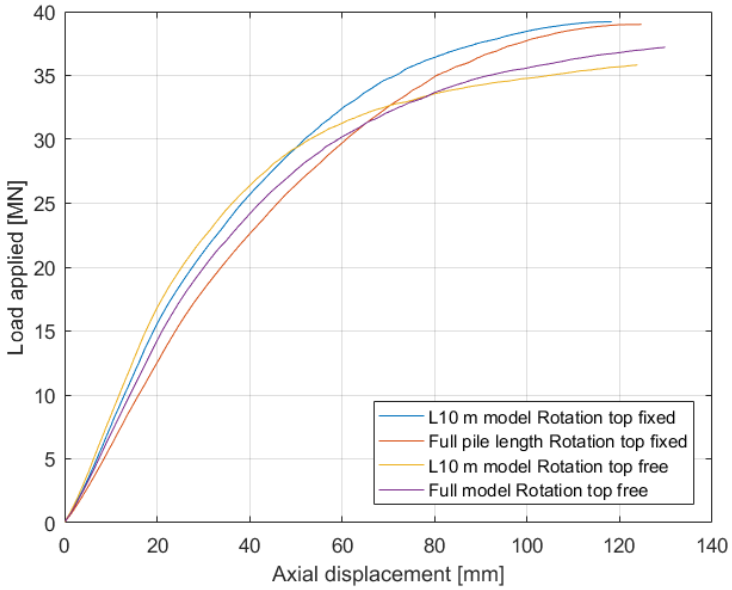

Figure 4.4: Plot of the applied load at the top of the pile versus the axial displacement at Node 2 for the full pile (red) and 10 m modelled pile (blue) for the fixed rotation at the top of the pile and for the full pile (purple) and 10 m pile (yellow) when the top of the pile is free to rotate. Steel-rock friction coefficient is 0.3, boulder diameter = 2.0 m, $\alpha_{contact} = -10°$, and lateral and axial soil support is included in- and outside the pile.

4.3. ELEMENT TYPE AND MESH SIZE

It is important to determine the element type that should be used in the model. For modelling the contact between a monopile and a boulder there are basically two type of element that are likely to be suitable. These are the higher order shell (based on Mindlin-Reissner plate theory) element (Shell281 in ANSYS) as shown in Figure 4.5a and the higher order solid (also referred to as brick,) element (Solid186 in ANSYS) shown in Figure 4.5b. Higher order elements are required since linear elements might experience shear locking in bending modes and these bending modes will occur in collision of the monopile with a boulder. Shear locking is the phenomenon that occurs when the linear elements cannot accurately represent the curvature under bending, introducing an shear stress. This makes the element appears stiffer than it is and this leads to smaller displacements then is they should be the case. As seen in Figure 4.5 the higher order shell element uses 8 nodes, whereas the solid element uses 20 nodes. The main reason to favor shell elements over solid elements is that the computational time of the solution hugely decreases. Furthermore, shells are usually meshed easier, have less problems with stability, and require less disk space than for a model consisting solid elements. However, solid elements might represent the stress over the thickness more accurate and are usually preferred for modelling thick structures. Since the thickness of the monopile is considered thin compared to its diameter and length, shells will probably be accurate enough to model the deformation behaviour of the monopile. For clarification reasons, the higher order shell and solid elements will be referred to as 'shell elements' and 'solid elements' respectively.

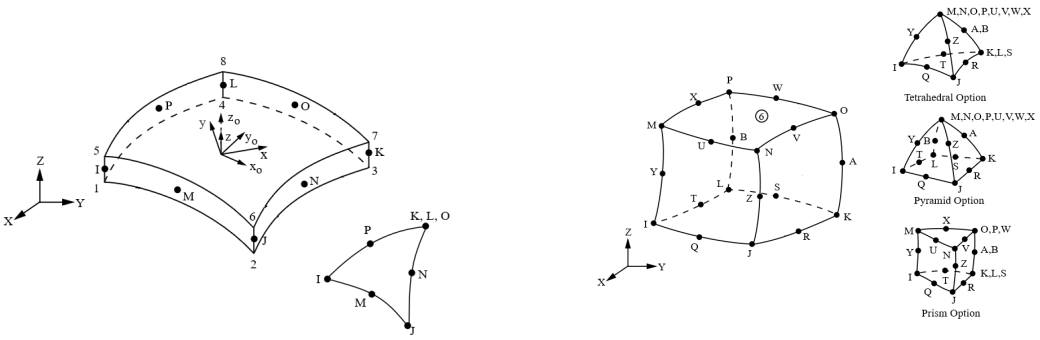

(a) (b)

Figure 4.5: (a) Higher order shell element. (b) Higher order solid element (ANSYS Inc., 2017).

A comparison between a monopile modelled with shell and solid elements was performed. The pile dimensions and material properties mentioned in Table 4.1 and 4.2 respectively were used. The length of the pile was set equal to 15 m.

4.3.1. AN AXIAL COMPRESSED CYLINDER

First, the monopile was axial compressed at both ends by applying a displacement at the top and bottom boundary of the cylinder in opposite direction. First a mesh convergence test was performed for both shell and solid elements. For both solid and shell models the element area was decreased in specified steps shown in Table 4.5. For the solid model, two elements were used over the thickness since increasing the elements over the thickness did not further improve the results. Disregarding the boundary effects, a plot of the axial-component of the stress and the first linear buckling load for the solid element cylinder is seen in Figure 4.6a and 4.6b respectively. The numbers shown on the x-axis represent the column number of the mesh size Table 4.5.

Table 4.5: Mesh size refinement steps

Mesh size length equal to width							
3	2	1	0.6	0.4	0.3	0.2	0.1

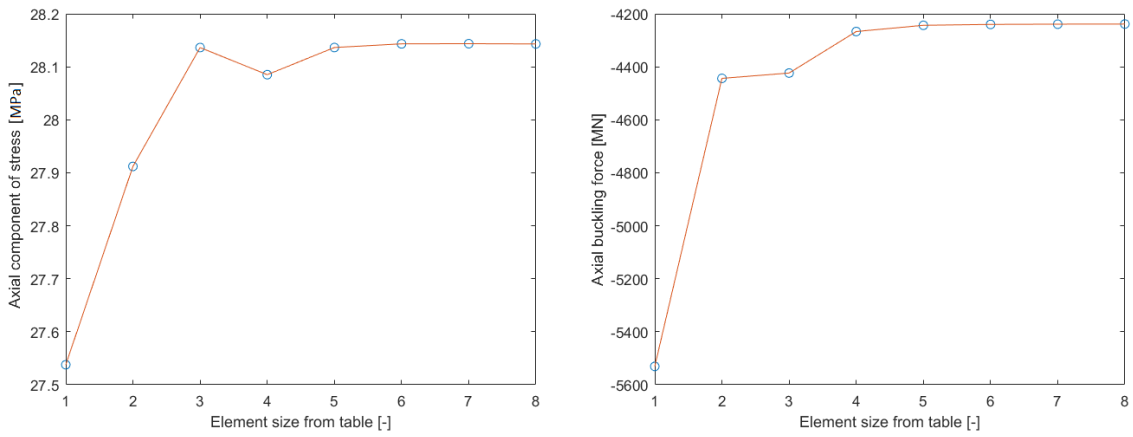

(a) (b)

Figure 4.6: (a) Maximum axial component of the stress versus the element size. (b) First linear buckling mode versus the element size. Both figures are results for a cylinder modelled with solid elements

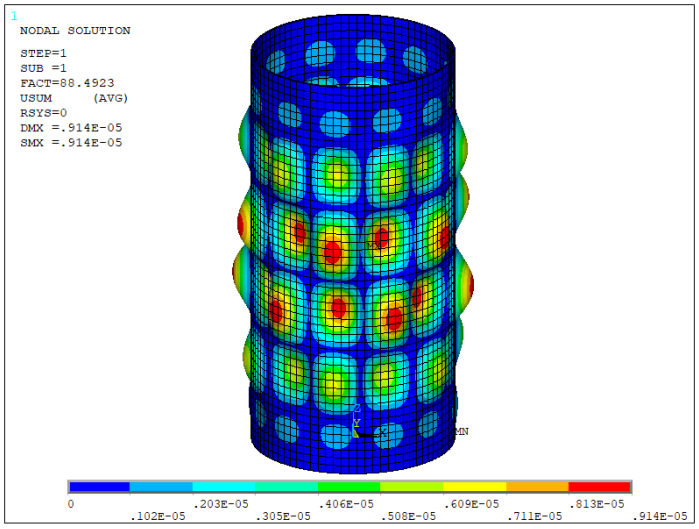

Figure 4.7: Scaled plot of the first buckling mode for a axial compressed cylinder with higher order solid elements.

A similar mesh convergence check was performed for the cylinder modelled with shell elements. For both solid and shell model the results were determined to be converged sufficiently at step six (mesh size of 0.3x0.3). It was seen that a smaller mesh size step only increases the accuracy of the shell buckling values by 0.027 and the solid by 0.022 percent and the stresses even less. A summary of the converged values is shown in Table 4.6.

Table 4.6: FEM results of an axial compressed shell and cylinder

Axial compressed cylinder FEM results			
	Axial-component stress [MPa]	1st linear buckling value [MN]	Computational time [s]
FEM Shell	28.13	4227	14
FEM Solid	28.14	4240	40

The linear buckling value from ANSYS was compared to theoretical linear buckling values. Expression for linear buckling values of axial compressed cylinders of intermediate length ($L/r > 0.75$) were formulated by the National Advisory Committee for Aeronautics (Batdorf et al., 1947) and clearly derived in the course TMR4205

at the NTNU (J. Amdahl, 2005). The theoretical linear buckling stress for an axial compressed cylinder of intermediate length is seen in Equation 4.1.

$$\sigma_{crit} = \frac{\pi^2 E}{12(1-\nu)^2}(\frac{t}{l})^2 \cdot \frac{4\sqrt{3}}{\pi^2} Z_{bat} \tag{4.1}$$

Where Z_{bat} is the Batdorf parameter shown in Equation 4.2.

$$Z_{bat} = \frac{l^2}{r \cdot t}\sqrt{(1-\nu^2} \tag{4.2}$$

Substituting the geometrical and material parameters shown in Table 4.1 and 4.2 in Equations 4.1 and 4.2 and multiplying this by the area of the cylinder this results in a theoretical buckling value 4329 MN. It is seen that the theoretical values matches the FEM values well. The buckling value of the solid elements is slightly more accurate. The maximum axial stresses in both both models are similar. Both computational times are very small, however if the model becomes more complex, these difference in computational time will start to matter and therefore the shell element is preferred.

4.3.2. MODELLING PILE-BOULDER CONTACT

In previous section it was shown that for an axial loaded cylinder the shell element is preferred over the solid element since the results are similar and the computational time is significantly reduced. In this section the elements are compared in more detail, focusing on the contact between monopile and a uniform sphere representing a boulder.

To model contact between two surfaces, ANSYS requires a Target and a Contact element. The Contact element moves in the direction of the Target. In the simulation performed, the monopile moves in direction of the boulder. In reality this is caused by the impact of the hammer. In ANSYS this means that the boulder is to be modelled as the Target and the monopile as the Contact. If large deformations of for example propagation damage is investigated, symmetric contact can be used by defining contact and target to both monopile and boulder. Modelling contact between the edge of the shell and the surface of the boulder requires a line-surface contact. ANSYS only allows the surface to be the contact and the edge (line contact) to be the target (thus moving the boulder into the monopile) which is a problem since in a later stage the hammer impact and consequently the movement of the pile into the boulder is to be investigated. One way to overcome this problem is by attaching a small ring of shell elements at the bottom of the cylinder, with two elements over the width equal to half the wall thickness and a height equal to the wall thickness. This way a line contact can be turned into a surface contact. Attaching this ring surface increases the length of the cylinder by a length equal to the thickness that leads to a small stiffness increase at the bottom of cylinder. This increase is suspected to be insignificant. A schematic of a section cut through the wall thickness is seen in Figure 4.8b and a ANSYS plot of the wall plus bottom area is seen in Figure 4.8a.

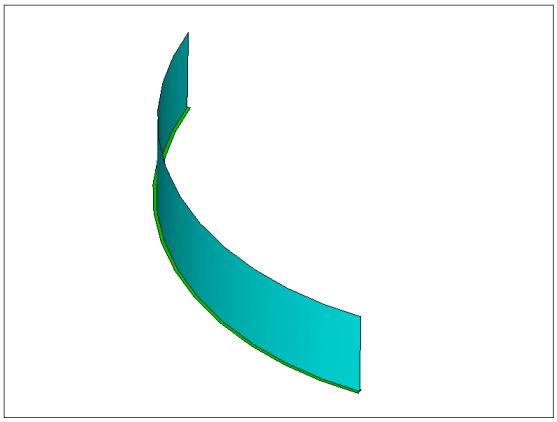

(a)

(b)

Figure 4.8: (a)Bottom monopile view on the shell element with attached area. (b) Schematic section cut of monopile wall thickness.

Again an axial compression simulation was performed, now by fixating the top and applying a compression force at the bottom op the monopile. A compression force of 1.0 MN (equal to a 0.59 MPa pressure) was

applied to the bottom of the regular shell model and the shell model with the attached area at the bottom (Figure 4.8b). This resulted in similar results for the displacements and buckling forces. This means that the attached area does not influence axial compression results.
More interesting is to model and investigate local contact between the cylinder and boulder. The contact area of boulder and cylinder was meshed in such a way that the number of nodes on both contact surface match, as seen in Figure 4.9b. Furthermore, the geometry of the elements in the contact area was modelled as squares since this is numerically desirable. This results into a fine mesh at the contact area, shown in Figure 4.9a.

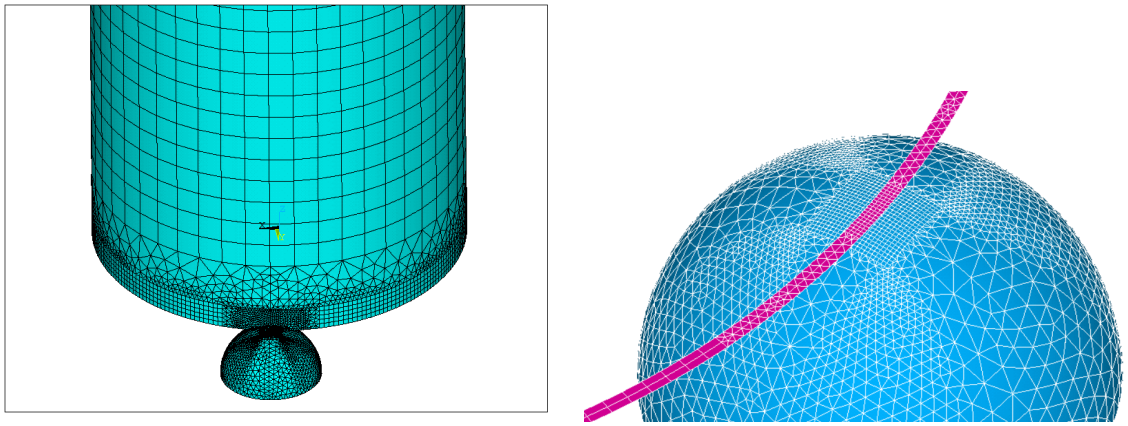

(a) (b)

Figure 4.9: (a) Monopile- and boulder mesh with four solid elements over the thickness, the mesh is small at the contact area. (b) Matching nodes and elements at the contact surface to help ANSYS stabilize the solution.

As was described before, the shell model has the disadvantage that the bottom area element consist of two elements over the thickness. Increasing this number will lead to rotation of these elements around their connected center point. It is suspected that two elements over the thickness will not be sufficient to accurately model the contact behaviour. A mesh refinement simulation was performed where the number of solid elements over the thickness was increased from 1 to 6 elements. For comparison reasons also a simulation with 8 elements over the thickness was performed. Typical strength parameters of granite shown in Table 4.3 were applied to the model and a friction coefficient of 0.5 was used.
Results of the contact pressure for one element and six elements over the thickness is seen in Figure 4.10. Plots of the contact pressure for the six thickness varieties are seen in the Appendix, Section E.1. By inspecting these plots it is clearly seen that applying more elements over the thickness is necessary to accurately model the contact behaviour. Plots of the linear buckling and maximum contact pressure for increasing the number of elements over the thickness are seen in Figure 4.11a and 4.11b respectively. By inspecting the plots it is seen that six elements over the thickness is sufficient to accurately model the contact behaviour. Logically, the mesh size has more impact on the local contact stress than on the buckling shape.

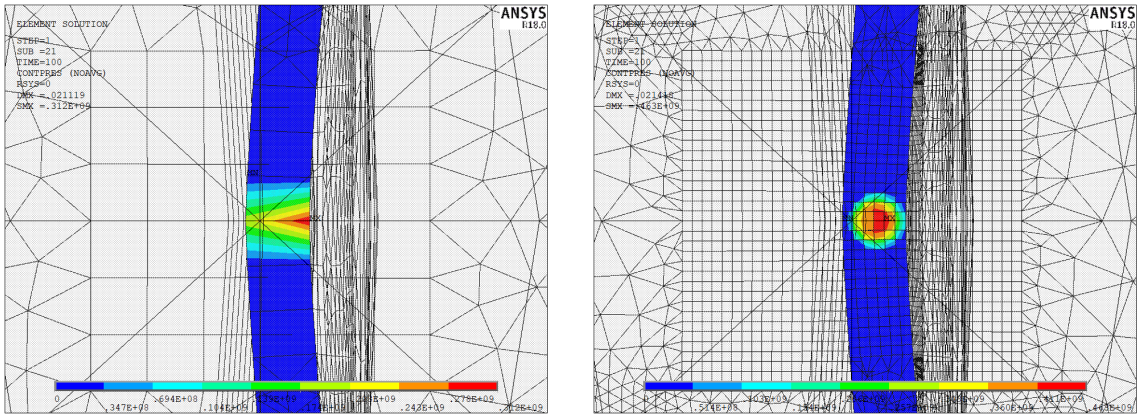

(a) (b)

Figure 4.10: (a) The contact pressure for the monopile having 1 solid element over thickness. (b) The contact pressure for the monopile having 6 solid element over thickness.

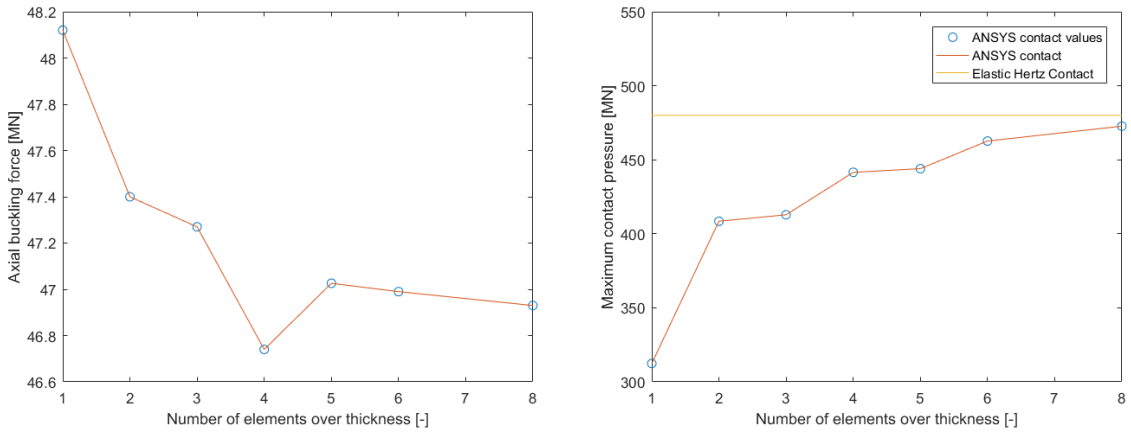

(a) (b)

Figure 4.11: (a) First linear buckling mode versus the number of elements over the wall thickness. (b) The contact pressure versus the number of elements over the thickness. The yellow line presents the elastic Hertz contact pressure.

The contact pressure was compared to theoretical formulations of Hertz contact between a elastic sphere and an elastic half-space (Negrea & Predoi, 2012). The expressions are formulated in Equation 4.3 through 4.6 and a sketch of the parameters is seen in Figure 4.12. The contact penetration output from ANSYS (seen in Table 4.7) was substituted in Equation 4.3. This leads to a Hertz contact area of around 34 mm, which is lower than the wall thickness. This indicates that the Hertz half-space contact theory is applicable. Substitution of the material properties of steel and rock (Table 4.2 and 4.3 respectively) and using a sphere with a radius of 1 m, leads to the theoretical maximum Hertz Contact stress shown in Table 4.7. Since the contact penetration from the model is quite constant, the maximum contact pressure is similar as well. The average of the theoretical Hertz contact stress from the runs is plotted in Figure 4.11b. Comparing this to the maximum contact pressure output from the model (Figure 4.11b and Table 4.7) it is seen that by increasing the number of elements over the thickness, the stress in the model tends to converge to the theoretical Hertz contact stress. From Figure 4.11 it is clearly seen that 2 elements over thickness is not sufficient and therefore it is necessary to disregard the shell model and continue with the solid element model. It should be noticed that the focus in the performed simulations was on the accuracy of the results and not on the computational time. This is because the computational time is still reasonable and therefore not relevant to inspect further.

$$a = \sqrt{R \cdot d_p} \tag{4.3}$$

$$F = \frac{4}{3} E^* R^{\frac{1}{2}} d^{\frac{3}{2}} \tag{4.4}$$

$$\frac{1}{E^*} = \frac{1-\nu_1^2}{E_1} + \frac{1-\nu_2^2}{E_2} \tag{4.5}$$

$$p_o = \frac{3F}{2\pi a^2} \tag{4.6}$$

Where:

- a is the contact radius [m]
- d_p is the penetration depth of the elastic half-space [m]
- $E_1, E2$ are the youngs moduli of each body [Pa]
- F is the applied force [N]
- ν_1, ν_2 are the Poisson's ratios of each body [-]
- p_0 is the maximum contact pressure [Pa]
- R is the outer radius of the sphere [m]

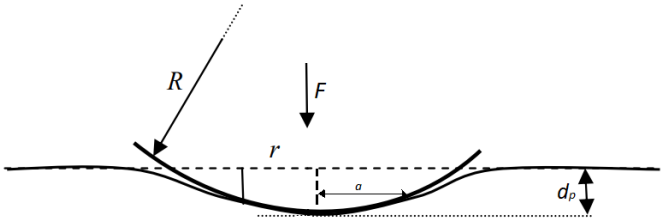

Figure 4.12: Schematic overview of the parameters used in the Hertz contact between an elastic sphere and half-space.

Table 4.7: Hertz contact results for an elastic sphere and elastic half-space

Number of elements over thickness [-]	FEM Contact penetration [mm]	Hertz Contact Stress [MPa]	Hertz Contact area [mm]	FEM Stress [MPa]
1	0.26	458	32.4	312
4	0.30	487	34.5	442
6	0.29	483	34.2	463

4.4. MODELLING THE SOIL BY NON-LINEAR WINKLER SPRINGS

An uniform medium-dense sand profile was chosen to be initially applied to this model. Soil characteristics for this sand profile are provided in the standard (API-RP-2-GEO, 2011) and are shown in Table 4.8. As mentioned in the theoretical background chapter (Section 2.8.1), the standards does not consider larger pile diameters. This correction was not performed in this study since the focus of this study is on the deformation of the steel. It is however recommended to include the correction in further studies.

Table 4.8: Uniform sand soil data

Soil Type	Relative density	Depth [m]	Submerged unit weight [kN/m^3]	Friction angle [°]	Initial subgrade modulus [MN/m^3]
Sand	Medium-dense	0-35	10	35	22

In the following paragraphs, modelling the lateral soil resistance is addressed first after which modelling the axial shaft resistance is discussed. End-bearing resistance of the soil is not included in the model since the boulder is located at the pile tip.

4.4.1. MODELLING THE LATERAL SOIL RESISTANCE

First, it is described how to transfer the 1D p-y curves to the 3D model. Secondly, applying the soil springs to an irregular mesh is discussed.

FROM 1D TO 3D

A convenient method to model the lateral pile-soil interaction is by representing the soil through non-linear Winker springs based on p-y curves as described previously. This means that the springs are discrete and do not possess continuity between one another, i.e. independent. A frequently used method to model the non-linear springs in a finite element model is described in this section. It should me mentioned that not only lateral pile-soil interaction, but also axial interaction can be modelled using a similar procedure.
What is generally done in pile-soil models is that non-linear springs are distributed around the pile to represent the soil. In circumferential direction discrete springs are applied as seen in Figure 4.13a. In vertical direction the springs are spaced with constant distances, as seen in Figure 4.13b. The springs are only capable of compression loading.

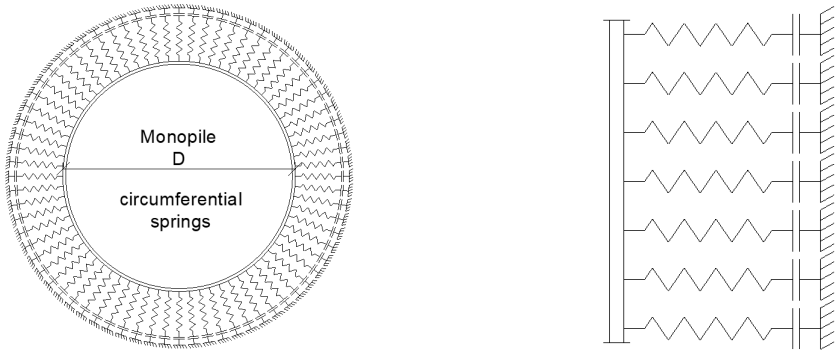

(a) (b)

Figure 4.13: (a) Schematic top view of the smeared circumferential springs. (b) Side view of the smeared springs over the pile length.

Due to the round shape of the pile, the springs further away from the outer right edge (Figure 4.14a) will carry less load in the direction parallel to the monopile displacement. Integration of this reaction will give the following relation between the multiple springs and the single PY obtained from the p-y curves. Assuming that the pile is infinite stiff, all spots on the pile will move over the same displacement δ_x. The reaction force in the springs is formulated in Equation 4.7. The elongation of the spring is shown in Figure 4.14b.

$$F = py \cdot \Delta l_{spring} \approx py \cdot \delta_x \cdot \cos\theta \tag{4.7}$$

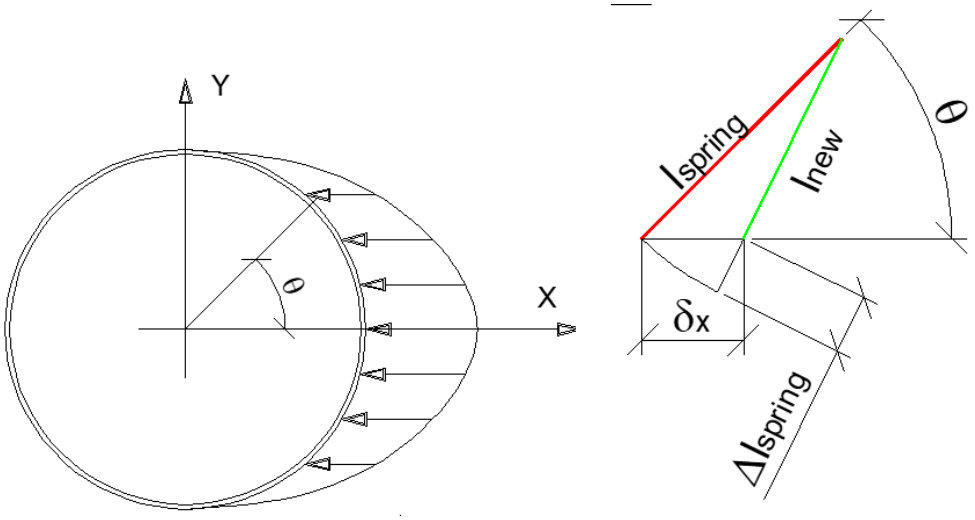

(a) (b)

Figure 4.14: (a) Displacement and spring forces.(b) Displacement δ_x and spring elongation.

The reaction force in x-direction per spring is formulated in Equation 4.8:

$$F_x = F \cdot \cos\theta = py \cdot \delta_x \cdot \cos^2\theta \tag{4.8}$$

For all discrete springs this results into Equation 4.9:

$$F_{tot} = PY \cdot \delta_x = \int_{\theta=-90}^{\theta=90} (py \cdot \delta_x \cdot \cos^2(\theta))d\theta \tag{4.9}$$

The obtained expression for a single py in the distributed situation is shown in Equation 4.10. In practice springs are often vertical distributed with gabs of 1 m. For simplicity this is assumed as well.

$$py = 2 \cdot \frac{PY}{\alpha \cdot n} \tag{4.10}$$

Where

- py = 3D spring value for distributed spring [N/m]
- PY = 1D spring value for 1 PY per unit length of the pile [N/m]
- α = vertical PY division per 1 m [-]
- n = number of springs on one side [-]

So far only half of the pile is considered, so for the full pile, the previous expression should be multiplied with a factor two as shown in Equation 4.11.

$$py = 4 \cdot \frac{PY}{\alpha \cdot n_{circumference}} \tag{4.11}$$

The described method of distributing the springs around the cylinder was verified with a simple ANSYS verification. For example let us consider a PY with stiffness of 30 N/m. This means that a force of 10 N results into a displacement of 0.333 m. In ANSYS a plate was modelled with 60 distributed springs around the edge of one side of the plate. This means 120 distributed springs along the edge of the whole plate. According to the above described spring distribution, a single spring should be modelled with a stiffness of:

$$k = 4 \cdot \frac{30}{120} = 1 \text{ N/m}$$

This spring stiffness of 1 N/m was applied to all springs and the initial force of 10 N was applied at the centre of the plate in x-direction. The solution of the displacement of the plate in ANSYS is shown in Figure 4.15. It is seen that the plate moved on x-direction as supposed to. The white circle to the left represents the original position of the plate. It is seen that the displacement of the circle is again 0.333 m (top-left corner).

This matches the displacement calculation of the single PY and therefore the spring distribution method is verified.

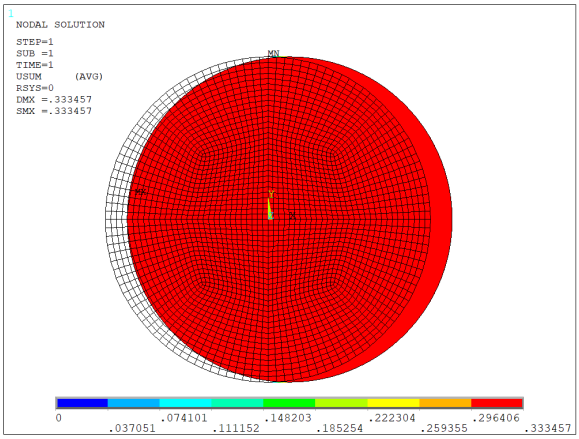

Figure 4.15: Displacement of a plate in x-direction. 60 distributed springs along plate edge.

SOIL SPRINGS INDEPENDENT OF MESH SIZE

The previous described transition of the 1D PY-spring to the distributed py-springs along the circumferential of the plate was transferred to a 3D cylinder. It is also important to consider that at a later stage the soil springs should be applied on a variety of meshes and orientations. These differences are caused by geometrical variations in the cylinder or by manually modifying the meshes as desired. It is therefore useful to write a script that will apply the soil springs to the model independent of the mesh size and orientation.
First, verification of the PY-spring distribution to the 3D cylinder was performed. An uniform 1D PY spring of 10 N/m per vertical unit length was chosen to be applied to a 4 m cylinder together with a 1D lateral force of 10 N. This means that pure lateral displacement of the cylinder is equal to $10/(4 \cdot 10) = 0.250$ m. The distributed springs were applied to the corner nodes of the rectangular mesh showing in Figure 4.16a according to the formula described in Equation 4.11. Applying an quadratic mesh with elements of 0.5 m length resulted in 16 corner nodes along the cylinder circumferential. A PY distribution of 0.5 m in vertical direction was considered, thus 2 divisions per meter. According to Equation 4.11, this results in a distributed 3D py value of:

$$py = 4 \cdot \frac{10}{2 \cdot 16} = 1.25 \text{ N/m}$$

A 10 N force is applied at the top of the cylinder in y-direction. This force might however be applied at any node since the cylinder is modelled as a rigid body. The cylinder was modelled as a rigid body by applying a high Young's modulus and thickness to the model. A Young's modulus in the order of E15 and a the thickness of the elements of 0.5 m was selected, since using higher order E modules introduced numerical errors. Modelling a rigid body this way is simple, however might introduce a very small error since the cylinder in not completely rigid. The stiffness of the springs at the top and bottom was divided by 2 since they only contribute to half of the area. A script was then written that loops from the top to the bottom z-coordinate of the cylinder and attaches the springs to the outside nodes of the cylinder. The result of the analyses is shown in Figure 4.16b. A displacement of 0.126 is obtained. This displacement is well seen in a top view plot, Figure 4.17. Multiplying this by a factor 2 results in a displacement of 0.252 m, which more or less matches the theoretical displacement value of 0.250 m. This value was determined to be appropriate since assuming a high Young's modulus and thickness introduces a small error. Also the mesh size is influences the results slightly. The factor 2 is due to the fact that in this case symmetric linear springs are used. This means that the springs have a tension and compression part which means that when the cylinder will move in one direction, have the springs will experience compression and half experience tension which results in a stiffness that is doubled. This is non-physical: soil does not have this tension part and the springs in the model should be modified by getting rid of the tension part, thus applying zero stiffness in the tension part of the spring curve. This can for example be done in ANSYS by using a gab element or using a non-linear spring with close to zero stiffness in the tension part as shown in the Appendix, Figure C.2b. This modification was tested and proved to work.

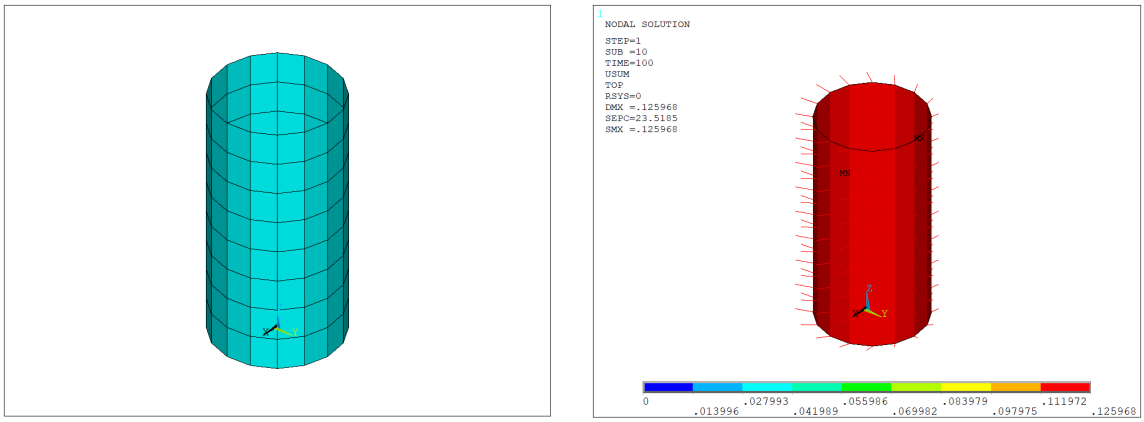

(a) (b)

Figure 4.16: (a) Rigid cylinder with with a mapped quadratic mesh. (b) Displacement sum after distributing a spring stiffness PY of 10 N/m per unit length over a 4 m long cylinder and applying a force of 10 N in y-direction.

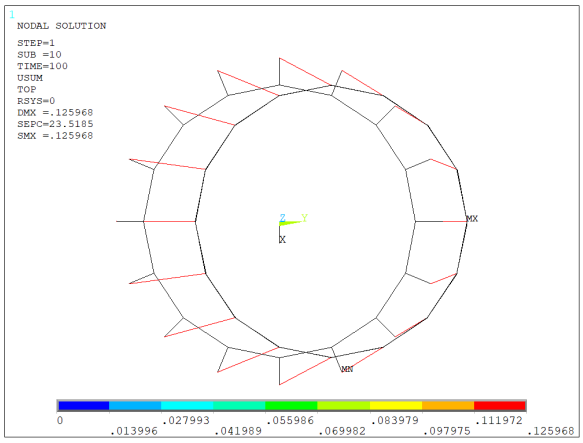

Figure 4.17: Top view of the quadratic, mapped-meshed cylinder. Displacement of the cylinder in y-direction.

Second, a script was written that applies the 3D distributed py's to a mesh size and orientation of choice, whereas the previous script only worked for a rectangular mesh. An arbitrary free mesh with triangular and quadratic elements is seen in Figure 4.18a and is used as test object. A script was written that calculates a reference py for a specific small area and scales this py to the area associated with a specific node.
The method used to apply the springs to the corner nodes of the elements is described briefly:

1. Loop through all nodes. For every single node, calculate the area of the elements surrounding the node and output the z-coordinate
2. If an area is rectangular, multiply the area by 1/4, if triangular by 1/3, and sum the resulting area's. Let's call this area A_{node}
3. Use the z-coordinate of the node and calculate the 1D PY according to the standard (API-RP-2-GEO, 2011)
4. Calculate reference area for a small rectangular reference element. This was done for 1 degree in circumferential direction and 0.5 m in height. The area associated with this small element is then $\frac{\pi \cdot D}{360} \cdot 0.5$. Let's call this area A_{ref}. The 3D py_{ref} is then calculated similar as in Equation 4.11 with α equal to 2 and $n_{circumference}$ equal to 360
5. The 3D py per node is than equal to $A_{node}/A_{ref} \cdot py_{ref}$

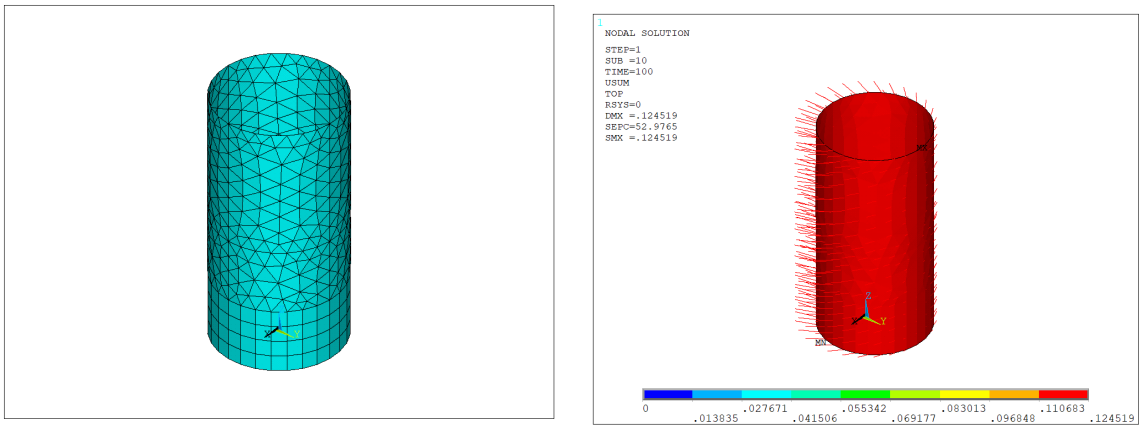

(a) Combined quadratic and triangular free mesh

(b) Plot of the displacement sum

Figure 4.18: (a) Rigid cylinder with with a free triangular and quadratic mesh. (b) Displacement sum plot after distributing a spring stiffness PY 10 N/m per unit length over a 4 m long cylinder and applying a force of 10 N in y-direction.

This method was verified by applying the same load and boundary conditions to the cylinder shown in Figure 4.16a. This resulted in a displacement of 0.0153, shown in Figure 4.18b. This matches the previous displacement of 0.0155 quite well. A small deviation in the fourth decimal can be explained by the fact that the cylinder is not 100 percent rigid and wen changing the mesh size this well have a small influence on the result. Furthermore, individual springs were checked at a specific location and these springs proved to have similar stiffness.
Another verification of this method to distribute the springs is that the total sum of all the area's calculated should equal the total area of the cylinder. This check for a cylinder with similar geometry resulted into:

$$\text{Total area} = \pi \cdot D \cdot L = 3.14 \cdot 2 \cdot 4 = 25.133 \tag{4.12}$$

The total area calculated by ANSYS equals 25.133 for the rectangular mesh shown in Figure 4.16a and 25.132 for the triangular mesh size shown in Figure 4.18a. This small deviation for the triangular mesh is the result of the fact that the area of the triangles connected to a single node is not exact equal to the sum of 1/3 multiplied by the triangular area's. This error is however to be shown very small already in this quite big mesh size and should reduce even further if the mesh size is refined. To conclude, with these two simple checks the distribution of the 1D PY spring over the 3D cylindrical area is verified.

LATERAL SOIL RESISTANCE INSIDE THE PILE

Due to collision with an obstacle the pile wall might deflect inwards, compressing the soil inside the pile, resulting in a lateral reaction force from the soil. The stiffness of the soil inside the pile might influence the local deformation of the steel. The soil inside the pile might behave different than outside the pile since it is trapped. For large deformations the presence of the other side of the monopile's wall might effect the response of soil inside the pile (stiffening). It is assumed that the soil inside the pile cannot fail and only experience compression (since it's trapped) and that the soil's elastic modulus increases linearly with depth. The latter is in agreement with many test results (Verruit & van Baars, n.d.), even though is it is acknowledged that soil is not a linear elastic material. According to Verruit & van Baars, the elastic modulus in sand is often expressed as in Equation 4.13.

$$E_{eod} \approx 250 \cdot q \tag{4.13}$$

Where q is the effective over burden stress equal to the unit weight of the soil times the depth, as was described in Chapter 3. Considering a uniform medium - dense sand profile with a undrained unit weight of 10 kN/m^3 at a depth of 20 m, the elastic modulus for static loading equals $250 \cdot 10,000 \cdot 20 = 50.0$ MPa. Verruit & van Baars furthermore mention that for wave propagation problems the soil will be about a factor 10 stiffer, thus 500 MPa. For more accurate stiffness values one should perform field measurement or laboratory tests.
Since the soil can only be compressed, the soil inside the pile can be modelled by either compression springs or by solid elements with contact elements between the soil and pile wall that prevent the soil behaving in tension. Since it was seen that by including contact and solid elements the solving time of the model increases

significantly, springs were chosen to represent the lateral soil support inside the pile. Ideally, the tension part of the p-y springs of the outside soil is used since these springs are already included in the model. The force-displacement curve of a single spring is seen in Figure 4.19. The already modelled p-y springs are connected to the outside of the monopile; this creates a small discrepancy regarding the soil inside the pile. This discrepancy is assumed to be insignificant since the elastic modulus is already theoretically approximated and the elastic modulus dominates the soil stiffness.

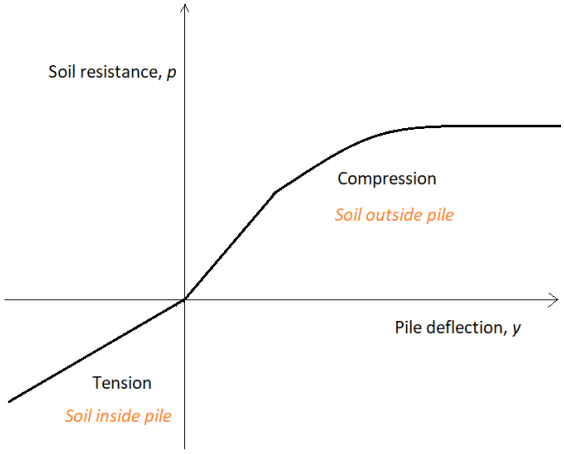

Figure 4.19: Modelling the inside soil linear lateral resistance by using the tension part of the p-y springs

In order to determine the spring stiffness, first a simple model was created by modelling the lower part of the monopile including solid soil support on the inside of the pile. The bottom 5.0 m of the pile was modelled with the same geometrical properties as shown in Table 4.1. Contact elements were used between the wall and soil so that the soil can only experience compression. This can be seen in the appendix, Figure E.11. The top of the wall and soil was clamped. The bottom ring of the soil was also constrained in vertical direction. A compression pressure was applied on a small area at the bottom of the pile representing the lateral load component acting on the pile that is caused by pile-boulder collision. The pressure is shown by a red arrow in Figure 4.20a. The part shown in purple is thus the soil that is modelled deeper than the bottom of the pile wall (blue). The soil is there in reality and its presence makes the soil behave slightly stiffer. Half symmetry is used to speed up the calculation time. The maximum elastic modulus at the maximum pile penetration depth of 35.0 m was applied to the soil (87.5 MPa using Equation 4.13). This results in a maximum radial displacement of 15.9 mm as seen in Figure 4.20b. It is seen that at the applied pressure location the wall and soil deflect inwards (blue) and that due to the pressure the wall at some distance away from the pressure deflects outwards (red). Since there are contact elements between the wall and soil the soil experiences compression only.

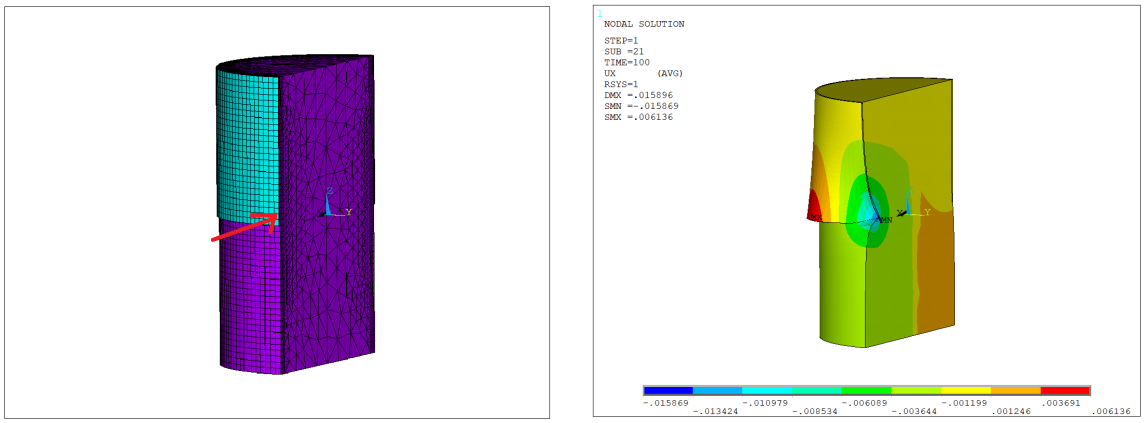

(a) (b)

Figure 4.20: (a) Plot of the wall (blue) and soil (purple) mesh and the location of the applied pressure depicted by the red arrow. (b) Resulting radial deflection, in blue the inward deflection and in red the outward deflection of the wall. Not to scale.

The clamped boundary condition at the top of the pile and soil however, influences the results. The fixed boundary at the top leads to the pile behaving as cantilever. To get rid of the undesired influence of the boundary condition, the length of the pile and corresponding inner soil was increased. The radial displacement versus the length is seen for simulations of the pile wall only (red) and pile with inner soil (blue) in Figure 4.21a. The difference between these lines is the effect of solely the soil on the radial displacement and it is seen that the displacement converges nicely with increasing length of the pile (Figure 4.21b). The displacement at 35.0 m is converged well and selected as the length that should be used to not 'feel' the influence of the boundary condition at the top. Looking back at Figure 4.21a, at 35.0 m the displacement of the simulation with pile wall and inner soil (red line) equals 33.3 mm. To be sure that linear springs can be used to model the soil inside the monopile, the force versus the radial-displacement at several nodes was checked in the solid elements soil model. A plot of the force versus the radial-displacement at a node in the area where the pressure was applied is seen in Figure 4.21a. The force-displacement curve seems linear and therefore the solids can be replaced by linear springs.

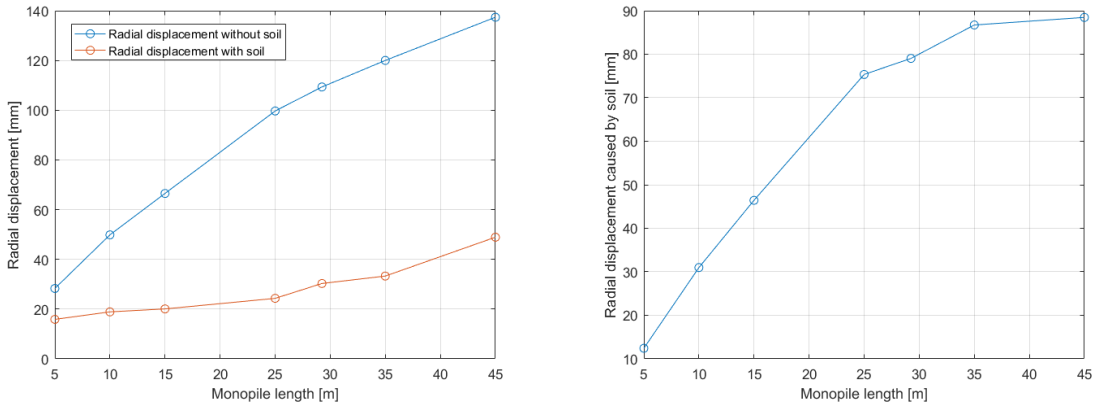

(a) (b)

Figure 4.21: a) Radial-displacement versus the length of the pile's wall including (red) and excluding soil (blue). (b) Radial-displacement versus the length of the monopile of the effect of the soil.

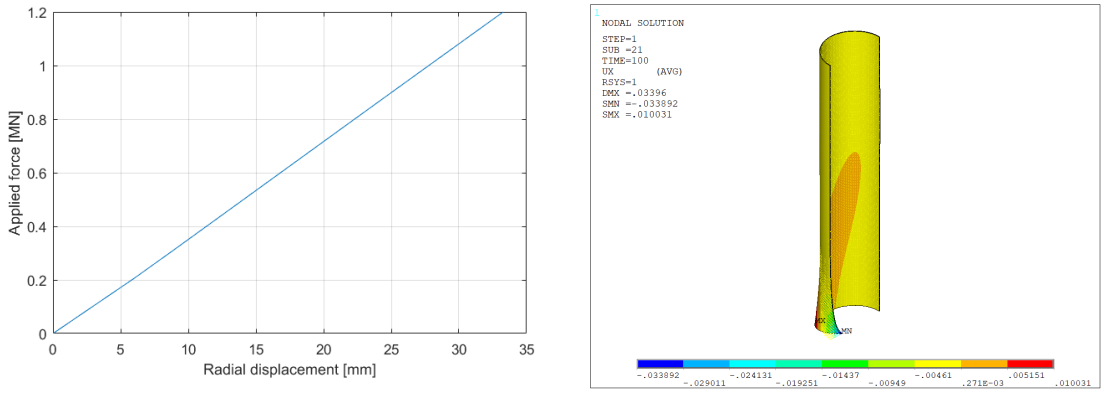

(a) (b)

Figure 4.22: (a) Force versus radial-displacement for a node in the applied pressure area (red arrow Figure 4.20a) in the solid soil elements model. (b) Radial displacement plot of a 35 m monopile model including soil inside the pile modelled by linear Winkler springs.

The next step is to model the 35.0 m pile wall with linear Winkler springs to represent the soil inside the pile and to match the displacement of 33.3 mm. In this simulation it is important to define the spring force-deflection curve such that it can only operate in compression. By running several simulations with different spring stiffness constants, a stiffness of $4.3{\cdot}10^5$ N/m^3 was found that matches the previous obtained displacement of 33.3 mm. Using a similar approach as was described in the previous section, the spring stiffness is smeared out over the irregular mesh. The results of the volume element soil model inside the pile is compared with a model where the outside p-y curves were applied on the inside as well. These results match quite well, as is seen in Section 5.6.2.

LATERAL EARTH PRESSURE

It is assumed that the lateral earth pressure acts on the inside and outside of the pile wall. This means that the net pressure acting on the pile wall equals zero and therefore the lateral earth pressure does not influence the buckling behaviour and is not taken into design consideration.

4.4.2. MODELLING THE AXIAL SOIL RESISTANCE

A similar modelling approach as applying the lateral resistance with p-y curves was done for the axial shaft resistance. T-z curves describe the vertical displacement z of the pile for any mobilized shear force or skin resistance T. The shaft friction per unit length pile was determined according to the API-R2-GEO (Appendix, Section C.2). For every node the shaft friction was multiplied by the area of the node A_{node}. As mentioned, the monopile is assumed unplugged. This indicates that the soil can move vertically inside the pile wall creating shaft resistance. It was assumed that the shaft friction outside the monopile equals the shaft friction inside the monopile. Therefore the external shaft friction was multiplied by a factor two to include the contribution of soil inside the pile to the axial shaft resistance.

4.4.3. VERIFICATION OF THE GENERATED SOIL DATA

As described previously, the soil curves were generated according to the American Petroleum Institute standard (API-RP-2-GEO, 2011). To make sure that no errors were made while generating this data, the generated data was tabled for specific values and verified with the software OPILE (Cathie Associates SA/NV, 2015). This software follows the same generation of the soil curves according to the API-RP-2-GEO, based on the soil input characteristics. A downside of OPILE is that the discretization of the curves over the depth of the monopile is limited to 0.25 m. Since this model will use smaller discretization steps (small element size), it is more accurate to generate the data in the model in ANSYS. This is also more convenient since this way the soil data is automatically updated when changing pile or soil characteristics in the model. The output of OPILE matched the results of the data generated for p-y, q-z, and t-z curves in the model and is therefore verified.

4.5. DEFINITION OF THE CONTACT ANGLE

In reality, the boulder will always hit the pile asymmetrically. Different locations of the boulder are to be investigated as is done in Section 5.8. To be clear about the different positions of the boulder under the pile wall and to distinguish between these positions, the pile-boulder contact angle $\alpha_{contact}$ was defined. A schematic 2D section-cut of the pile's wall and varying contact angle is seen in Figure 4.23. The angle is defined as the angle between the horizontal bottom of the pile and the tangent of the edge of the monopile on the boulder. This angle is chosen negative (Figure 4.23a) when the boulder's centre is located inside the monopile and positive (Figure 4.23b) outside the monopile. To clarify, the boulder position in- and outside the monopile's wall is seen in 3D in Figure 4.24a and 4.24b respectively.

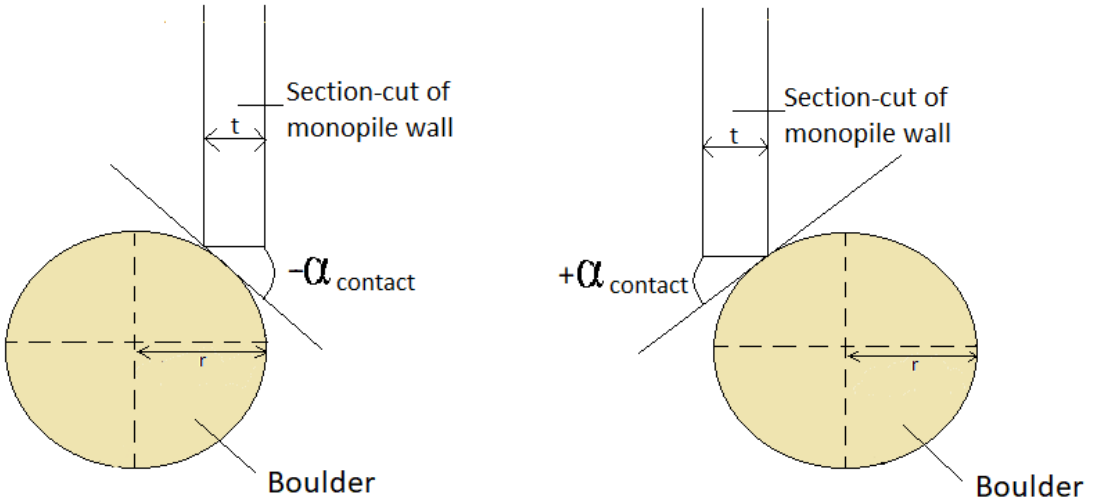

(a) (b)

Figure 4.23: (a) Boulder's centre located inside the pile. (b) Boulder's centre located outside the pile. (a) and (b) show different locations of the boulder under one side of the pile, forcing asymmetric loading on the pile.

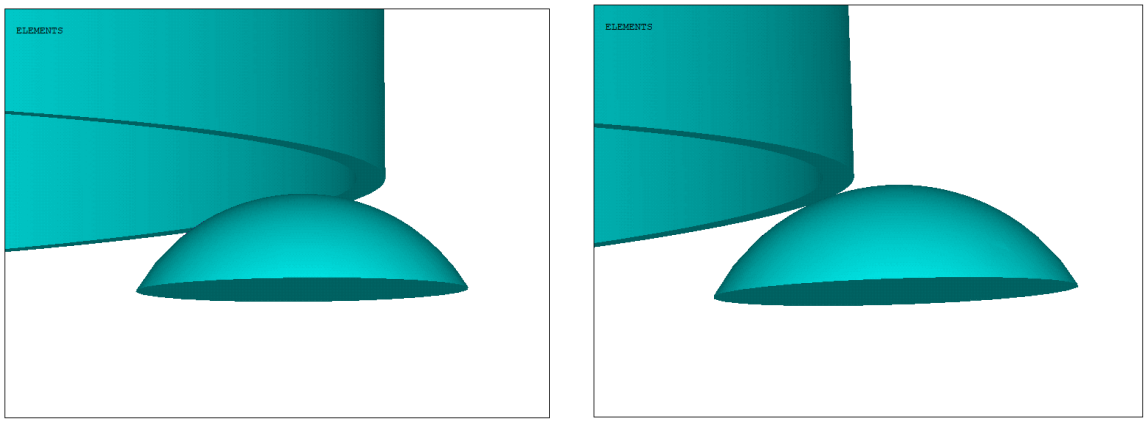

(a) (b)

Figure 4.24: (a) Boulder's centre located inside the pile. (b) Boulder's centre located outside the pile.

5

NUMERICAL MODEL - STATIC

5.1. INTRODUCTION

In the previous chapter 'introduction to the model' the basics behind the model were discussed. Contact was modelled between a monopile and a fixed boulder. For the monopile geometry specifics mentioned in Table 4.1, it was determined that six solid elements over the thickness should be used to accurately model the interaction between a monopile and boulder of unit radius. Granite with a Young's modulus of 50 GPa was selected to represent the boulder. Furthermore, scripts were written to apply lateral and axial soil resistance to the model and the contact angle between the boulder and monopile was defined. In this chapter this model is investigated in more detail. If not mentioned otherwise, similar geometrical and material parameters as described in the previous chapter were used. Nonlinear static simulations were performed. In all cases an uniform axial compression force was applied at the top of the monopile. The model aspects and parameters that were investigated are listed below.

- Geometric- and material nonlinearities
- Pile imperfections
- D/t ratio
- Size of the contact area
- Axial and lateral soil support
- Friction coefficient
- Position of the boulder
- Boulder embedded in soil

5.2. GEOMETRIC- AND MATERIAL NONLINEARITIES

In numerical FEM simulations, one typically distinguishes geometric linear (also known as small-displacements) and geometric non-linear (also known as large-displacements) simulations. Geometric linear simply means that the stiffness does not differ due to changes in the shape during simulation. This will reduce the simulation time but in many cases leads to wrong results as will be shown in this section. A 25 MN axial static (hammer) force was applied at the top of the cylinder. In these simulations the 2.0 m diameter boulder is located symmetrically straight under the pile wall and a high steel-rock friction coefficient of 0.5 was selected to prevent the pile from sliding over the boulder's surface. Detailed investigating of the friction coefficient was done at a later stage, shown in Section 5.7. The length of the modeled pile section was the lower 15.0 m. The part of the pile above the 15.0 m was not modelled to save computation time. In Section 4.2.1 it was concluded that a length equal or larger than 10.0 m can be used to continue investigating the model since the top of the pile does not influence the local deformation. Furthermore, soil support was not included in this simulation and hence the only boundary is the fixed rotation at the top. This was done to save calculation time since the purpose of these simulations is showing the influence of non-linearities on modelling. A plot of the force versus the radial displacement at a node in the centre of the wall, 0.1 m above the contact area (node 1, Figure 4.1b), is seen in Figure 5.1a for a geometric linear simulation. In this figure it is seen that there is a inclination in the curve which is caused by the nonlinear contact behaviour of the pile-boulder collision. It was seen that after initial contact, the wall at the contact point deflects inwards. This leads to the boulder-pile

contact moving normal to the wall in opposite direction, thus towards the outside of the monopile wall. The deflection of the contact is clearly shown by plotting the axial stress component in the monopile (Appendix, Figure E.4 and E.5). When a geometric nonlinear analyses (enabling large-deformations (NLGEOM,ON in ANSYS)) is performed, changes in the stiffness during to geometric deformations are allowed. This is realistic and requires more computational time. The force-displacement results of the large displacement simulation is seen in Figure 5.1b. It is seen that the radial displacement increases significantly for lower loads when large deformations are enabled. This indicates that the results are largely under-predicted by considering small displacements. Since the difference in geometric linear and geometric nonlinear analysis is large, geometric nonlinear simulations should always be performed in this kind of simulation. Also the displacements in the other two directions were checked. Here the difference in the displacement results were less significant. Therefore the radial displacement is a good factor to check in these analyses.

By inspecting Figure 5.1b it was noticed that due to geometric nonlinear effects, the force needed to initiate displacement reaches an asymptote, resulting in an unstable solution (convergence problems) in ANSYS. ANSYS usually collapses at this point due to too much deformation of the elements in the contact area or due to its inability to find a stable static solution which might happen when the pile slides off the boulder or the boulder is pushed away. This point is taken as the maximum static force you are able to apply to the structure and is a good indicator for the pile's capacity. The structure cannot absorb more force than this limit and becomes unstable. To be consistent, this limit is called '*static load limit*'. In this plot it can be seen that the static load limit is reached at 19.7 MN.

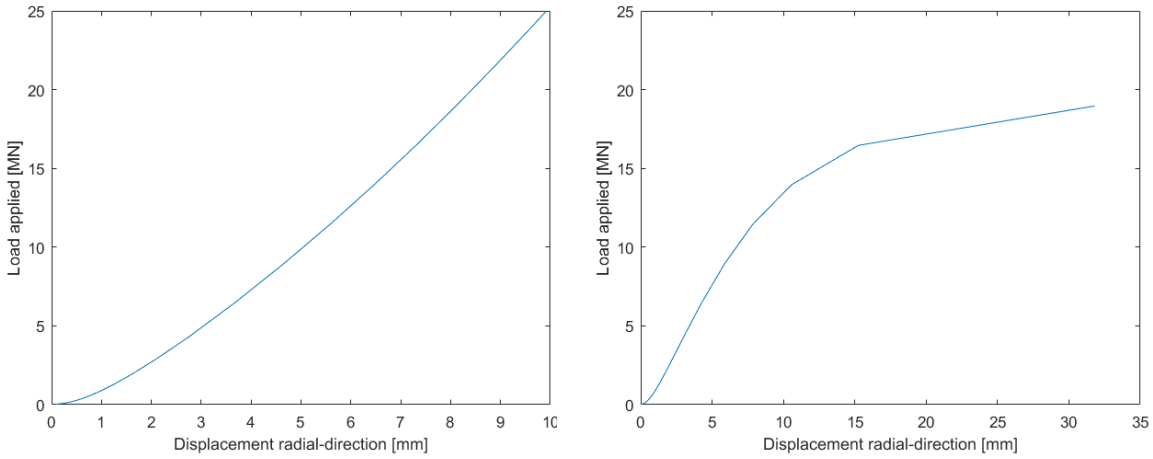

(a) (b)

Figure 5.1: (a) Applied axial load versus displacement curve for linear geometry properties. (b) Applied axial load versus radial-displacement for nonlinear geometry. In (a) and (b) the displacement was plotted for the contact node 0.1 m above the contact area in the centre of the wall.

When nonlinear properties of steel (Figure 4.2) are used in the model for a linear geometric simulation, the solution did not converge after an applied load of 7.9 MN (Figure 5.2a). At the final load-step, plastic-strains at the contact area higher than 15 % were obtained. These very local plastic strains at the pile-boulder interaction do not matter in terms of the global stability of the pile and as was mentioned before, when ANSYS stops converging is seen as a better criterion than the local plastic deformation. Performing the same simulation for a geometric non-linear simulation further reduces the static load limit to 6.0 MN, as shown in Figure 5.2b. A check was performed to check if the non-linear material properties were correctly applied to the model. A figure of the Von-Mises stress at an applied load of 25.5 MN for a run with a 10.0 m model, friction coefficient of 0.3 and $\alpha_{contact}$ = 20 degrees and a plot of the total strain at 25.5 MN are included in the Appendix, Figure E.13b and E.13a respectively. It was seen that the yield stress of 316.7 MPa was exceeded and that the ultimate stress at fracture of 450 MPa (DNV-RP-C208, 2016) was reached. Also the ultimate strain of 15 % (DNV-RP-C208, 2016) was reached. Since the slope of the strain-stress curve used in the model increases almost horizontal in the model, it is seen in the figures that the stress remains constant at 450 MPa and the strain keeps increasing (68.1 %). The stress-strain curve was kept horizontal after the fracture point since fracture modelling in ANSYS was out of the scope of the research. It should however be noticed, that

in reality the steel is likely to fracture locally since the maximum strain is exceeded and this is likely to lower the capacity of the steel. Since stress-strain results match the material model input, it was concluded that the non-linear material model was included correctly into the model.

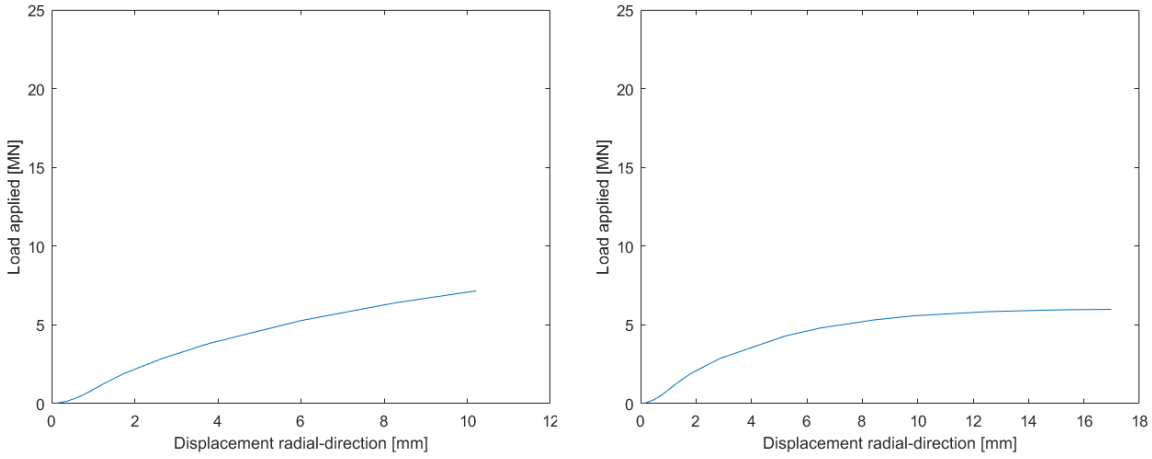

(a) (b)

Figure 5.2: (a) Axial load versus radial displacement curve for linear geometry properties and non-linear material properties. (b) Axial load versus radial displacement for nonlinear geometry- and nonlinear material properties. In (a) and (b) the displacement was plotted for the contact node 0.1 m above the contact area in the centre of the wall.

The results of the four performed simulations are plotted in Figure 5.3. Here SD stands for 'small displacements' (geometric linear) and LD stands for 'large displacement' (geometric nonlinear). In this figure it is seen that the simulation with both geometric- and material nonlinearities results in the lowest static load limit that is to be applied to the monopile. This simulation is the most realistic one and further simulations are to be performed with these properties. Also, it is noticed that material non-linearity has significantly more impact on the static load limit than the geometric non-linearity. Furthermore, it can be seen that slightly above the contact pressure exceeds the yield strength of the material, thus local plasticity occurs (blue horizontal line), the curves start to diverges in respect to each other. This means that when one is interested in the behaviour of the steel in the elastic region, geometric- and material linear properties are sufficient to simulate.

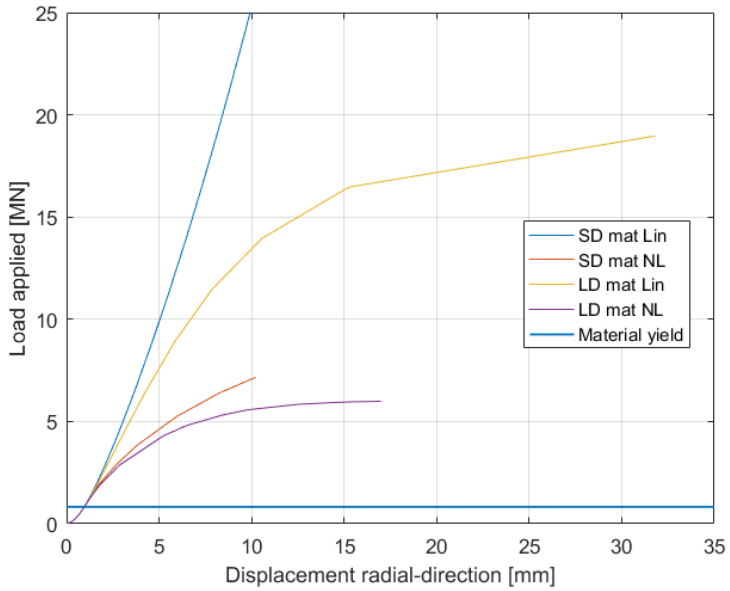

Figure 5.3: Plot of the applied load versus the radial-displacement for four simulations. 1, geometric- and material linear (blue line). 2, geometric non-linear and material linear (yellow line). 3, geometric linear and material non-linear. 4, geometric- and material nonlinear. The horizontal blue line represents the applied load at which the contact pressure exceeds the yield strength of the material.

5.3. PILE IMPERFECTIONS

So far the pile that was considered was geometrically perfectly round. In reality however, the pile consist of imperfections included in the fabrication process. The limitations of these imperfection tolerances are described in standards. Following the DNV (DNVGL-OS-C401, 2015), the maximum allowable deviation from the nominal radius and local out of straightness were checked. These tolerances are included in the Appendix, Figure D.1. For the considered pile with a radius of 3.7 m, the out of straightness of 22.6 mm turned out to be the maximum allowable fabrication tolerance. As in the previous section, the steel-rock friction coefficient used was 0.5, the boulder diameter 2.0 m, the length of the pile 15.0 m and no soil was included. A linear buckling simulation was performed and the first linear buckling mode is seen in Figure 5.4a. The five first buckling modes are included in the Appendix, Section E.3. This first buckling mode was scaled to meet the out of straightness tolerance of 22.6 mm and this new geometry including the imperfection was used for another geometric- and material non-linear buckling analyses. The result of the analyses with a perfect pile and the analyses including the pile imperfection is seen in Figure 5.4b. It was noticed that due to the imperfection, the static load limit decreases from 6.00 MN to 5.42 MN, which is an decrease of 9.5 %. Furthermore, the imperfection seems to result in an initial increased stiffness. This apparent increased stiffness is caused by the difference in the pile shape due to the imperfection and this results in the contact elements interacting slightly different. This imperfection is not included in other static sensitivity analyses in this chapter since the computational time to perform the simulation increased a lot (since first a linear buckling analyses after which a non-linear static analyses is to be performed). To account for the geometric imperfection in the pile, a safety margin of 10% is suggested.

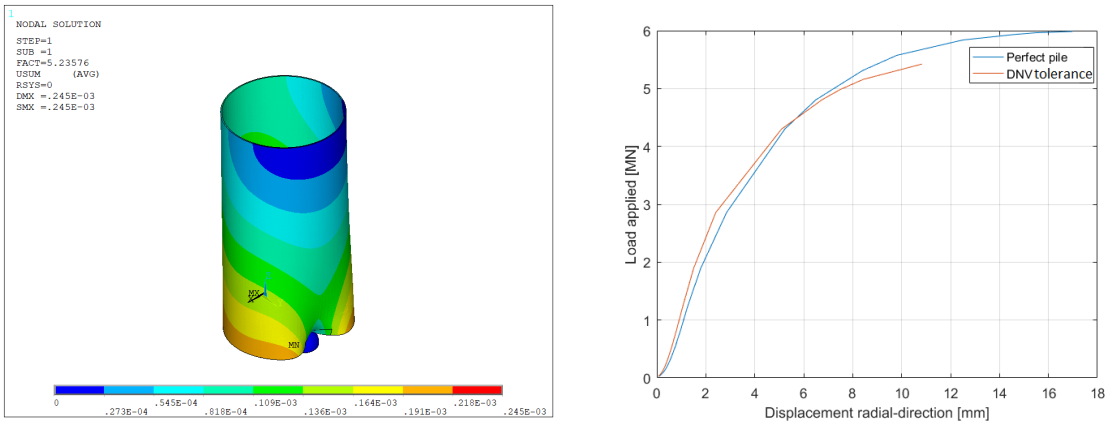

(a) (b)

Figure 5.4: (a) Plot of the first buckling mode in ANSYS. This deformation mode is scaled to meet the tolerance provided in the standard (DNVGL-OS-C401 2015. (b) Applied load versus the radial-displacement for a perfect round pile (blue line) and a pile with initial imperfection (red line).

5.4. THE D/T RATIO

The D/t ratio is the ratio of the diameter over the wall thickness of the monopile. The current increase in turbine size required larger foundations. This trend is visible in the offshore industry by the continue increasing diameters of the monopile. The thickness of the wall is generally however is not increased proportional, resulting in more slender piles. D/t ratios equal to 100 have already been exceeded. These piles are likely to be more vulnerable to tip damage caused by collision with obstacles.

The effect of D/t ratios on damage to the pile tip was investigated first by keeping the diameter of the pile constant and varying the thickness of the pile (t inc.). As in the previous section, the steel-rock friction coefficient used was 0.5, the boulder diameter 2.0 m, the length of the pile 15.0 m, no soil was included and the boulder was located symmetrically under the pile wall. A plot of the force versus the radial displacement at Node 1 for different D/t ratios is seen in Figure 5.5a. The static load limit is shown in Table 5.1. In Figure 5.5a it is clearly seen that by increasing the D/t ratio (hence decreasing the thickness), the static load limit decreases rapidly. The same three D/t ratios were then plotted for simulations where the thickness was kept constant and the diameter varied (D inc.). Here D/t equal to 100 was chosen as base case from where the diameter and thickness were varied since this is a common used ratio in the offshore industry. In Figure 5.5b the D/t ratios with a constant thickness are represented by the dashed lines and the base case with a D/t equal to 100 by the triangular line. It is obtained that keeping the thickness constant and increasing the pile diameter also leads to lower static load limits. The rate of change in static load limit is larger when the thickness is varied (solid lines) than for varying the diameter (dashed lines). This indicates that the thickness is the driving geometrical parameter considering buckling of the pile due to collision with a spherical boulder. This matches existing research on pile tip deformation by Aldridge et al. (Aldridge et al, 2005) and MSL Englineering Limited (MSL Engineering Limited, 2001). In these studies it is described that for large D/t ratio's the damage to the pile tip is a function of the wall thickness only. Where historically the non-dimensional D/t ratio was used as a single independent design criteria, it is clear that these two parameters cannot be seen independent of each other and in the design, one should check for both the influence of the diameter and the influence of the thickness.

Table 5.1: Impact of D/t ratio on the monopile deformation by keeping the diameter constant and varying the thickness

D/t ratio [-]	**Maximum axial force [MN]**
60	18.3
100	6.00
140	2.96

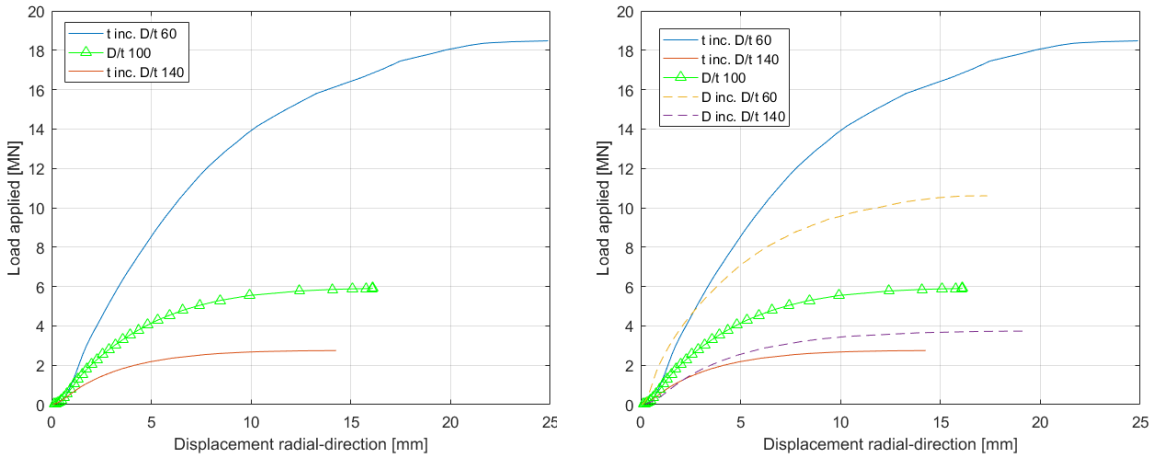

(a) (b)

Figure 5.5: (a) Applied load versus radial-displacement for different D/t ratios keeping the diameter constant and varying the thickness. (b) Applied load versus radial-displacement for varying D/t ratios. The filled lines represent the D/t ratios keeping the diameter constant and the dashed lines show the D/t ratios keeping the thickness constant. The triangular line represent the base case where D/t equals 100.

5.5. THE SIZE OF THE CONTACT AREA

To investigate the effect of the contact area, which depends on the size and shape of the boulder, on damage to the pile tip, three different spherical boulder sizes were modelled that lead to different contact areas: diameters of 2.0 m, 1.0 m, and 0.5 m. The 2.0 m size limit was chosen since this is typically the range of the maximum boulder sizes seen offshore (Section 2.5). A sketch of the different sizes is seen in Figure 5.6 (not to scale). In these situations the boulder is located symmetrically under the pile wall, the friction coefficient equals 0.5, the length of the pile is 15.0 m and there is no soil included in the model. The results of the force versus axial-displacement at node 2 is shown in Figure 5.7. First, it is seen that the maximum load able to be applied to the model is close. This is logical since the failure mechanism of the pile is similar in these cases. This is caused by the fact that only the amount of contact area increases and the other parameters remain constant. The amount of contact area does however lead to stiffer responses for larger boulders in the force-deflection curves. This makes sense since the contact area is larger and hence the force is better spread over the boulder and the pile. Small boulders are however relatively easy to push away into the soil or to break as is discussed in more detail in Section 6.2. An approach to model the displacement of a boulder into the soil is elaborated in more detail in Section 5.9. As this study focuses on failure of the pile tip and not the boulder, a 2.0 m boulder is used in further analyses.

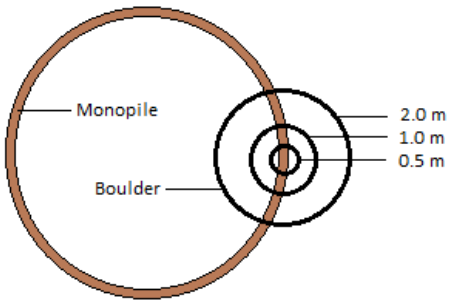

Figure 5.6: Considered sizes of the spherical boulder. Not to scale.

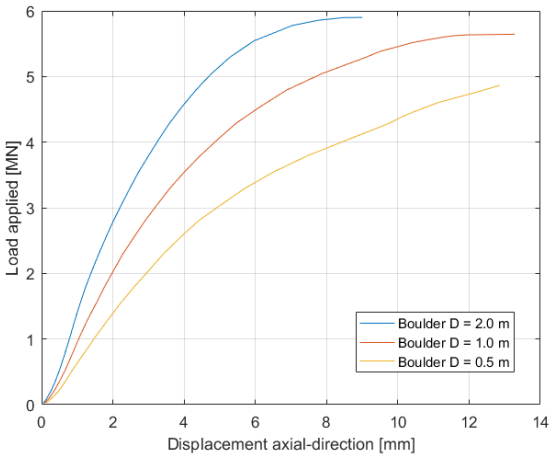

Figure 5.7: Applied load versus the axial displacement for different boulder sizes.

5.6. LATERAL AND AXIAL SOIL SUPPORT

As was described in previous Chapter, the soil stiffness around the pile was modelled by applying Winkler springs to the model. P-y and t-z springs were used to model the lateral soil resistance and axial shaft resistance, respectively. It was assumed that all the force at the pile tip is transmitted to the boulder, hence soil toe resistance (q-z curves) was not included in the model. In reality however, part of the force at the bottom of the pile is transmitted to the soil, reducing the deformation for the same applied load and therefore this assumption is conservative. Furthermore, it was assumed that the monopile is unplugged. Therefore the axial shaft friction inside the pile is included by multiplying the axial shaft friction outside the wall by a factor two. An approach was described to model the lateral soil support inside the pile as well. In this section the influence of modelling soil on pile tip damage is investigated. In all cases, the soil characteristics of a uniform medium-dense sand profile were used (Table 3.1). Again, it is ignored that the boulder can move in the soil matrix. If not mentioned otherwise, the embedded pile length of 15.0 m was used with a pile-boulder contact angle of 0 degrees, and a friction coefficient of 0.5 in the performed simulation in order to prevent the wall sliding over the boulder's surface.

5.6.1. LATERAL AND AXIAL SOIL RESISTANCE OUTSIDE THE MONOPILE

First the influence of adding lateral soil support outside the monopile was investigated. A view of the radial displacement at the bottom of the monopile for the situation without soil support and with soil support is seen in Figure 5.8a and Figure 5.8b respectively. The displacement in these plots is scaled by a factor five to clarify the deformation pattern. It is noticed that the deformation pattern is different. Since there is no outer soil support in Figure 5.8a, the whole bottom of the pile deforms as a consequence of collision with the boulder. This deformed bottom can be seen well since on the left side of the bottom of the pile, one can actually see the top of the pile at the end of the pile wall. The wall displaces outwards (in red) above and below the pile-boulder contact (ovalisation) as a result of inward pile deformation at the contact point, which matches the first linear buckling mode deformation pattern as was shown in Figure 5.4a. Including lateral soil support outside the monopile (Figure 5.8b) leads to a different buckling type. First it is seen that the deformation is more local and smaller, which is a more realistic scenario. Since the deformation is very local, the rest of the bottom of the pile remains intact and therefore in this situation, one cannot see the top of the pile along the wall. This is expected since the soil support prevents outwards deformation of the pile. It is seen that exactly at the contact point the wall deflect slightly inwards, resulting in a outward deformation a bit above the contact point.

Globally, the extra lateral soil support increases the maximum load that is potentially transmitted to the monopile significantly. A plot of the load versus the axial displacement at Node 2 is seen in Figure 5.9a. Here in blue (small short line) is the result of the run without any lateral soil support and in red the force-displacement curve for the run with lateral soil support caused by the uniform medium-dense sand profile. It it seen that the lateral support of the soil positively contributes to the global stability of the pile-boulder interaction. In this figure the yellow line is the result of additionally adding the shaft resistance (t-z curves) to

the model. Since part of the applied force is transmitted to these springs, the load that can be applied to the model before the model becomes unstable increases, however this axial soil component does not influence the local deformation behaviour. This was checked by integrating the load absorbed by the t-z springs and subtracting this load from the yellow (p-y + t-z curve). This results is seen by small blue dots in the same figure, overlapping the red p-y spring graph. Since the curves overlap the t-z springs do not influence the local deformation of the pile and is therefore currently not relevant to include. To compare the applied load with drive-ability analyses however, the axial resistance should be included as was done in the next chapter. Force-displacement curves results of varying the stiffness of the medium-dense sand profile within +-30 % are shown in Figure 5.9b. It is shown that initially the difference in soil stiffness does not influences the results, however after transmitting a load of 10 MN to the pile, the load-displacement curves start to diverge. Again, we see that that a higher soil stiffness (yellow line) improves the stability of the pile.

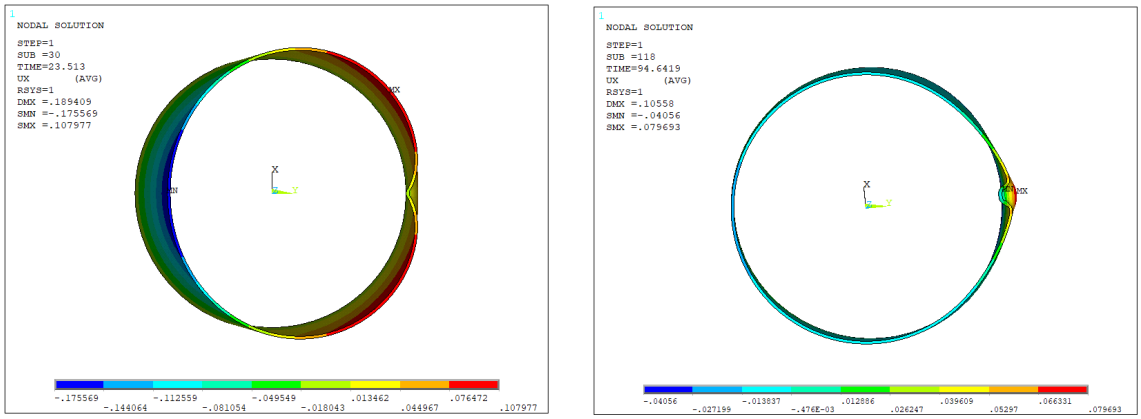

(a) (b)

Figure 5.8: (a) Monopile bottom view showing the radial displacement without soil support. (b) Monopile bottom view showing the radial displacement with lateral soil support outside the pile. In both (a) and (b) the deformation is scaled by a factor five for visualization purposes.

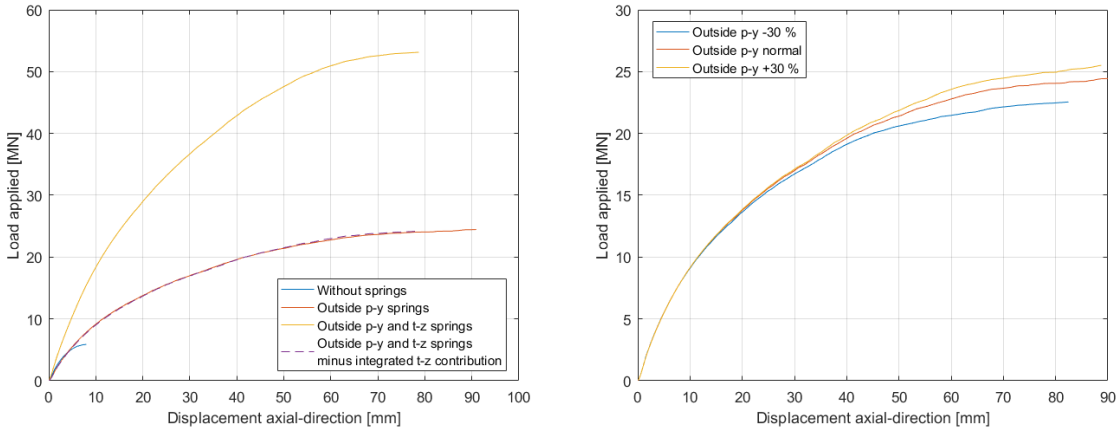

(a) (b)

Figure 5.9: (a) Applied load versus the axial displacement for the model without springs (blue), p-y springs (red) and p-y and t-z springs (yellow). In blue dashed lines (overlapping the p-y curve) the results of the integrated axial spring load subtracted from the yellow (t-z and p-y) curve. (b) Applied load versus axial displacement for the model where the lateral soil stiffness (normal in red) was varied within +30 percent (yellow) and -30 percent (blue).

5.6.2. LATERAL SOIL RESISTANCE INSIDE THE MONOPILE

In Section 4.4.1 a method was described to model the lateral component of the soil inside the pile, characterized by a young's modulus. In this report this method is called the volume element method. The influence of

adding lateral soil support inside the pile on pile tip damage is investigated in this section. A Young's modulus value for sand at a depth of 35.0 m, equal to 87.5 MPa (see Section 4.4.1) was selected to represent the lateral support of the soil inside. This value was not decreased for lower depths in the simulations. For more accurate simulations it is recommended to adapt the stiffness of the soil dependent on the depth as was for example described in Section 4.4.1. A 2D section-cut at the pile-boulder contact location is shown for the model without soil support inside the pile (Figure 5.10a) and with the inner soil support (Figure 5.10b). It should be noticed that for both cases also the outside soil support was modelled using the p-y curves described in previous section and the boulder's centre is aligned with the centre of the pile wall. The friction is again equal to 0.5 and the length of the model equals 15.0 m. From these figures it is seen that including lateral soil support inside the monopile results in a decrease in the local deformation of the pile wall (from 112 mm to 44.2 mm). This is logical since the included soil inside the pile makes the entire soil support stiffer. Due to this decrease, also the outward deflection slightly above the contact zone (in red in both Figure 5.10a and 5.10b) is decreased. Hence the local deformation of the pile is decreased and therefore it is concluded that lateral soil support inside the pile contributes to a decrease in local pile tip deformation. This matches expectations.

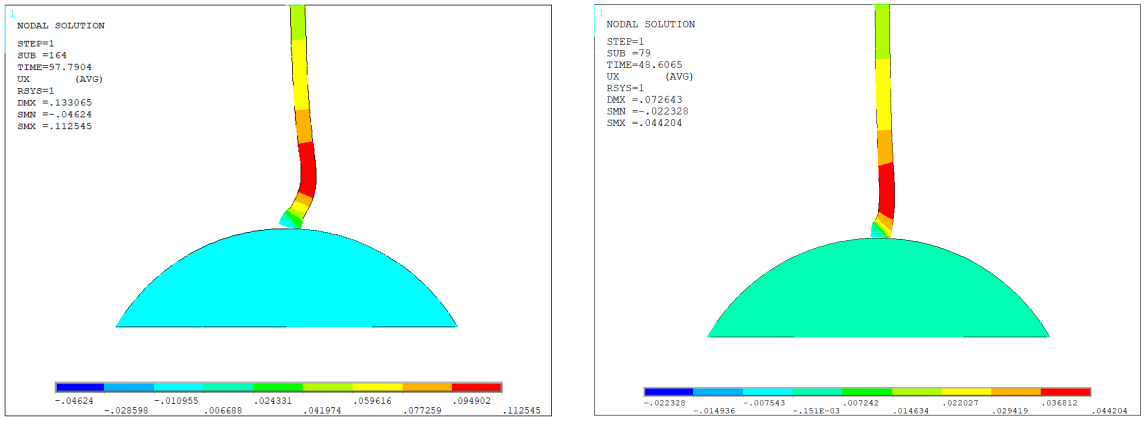

(a) (b)

Figure 5.10: (a) Radial displacement of the wall at pile-boulder contact without lateral soil resistance inside the pile. (b) Radial displacement of the wall at pile-boulder contact with lateral soil resistance inside the pile. In (a) and (b) the boulder is located symmetrically under the wall ($\alpha_{contact} = 0\,^{\circ}$), the friction coefficient is 0.5, and the applied load at the top of the pile equals 24.25 MN. True scale.

To verify the volume element (VE) method used to model the soil inside the monopile, their results were compared with the simulations were the same p-y springs connected to the outside of the pile were included inside the pile. These results should at least range in the same order of magnitude. If not, the accuracy of the VE method is likely to be insufficient. Simulations were performed for a positive and negative pile-boulder contact angle of 10 degrees. The friction coefficient used in this simulation is 0.3 and the model length is 10.0 m, similar and explained in the following Section 5.8. The result of the runs are presented in Figure 5.11. The dotted lines show the simulations where the outside soil p-y springs are used for the soil inside the monopile and the full lines show the runs with the VE model calibrated linear Winkler springs used inside the pile. In the figure it is seen that the dotted lines are slightly higher than the full lines, which indicates that the maximum load able to be applied to the p-y model is higher than for the VE model. The difference is minimal, however since the VE model results in slightly more deformation at the same load, the VE model is used to highlight the deformation mechanisms.

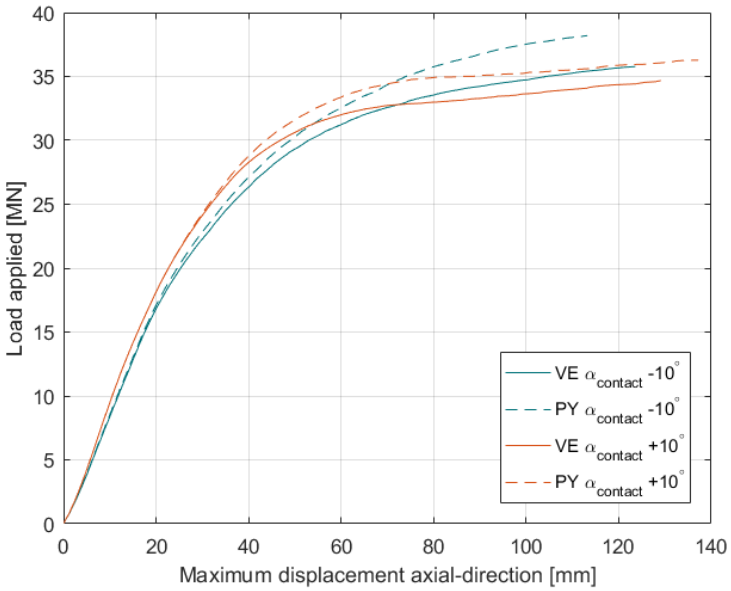

Figure 5.11: Applied load versus axial-displacement for contact angles -10 and +10. VE refers to volume elements inside the pile and PY indicates that the outside PY springs were applied to the inside of the monopile.

5.7. THE FRICTION COEFFICIENT

In 'Measurements of dynamic friction between rock and steel' (Defense Nuclear Agency, 1976) the dynamic friction coefficient for steel-rock contact was measured and varies between 0.39 and 0.5 for dry rocks. In this study it is furthermore mentioned that the presence of water seems to reduce the coefficient. The upper bound of the dynamic friction for steel-rock contact equal to 0.5 was initially chosen to prevent the pile from sliding over the boulder's surface. In the following simulations, the boulder was located inside the pile resulting in an contact angle of -20 degrees. Both the angle and lower friction coefficient were suspected to influence the pile-boulder interaction. This influence of the angle is discusses in the next paragraph, Section 4.5. Friction coefficients were varied in the range 0.2 to 0.5. Lower friction values do not seem realistic as is discussed at the end of this paragraph. Simulations were performed for a 10.0 m embedded monopile, a boulder diameter of 2.0 m, and the pile-boulder angle of -20 degrees. In these runs lateral- (inside + outside the pile) and axial soil support was included in the model to help ANSYS converge the solution. Results of the applied load versus the axial displacement for the simulation with different friction coefficients is depicted in Figure 5.12. It is clearly seen that the friction coefficient effects the results when the pile hits the boulder under an angle. The lower the friction coefficient, the sooner the force-displacement plot converges, hence the lower the applicable static load and the sooner the model becomes unstable.

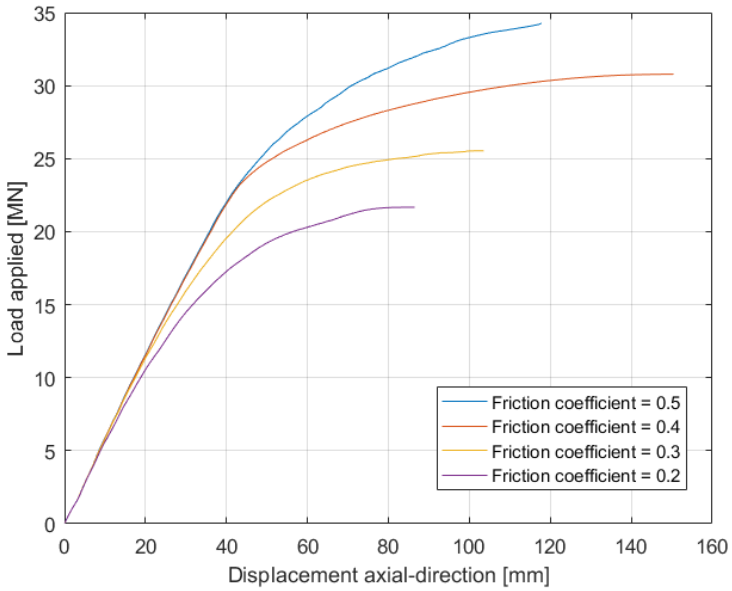

Figure 5.12: Applied load versus the axial displacement for simulations with different friction coefficients. The boulder is located inside the pile, hitting the pile under an angle of -20 degrees.

It is now interesting to investigate the difference in the curves that where shown in Figure 5.12, in more detail. This was done by inspecting the local deformation area at the pile-boulder interaction zone. A section-cut of the pile-boulder interaction for the 0.5 friction coefficient at its final load step of 34.3 MN is seen in Figure 5.13a and for the final load step of 30.8 MN for the 0.4 friction coefficient in Figure 5.13b. In Figure 5.13 the black wall lines represent the starting position of the pile, hence at zero applied load. It is shown that for the final load step of the 0.5 friction run (Figure 5.13a), the pile almost does not slide over the surface of the boulder and that the wall locally deforms above the contact area. The high friction value between the pile and boulder keeps the pile wall in place at the contact area on the boulder. Looking at the section-cut of the 0.4 friction coefficient simulation in Figure 5.13b, it is clearly seen that the pile slides over the surface of the boulder due to the decrease in friction. It can be seen that at 24.9 MN the pile starts to slide over the surface of the boulder and this explains the divergence point of the blue and red curve in Figure 5.12 and their difference in static load limit. The final load step deformations for the 0.5 and 0.4 friction coefficient runs are shown in 3D in Figure 5.14a and 5.14b respectively. The displacement in these plots was scaled by a factor three to clarify the deformation pattern. In these figures it is seen that the deformation shape is different. Sliding causes a ovality type of non-linear deformation, whereas non-sliding causes rippling/folding of the wall like the harmonic instrument. One can imagine that continuing pile-driving after these deformations might lead to serious damage to the pile tip. These differences and implications are more clearly distinguished and discussed in Section 5.8. Looking at the other two lower friction coefficient (0.3 and 0.2) simulations, it was seen that the lower the friction coefficient, the earlier the pile starts to slide over the surface of the boulder. This intuitively makes sense. Results of the static load limit (applied load at which the pile becomes unstable), the load that initiates sliding of the pile over the boulder's surface, and the maximum radial displacement (at the lowest static load limit, thus 21.7 MN) are presented in Table 5.2. As seen, the static load limit matches the asymptotic values shown in Figure 5.12. By looking at the maximum radial displacement of the deformed wall section with respect to the centre of the bottom of the pile, it is seen that the displacement is larger for lower friction coefficients and this is a confirmation of the sliding of the pile over the boulder's surface. The jump in radial displacement from the 0.3 (53.8 mm) to 0.2 (131.8 mm) friction coefficient can be explained since at 21.7 MN the pile is at it's sliding end (static load limit) of the 0.2 simulation and slides just a little in the 0.3 simulation, as is seen in their curves shown in Figure 5.12.

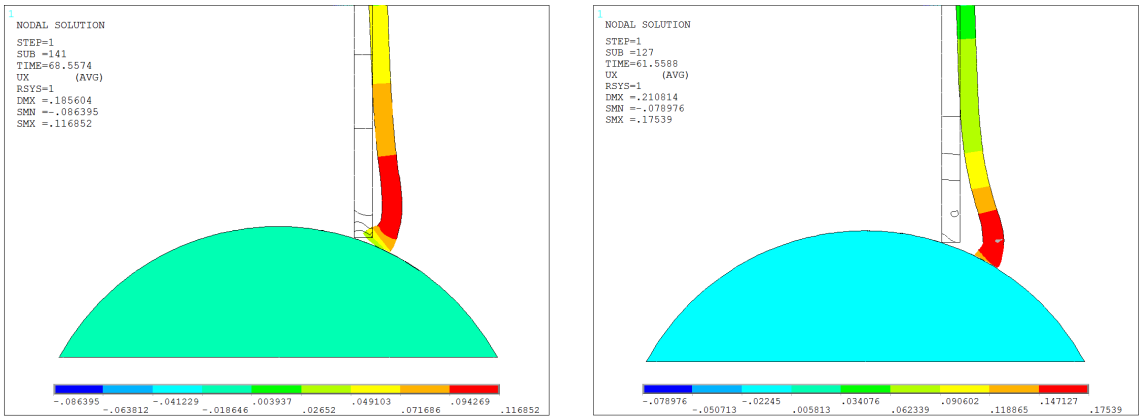

(a) (b)

Figure 5.13: (a) Section-cut of the final load step of 34.3 MN for a steel-rock friction coefficient of 0.5. (b) Section-cut of the final load step of 30.8 MN for a steel-rock friction coefficient of 0.4. In both (a) and (b) deformations are on true scale.

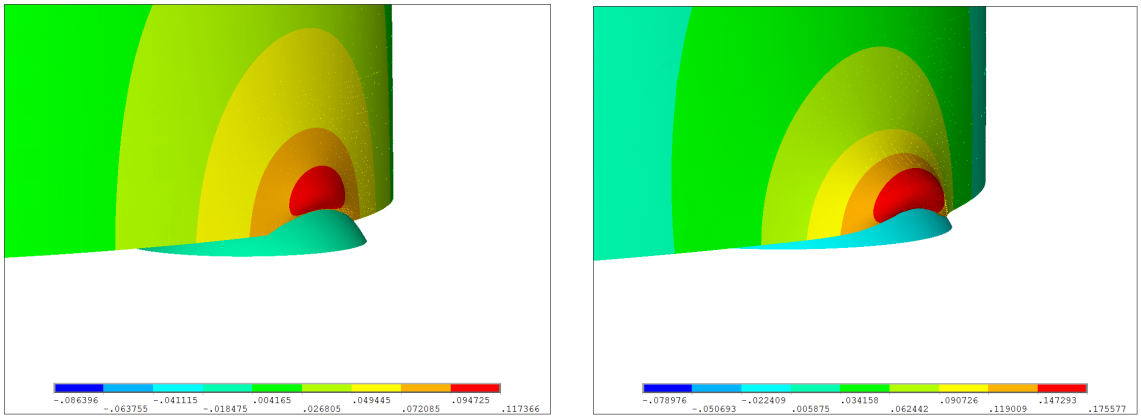

(a) (b)

Figure 5.14: (a) 3D plot of the radial displacement for the final load step of 34.3 MN for a steel-rock friction coefficient of 0.5. (b) 3D plot of the radial displacement for the final load step of 30.8 MN for a steel-rock friction coefficient of 0.4. In both (a) and (b) deformations were scaled by a factor three for visualization purposes.

Referring back to literature studies, in the 'Measurements of dynamic friction between rock and steel' (Defence Nuclear Agency,1976) the dynamic steel-dry rock friction range of 0.39-0.5 was mentioned. When water and/or mud is present, the friction coefficient decreases. In reality, the pile will always penetrate the boulder somewhat and this is likely to increase the steel-rock friction again. Therefore the friction coefficient between 0.3 and 0.4 was determined to be appropriate to select. It was shown that a smaller friction coefficient leads to earlier sliding of the wall over the boulder's surface and thus a different failure mechanism than when the pile wall ripples due to the bottom sticking to the surface of the boulder. The purpose of this research is to investigate the different causes of failure mechanisms. The failure mechanism are dependent on both the friction and contact angles. Since the different failure mechanism can be clearly identified combining the friction coefficient of 0.3 with different boulder angles, (discussed in Section 5.8), a coefficient of 0.3 was chosen as the steel-rock friction value.

Table 5.2: Influence of the friction coefficient for a 10.0 m embedded pile, hitting a boulder at an angle of -20 degrees.

Friction coefficient [-]	**Static load limit [MN]**	**Initiating sliding Load [MN]**	**Max radial displacement at load 21.7 MN [mm]**
0.5	34.3	-	29.6
0.4	30.8	24.9	30.3
0.3	25.5	15.0	53.8
0.2	21.7	9.8	131.8

5.8. THE POSITION OF A BOULDER

To investigate the influence of the asymmetric pile-boulder contact, the size of the spherical boulder was fixed using a diameter of 2 m (r equal to 1) and the pile geometry is kept constant as well. The standard geometry of a D/t equal to 100 (D = 7.4 m, t = 0.074 m) was used again for this analysis. As was discussed in Section 5.7, a steel-rock friction coefficient of 0.3 was chosen. The contact angle $\alpha_{contact}$ (defined in Section 4.5) was varied using the values shown in Table 5.3. Larger angles are not interesting to review since these angles will just result into quicker sliding of the pile wall over the boulder's surface, as is shown below.

Table 5.3: Varying the contact angle

Pile-boulder contact angle α [°]						
+30	+20	+10	0	-10	-20	-30

Asymmetric contact between pile and boulder complicates the calculations in ANSYS. When the centre of the boulder was located some distance away from the centre of the wall, the boulder also starts making contact with the inside or outside of the wall. The combination of contact with the bottom and in- our outside of the pile wall required significantly more computational time. Convergence of the solution was established by decreasing the load step size and including p-y curves of a uniform medium sand profile (see Section 5.6) to model the lateral resistance of the soil outside the pile. Also the lateral soil support inside the pile was included in the model using the volume elements method as was described in previous section and the axial shaft resistance was included using the t-z springs.

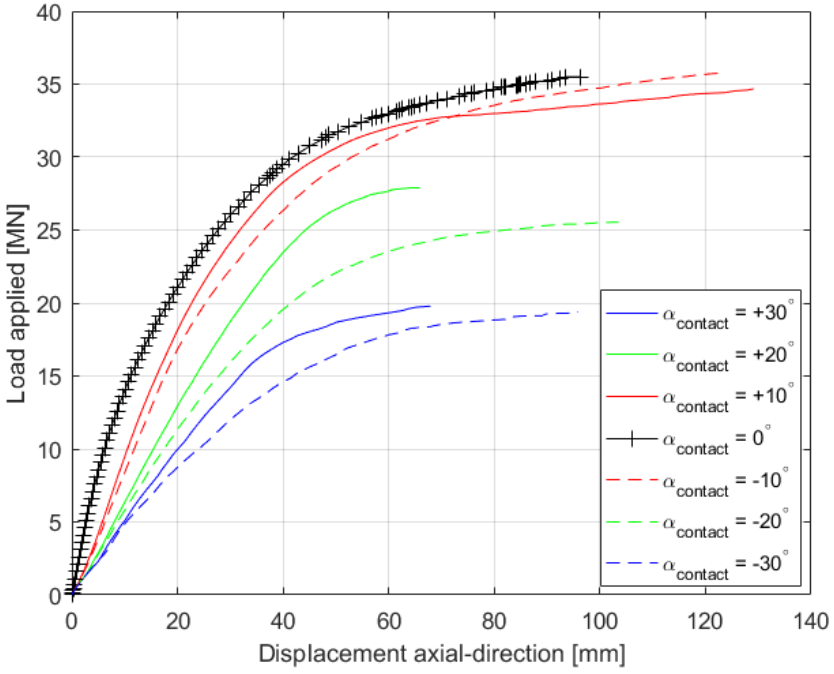

Figure 5.15: Applied load versus axial-displacement for varying contact angles.

The force-axial displacement results for runs with different positions of the boulder under the pile's wall are shown in Figure 5.15. The vertical displacement was checked at the top of the pile (Node 2 Figure 4.1b), since the radial-displacement is visually less clear to inspect due to the pile-soil interaction. The vertical displacement at the top of the pile is a good indicator to check the global response of the pile due to the local deformation at the bottom of the pile. Again, the curves end at the maximum load that one is statically able to apply to the model. The convergence stopped when the elements are too deformed or when static equilibrium was not found after sliding of the pile over the boulder's surface. In the plot the negative angles are shown by the dotted lines (the centre of the boulder positioned inside the pile wall) and the positive angles by the full lines (the centre of the boulder positioned outside the pile wall). The boulder located symmetric under the pile wall is shown by the black line with the plus symbol in it. In this plot it is seen that the pile behaves stiffer when the boulder is located exactly symmetric under the pile wall (black line). This physically makes sense since the force is distributed better along the wall. When the boulder is located inside or outside the pile hitting the pile under an angle, the pile behaves less stiff. The static load limit (converged values) is quite similar for the angles between -10 and + 10 degrees as presented in the Figure by the red curves. Clearly the static load limit decreases for angles larger than +10 degrees and smaller than -10 degrees. For the large +30 and -30 degrees angle, the behaviour of the pile is the least stiff and the static load limit is the smallest as can be seen by the blue curves in Figure 5.15. It is therefore concluded that the +30 and -30- degrees angle simulations result in the fastest static stability problems. As was done in comparing the friction coefficient (Section 5.7), the local behaviour of the pile-boulder interaction should be inspected to find the failure mechanism that leads to the static instability that is reached at the end of the curves shown in Figure 5.15. This was done next.

Radial displacement results on true scale in a 2D section-cut through the wall and boulder for the different angles are shown in Figure 5.16a, 5.17a, 5.18a, 5.19a, 5.20a, 5.21a, and 5.22a. These are the results of the final load step of each simulation, hence at the end of the graphs shown in Figure 5.15. Again, the black lines represent the original/starting position of the pile-boulder interaction process, hence at zero force. It is interesting to see that for the cases (-10 $^\circ \leq \alpha_{contact} \leq +20^\circ$) the bottom of the pile sticks to the surface of the boulder. This means that for these cases, the 0.3 friction is high enough to keep the boulder in place and the pile locally deforms significantly before sliding over the surface of the boulder. For the angles < -10 $^\circ$ and > +20° however, the pile starts to slip and slide over the surface of the boulder. More precise, it is seen that for the -20 degrees (Figure 5.21a) the pile clearly slides over the boulder, however stays in place for the +20 degrees simulation (Figure 5.17a). Having the boulder located on the inside of the pile (minus angles) creates an outward force resultant. A cylinder can however resist outward forcing better than inward forcing due to the effect of membrane and hoop stresses developing in the steel. Instead of deforming like in the +20 degrees case, this explains why for the -20 degrees the pile prefers to slide over the boulder's surface. Furthermore, for the angle -10 $^\circ \leq \alpha_{contact} \leq 10^\circ$, the outward or inward deformation seems relatively large and sort of curves around the original pile wall position. This phenomenon looks like rippling of the wall. Since in these cases the pile does not slide off the pile surface and ANSYS can model this rippling quite well, the loads that can be transferred to the pile are relatively large and this matches the the red and black curves in Figure 5.15. To extract more information from the different runs, the final deformation in 3D at the end of the force-displacement curves should be investigated.

The radial displacement in 3D for the different angles at the their final load step is shown next to the 2D figures, in Figure 5.16b, 5.17b, 5.18b, 5.19b, 5.20b, 5.21b, and 5.22b. The deformation was scaled by a factor three to clarify the different deformation patterns. The deformation mechanisms can be better seen than in the 2D plots and three deformation types were distinguished:

1. Local inward deformation of the wall (local ovalisation) ($\alpha_{contact} \geq +20^\circ$)
2. Local rippling (folding) of the wall (-10 $^\circ \leq \alpha_{contact} \leq +10^\circ$)
3. Local outward deformation of the wall (local ovalisation) ($\alpha_{contact} \leq -20^\circ$)

As was mentioned in the previous friction section, it is again clearly shown that the combination of friction and boulder angle influence the deformation mechanism significantly. Local inward deformation of the wall is seen for the $\alpha_{contact} \geq +20^\circ$ case. The local inward deformation results into outward deformation next to the indented zone (red cheeks in Figure 5.16b and 5.17b). Local rippling (folding of the wall like the har-

monic instrument) seems to occur for the angles -10 ° ≤ $\alpha_{contact}$ ≤ +10°. Finally, local outward deflection of the wall (local ovalisation) seems the happen when the wall slides over the surface of the boulder, which happens for the angles $\alpha_{contact} \leq -20°$. This matches the sliding result in the 2D section-cut plot shown by Figure 5.21a and 5.22a. The local outward deformation after sliding of the pile over the surface of the boulder caused by the contact angle ≤ −20° is similar as the deformation after sliding caused by the low friction coefficients presented in Section 5.7. As was shown by the 2D angles plots, sliding also occurs for positive contact angles > +20°. It was furthermore shown that at the contact point the wall of the monopile is easier deflected inwards than outwards in most cases: for the angles -10 ° ≤ $\alpha_{contact}$ ≤ +10° (rippling mechanism). This matches known physical properties of a cylinder that is locally deformed easier inwards than outwards (membrane/hoop stresses) as was mentioned before. This initial inward deflection is depicted very clearly by plotting the bottom of the pile. For the -10 degrees run, the inward deflection is clearly seen in Figure 5.23. The inward deflection is followed by an outward deflection of the wall slightly above which is why it's called the rippling of the wall.

In this section it was shown that different pile-boulder contact angles lead to different deformation mechanisms. Which deformation type leads to worse pile damage cannot be stated as a fact, as it largely depends on the propagation of the damage. Inward deformation might propagate and might lead to total closure of the pile tip as was pointed out in the introduction, Figure 1.3. Also propagation of a rippled area might propagate and have serious consequences. Continue hammering on a pile with a locally outward deflected bottom might propagate fracture the pile like a zipper.
Related to the damage propagation, the depth at which the deformation occurs is important. The obtained deformations do not matter when they occur close to the target penetration depth. However, when deformation is initiated at depths significantly above the target penetration depth, damage propagation might become a serious issue. This also highlights the importance of boulder detection. Damage propagation is very interesting to investigate in further research and this is described in more detail in Section 8.3. It should also be noticed that similar as was discussed in Section 5.2, local strains exceed the fracture strain of 21 %. Local fracture might change the deformation mechanism and should be considered in further studies.

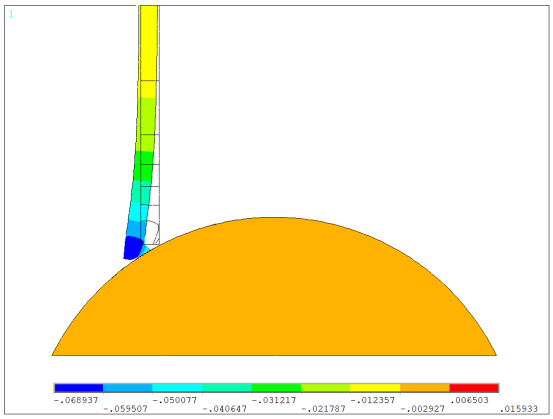

(a) +30 °

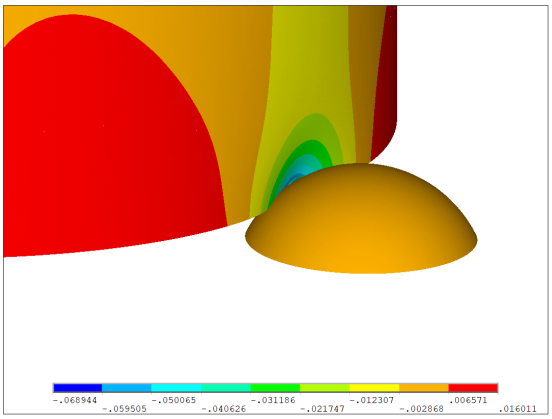

(b) +30 °

Figure 5.16: 2D plot (a) and 3D plot (b) of the radial displacement for a contact angle of +30 ° at maximum applied load.

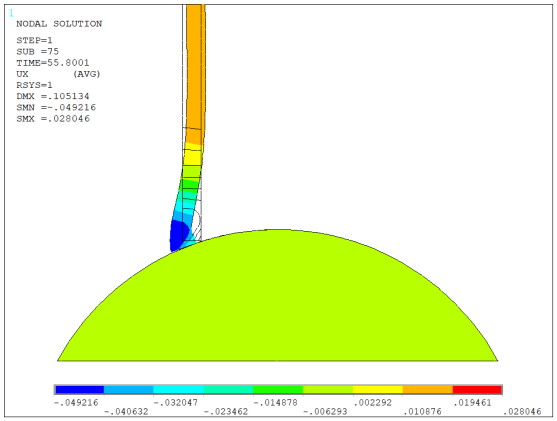

(a) +20 °

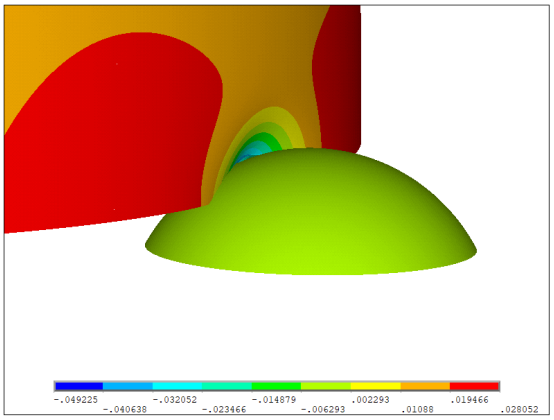

(b) +20 °

Figure 5.17: 2D plot (a) and 3D plot (b) of the radial displacement for a contact angle of +20 ° at maximum applied load.

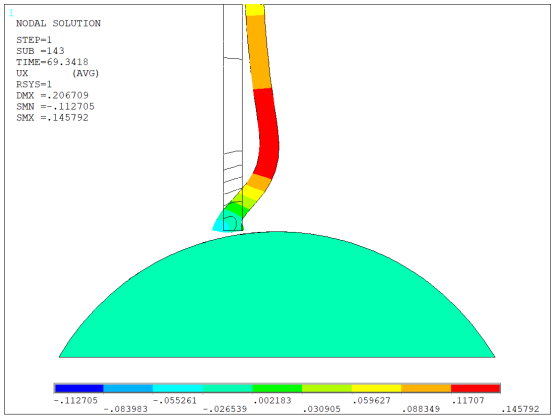

(a) +10 °

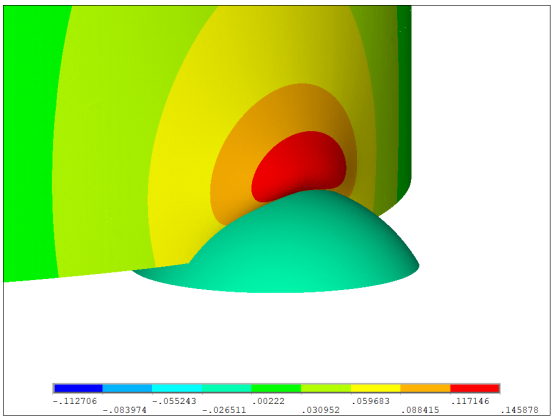

(b) +10 °

Figure 5.18: 2D plot (a) and 3D plot (b) of the radial displacement for a contact angle of +10 ° at maximum applied load.

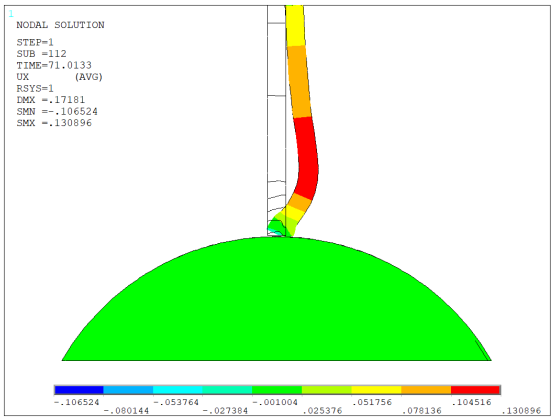

(a) 0 °

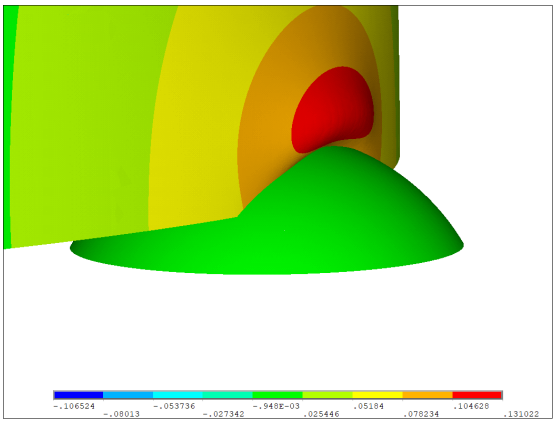

(b) 0 °

Figure 5.19: 2D plot (a) and 3D plot (b) of the radial displacement for a contact angle of 0 ° at maximum applied load.

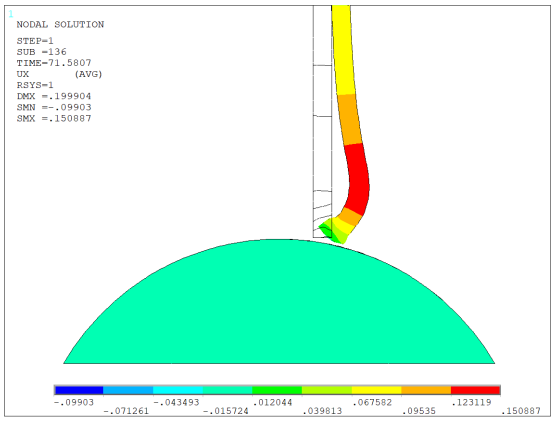

(a) -10 °

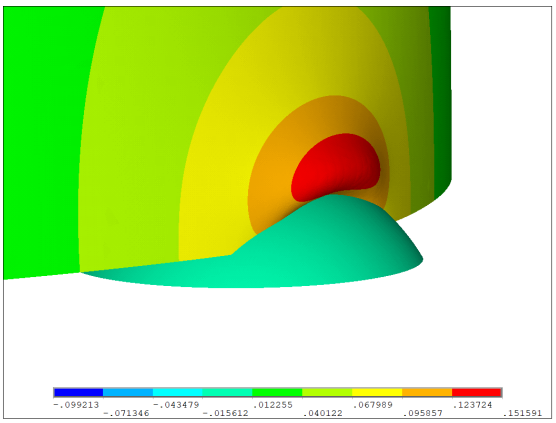

(b) -10 °

Figure 5.20: 2D plot (a) and 3D plot (b) of the radial displacement for a contact angle of -10 ° at maximum applied load

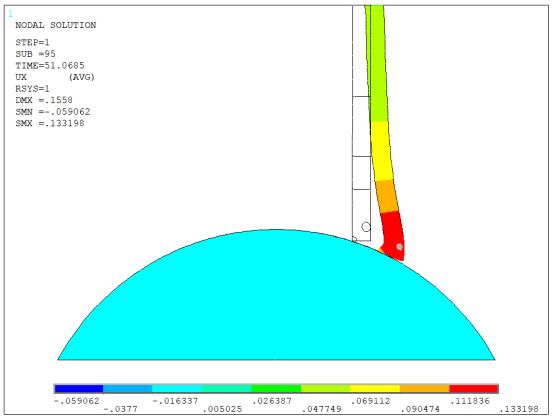

(a) -20 °

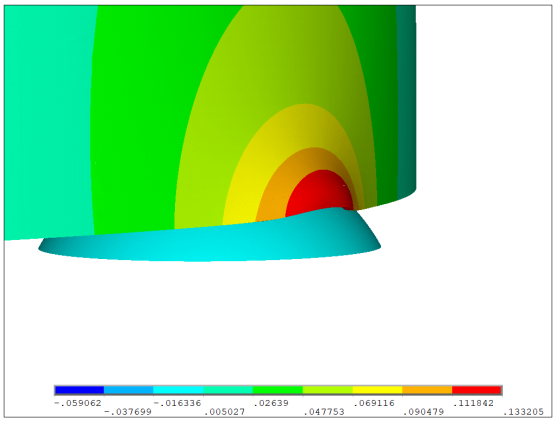

(b) -20 °

Figure 5.21: 2D plot (a) and 3D plot (b) of the radial displacement for a contact angle of -20 ° at maximum applied load

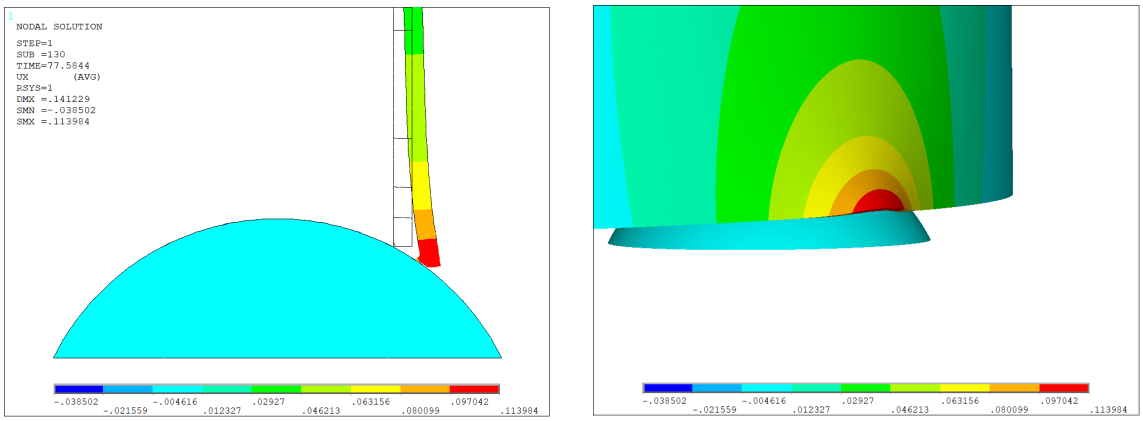

(a) -30 ° (b) -30 °

Figure 5.22: 2D plot (a) and 3D plot (b) of the radial displacement for a contact angle of -30 ° at maximum applied load

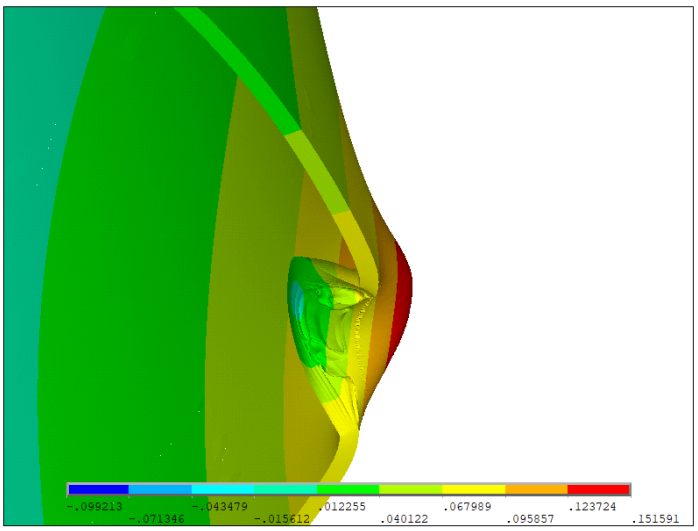

Figure 5.23: Bottom view of the radial deformation at the final load step (36.1 MN) for the pile-boulder contact angle of -10 degrees (corresponding to Figure 5.20b). The steel-rock friction coefficient equals 0.30, the pile length is 10.0 m, and the boulder diameter is 2.0 m. Lateral- and axial soil support in- and outside the pile are included. The deformation is scaled by a factor three.

5.9. A BOULDER EMBEDDED IN SOIL

So far the boulder was fixed, hence unable to move. This might be representative in the cases that the soil is stiff enough to keep the boulder in place. In many cases however, the boulder is likely to be displaced into the soil due to impact with the monopile. Displacement of the boulder depends on soil characteristics, load acting on the boulder and size of the boulder itself. When the boulder is pushed downwards, the resistance is likely to increase again and the boulder will be pushed downwards again at the next hammer blow. Inertia of both boulder and monopile play a role in this dynamic process and modelling this dynamic process is out of the scope of this research project. In these simulations the boulder is therefore fixed in vertical direction, which leads to the pile tip deformation that is of interest in this project. If the boulder is likely to move in vertical direction might be estimated by bearing capacity equations as was shown in Chapter 3. In reality, the pile will always hit the boulder under an angle, resulting in a horizontal force component acting on the boulder. The boulder might actually be pushed sideways, changing the boulder-pile interaction process. By embedding the boulder in a Winkler spring environment, it was attempted to model the effect of the sideways deflecting boulder. The effect of the displacement on local deformation and the global stability of the pile was investigated. Again, medium-dense sand soil properties were used and the p-y value was corrected for the boulder diameter and the depth of the location of the boulder according to Equation 4.10. Since the spring

stiffness was determined using the API (API-RP-2-GEO, 2011), the stiffness was calculated for an embedded square. The cross area of a sphere is smaller than that of a square and therefore the stiffness was multiplied by a factor 2/3. Note that this is a very simple approximation.

To investigate the horizontal displacement of the boulder, the embedment depth of the pile and boulder was again selected at 10.0 m. Low embedment depths generally lead to softer soil environments, which will cause earlier horizontal displacement of the boulder. As was done before, lateral and axial soil support was included in the model, the friction coefficient equals 0.3, and the boulder's diameter is equal to 2.0 m. Results of the force versus the axial displacement at Node 2 for the embedded boulder runs for the negative contact angles are shown by the dotted lines in Figure 5.24a. Due to the significant calculation time and the limited available time in this thesis, the boulder displacement effects were not simulated for the positive angles. The previously obtained results of the parametric angle investigation (Section 5.8) are shown for the same angles in Figure 5.24a as well by the full lines. As is seen in this figure, for the -10 degrees contact angle (red curves), the embedded and fixed boulder simulation results match well. This means that the boulder does not, or barely, moves in horizontal direction. For the -20 and -30 degrees angle (green and blue lines respectively) however, the curves clearly diverge. This indicates that for these larger contact angles, the horizontal component acting on the boulder is large enough to horizontally push the boulder into the soil. Pushing the boulder away in horizontal direction can be seen well for the -20 degrees case in a 2D plot, Figure 5.25. Here the black lines represent the original position of the boulder, and the blue boulder represents the new position of the boulder at the final load step (hence the load at the end of the green dotted curve in Figure 5.24a and 5.24b. The applied load versus the maximum axial-displacement for the same considered angles simulations is presented in Figure 5.24b. It was seen that for the -10 degrees angle, the boulder was displaced 3.4 mm in the horizontal plane, which explains the overlapping graphs. The displacement was checked by a quick hand-calculation were the horizontal reaction force on the boulder from ANSYS (.59E6 MN) was divided by the linear part of the p-y curve of the boulder (156 MN/m). This leads to a similar displacement of 3.8 mm. This displacement is very small and the soil is thus stiff enough to keep the boulder in-place. As expected, the radial displacement for the larger angles and embedded boulders (dotted green and blue lines) differs significantly from the fixed boulder simulations (full green and blue lines). It can be seen that the blue and green dotted lines reach a much smaller radial displacement than the blue and green full lines. This means that due to the horizontal displacement of the boulder, the damage to the pile tip is reduced. However, damage is still initiated and might propagate when pile-driving is continued.

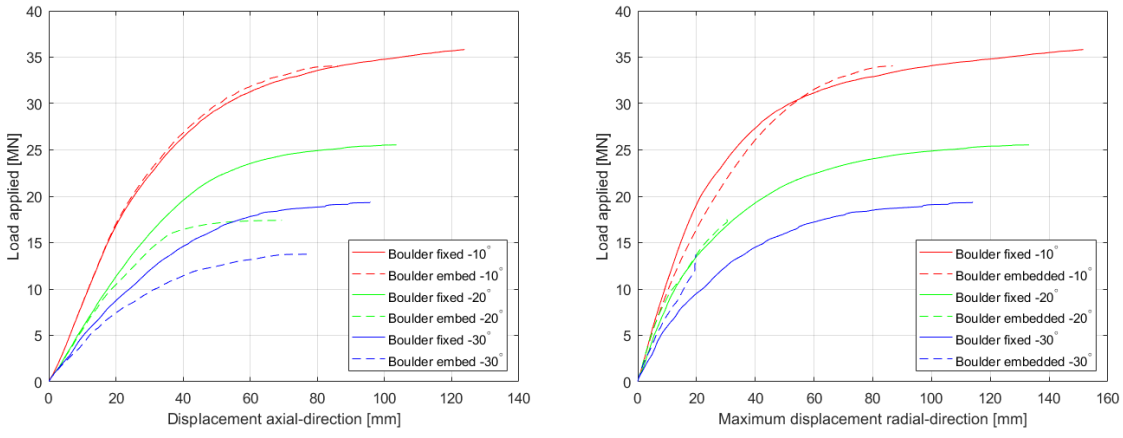

(a) (b)

Figure 5.24: (a) Applied force versus the axial displacement for varying boulder angles. (b) Applied force versus the maximum radial displacement for varying boulder angles. In (a) and (b) the dotted lines represent the simulations were the boulder was horizontally embedded in a spring environment and the full lines represent the simulations were the horizontal movement of the boulder was fixed.

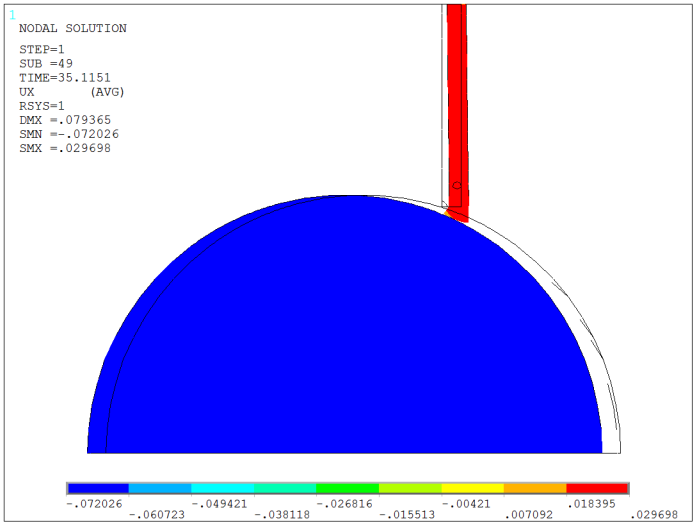

Figure 5.25: Radial displacement of a simulation with the boulder horizontally embedded in springs. Shown at the final load step for a contact angle of -20 degrees.

6

PILE TIP DAMAGE RELATED TO BOULDER FAILURE AND DRIVE-ABILITY

6.1. INTRODUCTION

In the static model the maximum force able to be transmitted to the pile was shown for different scenarios where the boulder was assumed to be intact. This force might however cause local deformation of the surface of the boulder or even split the boulder. This force should also be compared to typical hammers used in the offshore industry, to check if these hammers are able to deliver this kind of force. These topics are discussed in this chapter.

6.2. RELATING DAMAGE TO FAILURE OF THE BOULDER

Two failure mechanisms of the boulder were described in Section 3.3: local failure of the boulder's surface into zones and splitting of the boulder. Local deformation of the boulder is initiated if the contact stress on the boulder is larger than the bearing capacity of 851 MPa for granite and 296 MPa for sandstone, as was seen in Table 3.2. Considering the case where the boulder is not likely to push away the boulder (Section 5.9) of -10 degrees and causing rippling of the wall, the maximum force able to be transmitted to the boulder is 25.0 MN. This is the maximum load transmitted to the pile of 35.6 MN, minus the load of 10.6 MN absorbed by the axial springs. Considering an average stress distribution over the pile contact area on the boulder equal to 0.051 m^2 (approximated by inspecting the contact area length and width), this results in a stress of 490 MPa. Comparing this stress with the bearing capacity of granite and sandstone, it is noticed that the stress acting on the boulder exceeds the bearing capacity of sandstone, however is lower than the bearing capacity of granite. This indicates that the pile is able to cause local failure on the surface of relatively soft rocks, however is unlikely to penetrate into hard rocks such as granite. When the pile penetrates soft rocks, the increased contact area will reduce the contact stress however, which might still lead to deformation of the pile. Penetration of the pile into the boulder might reduce the sliding effect of the pile over the boulder. A higher friction coefficient might than be more realistic to apply to the pile-boulder interaction.

Substituting the force of 25.0 MN, a radius of 1.0 m, and a length of 0.69 m into the Brazilian test formula (Equation 3.10) results in a tensile strength of 11.5 MPa. Comparing this tensile strength to a reference tensile strength for limestone of 38.76 MPa (Amadai, 2015), it is seen that this tensile strength is not exceeded, hence spitting of the rock is not likely to occur. It should be noticed that in this approach all the force at the bottom of the pile is assumed to be transmitted to the boulder. This is conservative, in reality part of this force will also be absorbed by the soil under the pile. For smaller boulders, for example when the radius of the boulder equals 0.5, and considering similar force and contact area, the tensile strength results into 21.3 MPa. This is still lower the 38.76 MPa strength of limestone, however one can imagine see the trend that the smaller the rock, the less likely it will fail by splitting.

6.3. RELATING DAMAGE TO DRIVE-ABILITY ANALYSES IN GRLWEAP

The hammer energy and resulting pile driving stresses were related to the static model by combining pile drive-ability data from GRLWEAP (GRLWEAP, 2010) with the static numerical model. This was done in order to check if offshore hammers are able to deliver the kind of force needed to severely damage the pile tip. The stress output from GRLWEAP at refusal was compared with the ANSYS simulations. It should be noticed that this comparison is a very rough estimation performed only to have a general idea of the amount of force current offshore hammers can deliver, and related to the tip deformation.

Two different depths were chosen were a hard soil layer was modelled in GRLWEAP to represent a boulder: 15.0 m and the target penetration depth of 29.25 m. The in offshore frequently used IHC-S4000 hydraulic hammer was selected with its specifications shown in Table 6.1. The toe resistance at the mentioned two depth levels was increased to initiate refusal. Van Oord's refusal criteria of 125 blows per 1.5 m or a total of 250 blows was used. Furthermore, the axial shaft resistance of medium-dense sand was included in the GRLWEAP model, as was done in the ANSYS model. A screen-shot of the GRLWEAP input at 29.25 m depth is seen in Figure 6.1. Here the triangular profile represents the linear increasing shaft friction (multiplied by a factor two to also represent the shaft friction inside the pile) and the L- profile represents the sudden high tip resistance theoretically caused by the boulder. The maximum compression stress output of GRLWEAP is shown in Table 6.2 for different depths and D/t ratios of the full size monopile that was presented earlier, in Figure 4.1a. The values shown in Table 6.2 relatively make sense; the maximum stresses increase for larger D/t ratios. Furthermore, the stresses decrease with larger depths. This is caused by the fact that drive-ability analyses in GRLWEAP uses the maximum stroke for each blow and the axial soil resistance increases with depth, hence reducing the force transmitted to the tip of the pile.

Table 6.1: IHC-S400 specifications

Description	**Value**	**Unit**
Type	IHC-S4000	
	Direct drive, no cushion	
Ram weigth	1977.15	kN
Energy	3999.78	kJ/kW
Efficiency	2.02	[-]
Stroke	0.95	m

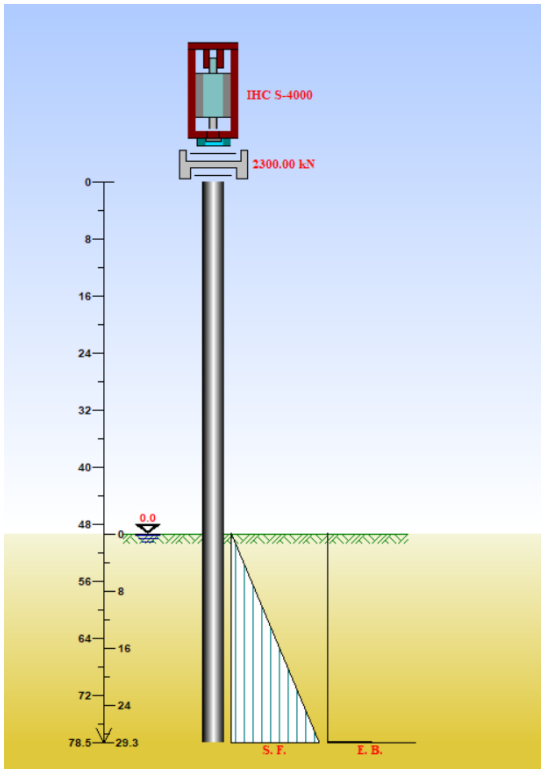

Figure 6.1: Screen-shot of the drive-ability simulation in GRLWEAP. Shown are the hydraulic IHC-S4000 hammer, the pile, shaft resistance (triangle), and sudden high tip resistance representing a boulder or hard soil layer

Table 6.2: Maximum compression stress in the pile from GRLWEAP for varying D/t ratios and boulder depths at pile refusal.

	D/t [-]	**Boulder depth [m]**	**Max compression Stress [MPa]**
D increase	60	15	235
	60	29.25	217
	100	*15*	*174*
	100	*29.25*	*157*
	140	15	134
	140	29.25	134
t increase	60	15	125
	60	29.25	125
	100	*15*	*174*
	100	*29.25*	*157*
	140	15	212
	140	29.25	188

Considering the base case pile geometry (D/t = 100) with a diameter of 7.40 m and a thickness of 0.074 m, 15.0 m embedded, this leads to a maximum compression stress in GRLWEAP of 174 MPa (Table 6.2). Multiplying this value by the cross section area of the pile (1.7 m^2), this results into a force equal to 296 MN. Comparing this to the static load limit of 35.6 MN, this indicates that offshore hammers can definitely exceed the static load limit and it is therefore shown that the hammer can deform the pile tip significantly. It should be noticed that the 35.6 MN force was the output of the 10.0 m static model and therefore not directly comparable to the 15.0 m depth used in GRLWEAP. However, as was discussed in this section, a depth of 10.0 m will cause even higher stresses at refusal than at 15.0 m depth and therefore it is still concluded that current offshore hammers can cause the local damage to the pile tip that was shown in previous chapter.

7

NUMERICAL MODEL - DYNAMIC

7.1. INTRODUCTION

The focus of this MSc thesis research was on the variety of static influences on damage to the pile tip and the resulting failure mechanisms. In this chapter a single dynamic run was performed to compare the dynamic with the static results. With 'dynamic run' it is meant that instead of gradually increasing a static load applied to the monopile, a pulse over time that is caused by the hammer blow, works on the monopile. It should be noticed that a lot that is mentioned in this chapter is not well substantiated since thorough dynamic analyses is out of the scope of the MSc thesis. The single dynamic run described in this chapter should be seen as a start for a dynamic approach to the problem, which can be done in future studies.

7.2. SET-UP OF THE DYNAMIC RUN

Matching the input for a run performed in the static model, the boulder is located at 10.0 m depth, the pile-boulder contact angle is -10 degrees, the friction coefficient equals 0.3, and the diameter of the boulder is 2.0 m.

7.2.1. DYNAMIC HAMMER PULSE

A hammer pulse from the hydraulic MENCK MHU3500 hammer, at full power for a monopile with a top diameter equal to 6.5 m, was provided by Van Oord. This time signal is presented in Figure 7.1. The duration of the pulse is approximately 0.01 s, hence 10 ms.

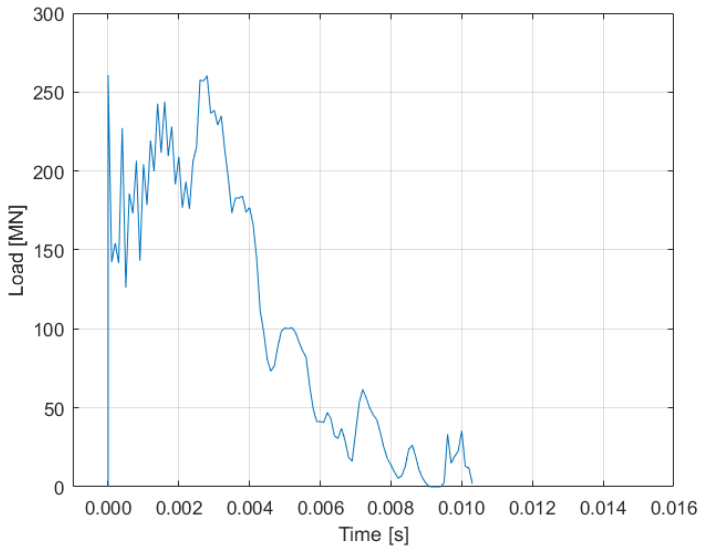

Figure 7.1: Hydraulic hammer MENCK MHU3500 impact pulse acting on a monopile with a top diameter of 6.5 m.

7.2.2. MATERIAL DAMPING

Rayleigh beta damping was applied to the material properties of the monopile. This damping coefficient was determined according to the criteria provided in the ANSYS manual (ANSYS, 2017) and is formulated in Equation 7.1.

$$\beta_{damp} = \frac{2 \cdot \xi}{2 \cdot \pi \cdot f_e} \tag{7.1}$$

Where

- ξ is the damping ratio of steel equal to 0.24 %. This is typically used at Van Oord for S355 steel
- f_e is the first eigen-frequency of the monopile

Modal analyses was performed for a monopile with a length equal to 78.5 m and a reached target penetration depth of 29.25 m. It should be noticed that the material damping was determined for a embedded depth of 29.25 m, and due to the time scope of the project (read lack of simulation time), was not corrected to 10.0 m depth. It is however expected that this does not influence the results significantly. It is recommended to investigate material damping and its effect on the results more thoroughly in future studies. Axial- and lateral soil support was included as well for the outside and inside of the monopile. Results of the modal analyses are shown in Table 7.1. A plot of the first and third modal modes is included in the Appendix, Figure E.12a and E.12b respectively. According to Van Oord these frequencies are higher than what they obtained for monopiles at the Borssele 3 and 4 parks. The higher values can be explained by that fact that changes in thickness and diameter along the pile were neglected, resulting in a stiffer pile. Also a uniform medium-dense sand profile was modelled which differs from a realistic soil profile and this influences the natural frequency as well.

Table 7.1: Modal analyses results for a 78.5 m monopile embedded 29.25 m in a medium-dense sand layer

Mode number [-]	**Frequency [Hz]**
1	2.2104
2	2.2104
3	2.7474

Substituting the first eigen-frequency value into Equation 7.1 this results in a β value equal to 0.00035. This damping value was added to the S355 steel properties used in the dynamic FEM model.

7.2.3. TRANSIENT EFFECTS

To help ANSYS solve this dynamic run, first contact was initiated slightly. The model should be stable before the pulse is transferred to the pile. This means that transient effects should be dampened out before applying the pulse. The material Beta damping estimated in the previous section was applied to the model. In 1.00 second the boulder was vertically displaced 0.10 mm, after which the boulder was fixed and the transient analyses was continued to inspect inertia effects. A node on the monopile in the contact area was selected and its axial displacement is seen in Figure 7.2a. Here it is seen that during the first second the node is displaced vertically linear after which the boulder was fixed and therefore the monopile does not displace any further (flat line). Zooming in on this flat line, Figure 7.2b was obtained. Looking at the numbers it was seen that there are no initial transients effect. The small perturbations might be caused by numerical effects and due to its small values are assumed not to be important. By performing a run without damping, and with very large damping, similar plots were obtained which confirms that the damping does not effect this initial response and this is another confirmation that there are no transient effects. The lack of transient effects might be caused by the fact that the boulder is displaced a very small amount (0.10 mm) in 1.00 s. Since there are no obvious interfering transient effects the hammer pulse might be applied to the model.

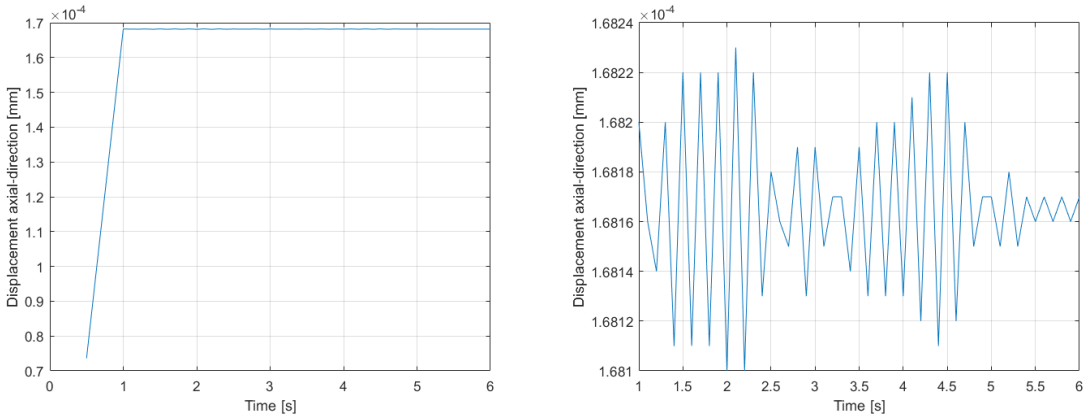

(a) (b)

Figure 7.2: (a) Axial displacement of a node in the contact area of the pile versus the time. From 0.0 to 1.0 s the pile-boulder contact is initiated and from 1.0 to 6.0 s the boulder's movement is fixed. (b) Zoomed in axial displacement after initiating contact with the boulder (after 1.0 s).

7.2.4. SOIL MODELLING

To run a dynamic case, the lateral and axial soil support, in- and outside the pile, was included as was done before in the static model. Soil damping is neglected which is conservative and estimating realistic damping values is out of the scope of this project.

7.2.5. TIME STEPS

The pulse is defined on time steps equal to 1.0 ms. If one models larger time steps, the FEM model will skip information that is present in the impact pulse and you are likely to lose important information in the pulse. Furthermore, the time step can be too large to give the structure enough time to respond to the pulse (inertia effects). Too small time steps however requires a lot of computation time and storage. Therefore the influence of the time step should be checked and this is done in the result section below.
According to Equation 2.2, the wave travels through steel at a speed of approximately 5172 m/s. This means that for the 78.5 m long monopile used in this research study, the wave takes approximately $\frac{78.5}{5172} \approx 0.015$ s to travel from the top to the bottom of the monopile. As the pulse last 0.01 s, at 0.025 the end of the pulse has reached the tip of the monopile. To investigate the effect of the pulse on the pile tip, the end of the pulse should pass the tip complete, therefore approximately 0.030 seconds should be an appropriate time domain to investigate dynamic behaviour of the stress wave running down and up the monopile.

Furthermore, since the pulse duration is 0.01 s and the wave velocity equals 5172 m/s, this results into a wavelength equal to $\frac{5172}{100} = 51.7$ m. This length of the pile should be enough to capture the dynamics of the first blow of the hammer. However, the entire pile length of 78.5 m was modelled to clearly visualize the wave running down and up the monopile.

7.3. RESULTS

The time step-size was checked by running a simulation with the time step-size equal to 1.0 ms and 0.1 ms. The first generated a file around 200 GB and the latter over 300 GB. This approaches the storage and computational time limit appropriate for this thesis. Unfortunately the results of the latter run were not correctly saved and therefore no plots of the displacement and stress were included in this report. The stresses and displacements were however checked before saving and the values matched, which indicates that 1.0 ms is small enough time step-size to use in this analyses.

The dynamic simulation was first investigated by looking at the vertical stress component in the pile. A plot of the vertical stress component with increasing time in seen in Figure 7.3, 7.4, and 7.5. The wave pulse running down, reflecting at the bottom and running up again is clearly visible. It should be noticed that the applied pulse starts at 1.0 s, since during the first 1.0 s the boulder was displaced vertically 0.10 mm to initiate contact as was discussed above. This also explains the stress already present in the pile. First, in Figure 7.3a the front

of the pulse defined in Figure 7.1 has started running down 1 ms from the top of the pile. After 9 ms (Figure 7.3b) the pulse continues running down. 9 ms is slightly smaller than the 0.01 s duration of the pulse wave and this means that the entire pulse is almost applied to the top of the pile. Looking at the colors in the pulse in Figure 7.3b, the light blue represent the maximum stress. It is seen that the light blue intervals match with the force peaks shown in Figure 7.1. This is better demonstrated by plotting the pulse next to the color plot as shown in the Appendix, Figure E.14a. Furthermore, by visually inspecting the light blue vertical peak stress values in the pile, the stress is approximately 150 MPa. This matches the peak force of 250 MN (Figure 7.1) divided by the area of approximately 1.7 $m^2 \approx 147$ MPa. Both the shape and values of the pulse on the pile verifies that the pulse was correctly applied in the dynamic run. In Figure 7.4a the front of the impact pulse at 14 ms is close to the pile tip. The stress pulse has almost reached the tip at approximately 0.015 s. This matches the estimated travel time of the pulse as was shown before by dividing the length of the pile by the wave speed.

In Figure 7.4b the front of the wave started to reflect from the tip and continues its way to the top showed at 24 ms and 30 ms in Figure 7.5. It is important to distinguish compression and tension waves to understand what actually happens in this dynamic simulation. When the pulse is running down (e.g. Figure 7.4a), the green-blue color legends show a negative stress sign. This means that a compression wave runs down, as expected. At 18 ms (Figure 7.4b) the front of the wave is reflected mainly as a tension wave showed by the yellow positive color contour. This is explained by the fact that apart from the boulder, there is no tip resistance at the pile. However, at the location on the pile wall where the pile interacts with the boulder, the reflective wave is in compression. This reflective compression wave caused by the boulder is seen by the small green colour contour at the tip at 18 ms in Figure 7.4b and is better visible by the green color contour at the pile tip after 24 ms and 30 ms in Figure 7.5.

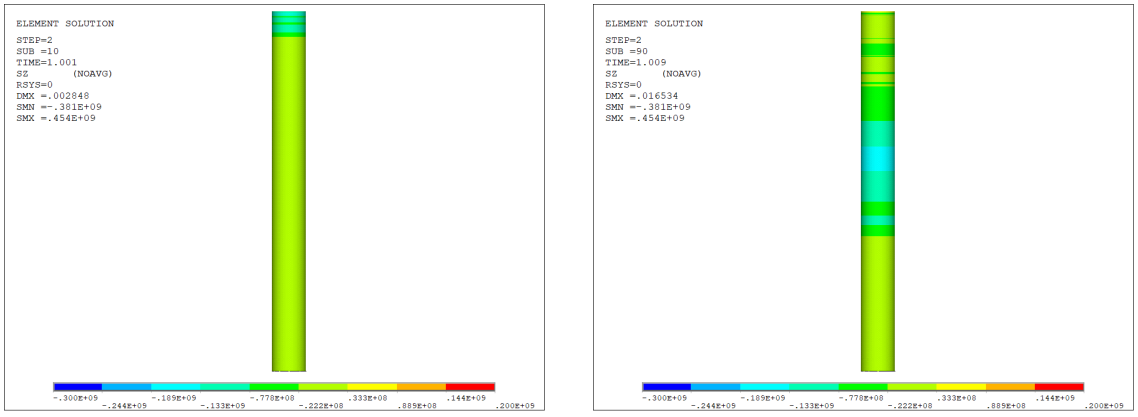

(a) 0.001 s (b) 0.009 s

Figure 7.3: Vertical stress in the monopile after 0.001 s (a) and 0.009 s (b).

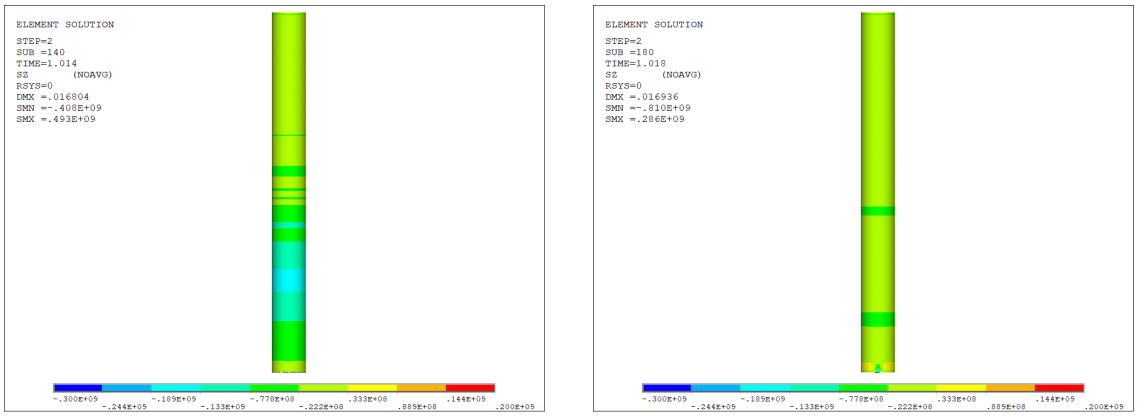

(a) 0.014 s (b) 0.018 s

Figure 7.4: Vertical stress in the monopile after 0.014 s (a) and 0.018 s (b).

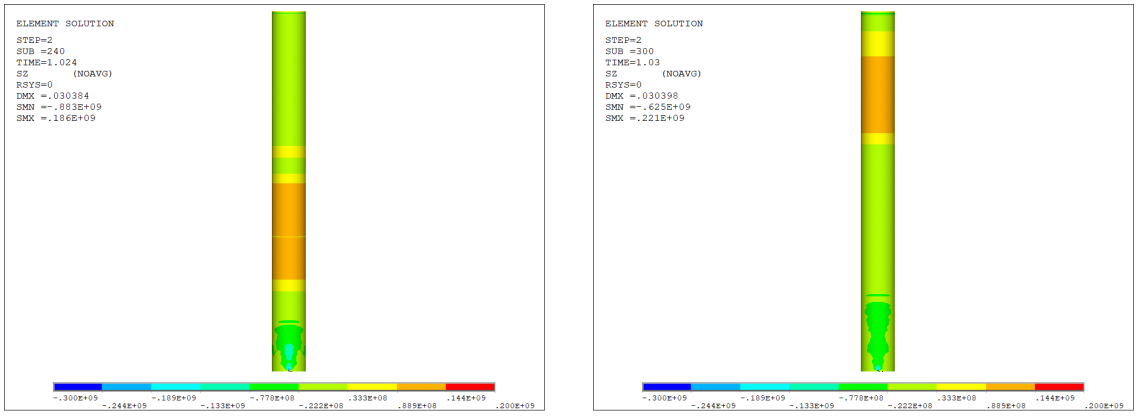

(a) 0.024 s (b) 0.030 s

Figure 7.5: Vertical stress in the monopile after 0.024 s (a) and 0.030 s (b).

The reflective compression stress is of interest to compare the dynamic simulation to the static one. A plot of the vertical reaction load on the boulder is presented in Figure 7.6. The first 15 ms there is no reaction load on the boulder since the impact pulse did not reach the pile tip yet. At approximately 15 ms the pulse reached the tip of the pile and this is visible in the plot by the increased vertical reaction load on the boulder. The reaction load reaches a peak at 22 ms and a maximum peak of 14.9 MN at approximately 25 ms. This double peak is also shown in the input pulse signal shown in Figure 7.1. After 25 ms the reaction force decreases since the peak of the pulse is reflected and on its way back to the top of the pile. Comparing the load values on the vertical axis with the applied force values in Figure 7.1 it is seen that only a fraction, less than 10 percent, of the force is transmitted to the boulder.

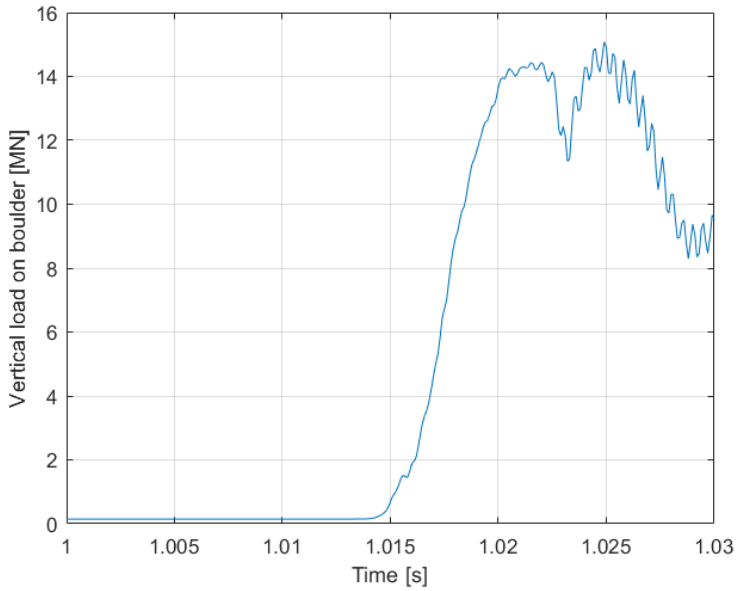

Figure 7.6: Vertical reaction load on the boulder versus the time.

The maximum load on the boulder at the 25 ms peak equals 14.9 MN. This reaction load on the boulder was then matched with the reaction force on the boulder (hence independent of the axial soil springs) in the static model, using the same input parameters. Results of the radial displacement in 3D and a view from the bottom of the pile are shown in Figure 7.7 for the dynamic run. For the static run this is displaced in Figure 7.8. The deformations are scaled by a factor three for visualization purpose. Comparing Figure 7.7 and 7.8 it is first of all obtained that the deformed shape at the pile-boulder interaction looks similar but the dynamic case looks less deformed. In the static run a larger area seemed to be deformed (red cheek), whereas the dynamic deformation seems more local. This is expected since in the static model the entire structure finds static equilibrium and in the dynamic model the structure does not have time to respond to global deformations. It was previously obtained that in the dynamic model less than 10 percent of the wave actually hits the boulder. For the static model, all the force applied at the top is transferred to the boulder (except the axial soil springs). The difference in static and dynamic structure response is shown well looking at the rotation of the op of the 79.5 m modelled pile. Previous chapter it was shown that the entire pile rotates due to static analyses. In the performed dynamic simulation it is seen that the top of the pile barely rotates (1.4 mm, Appendix Figure E.14b).

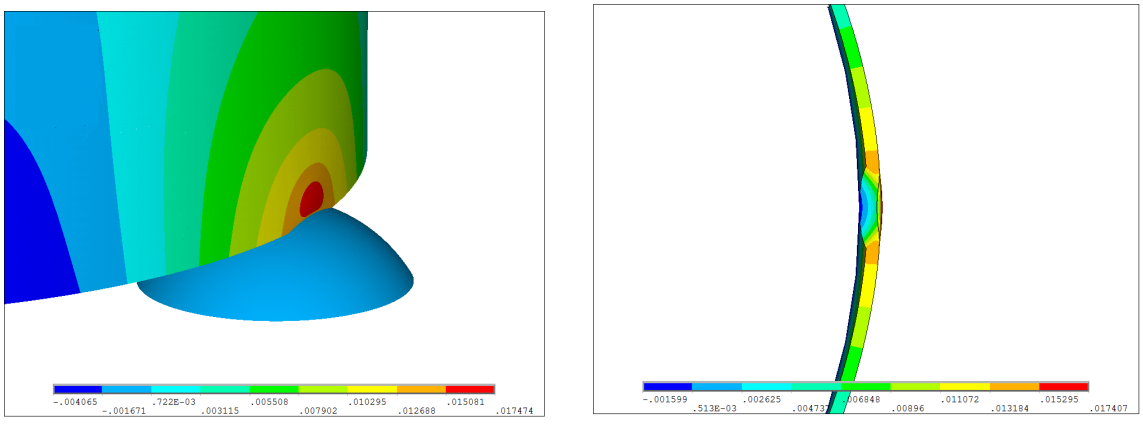

(a) (b)

Figure 7.7: (a) 3D plot of the local deformation. (b) Bottom view of the local deformation. (a) and (b) are the results of a dynamic simulation. Deformations are scale by a factor 3.

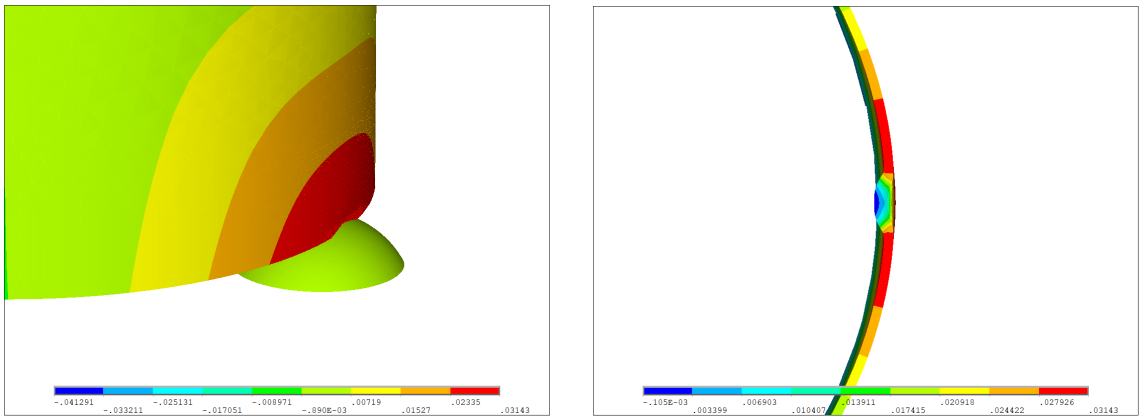

(a) (b)

Figure 7.8: (a) 3D plot of the local deformation. (b) Bottom view of the local deformation. (a) and (b) are the results of a static simulation. Deformations are scale by a factor 3.

To summarize, the dynamic and static response of the structure globally is entirely different. There are however to many uncertainties in the dynamic simulation to compare the static and dynamic case based on a single run. Locally, the deformed shapes look similar. The focus of this MSc thesis was to identify the causes and mechanism of local deformation at the pile tip. Since the deformed shapes of the static and dynamic analyses are similar, the different causes and failure mechanism seem possible to be calculated on a static approach. However, for more realistic and usable values in the industry, dynamic analyses should be performed. This is recommended to perform in future studies.

8

CONCLUSIONS AND FURTHER RESEARCH

8.1. DISCUSSION

In this research several modelling decisions were made based on a trade-off between modelling accuracy, scope- and focus of this MSc thesis. Many aspects were discussed in the report. Several points that require additional discussion are discussed in this section.

First of all, spherical boulders were used in order to specify the research. In reality boulders consist of different shapes (as was seen in Figure 2.8) and these shapes might influence the pile-boulder interaction. It is therefore recommended to performs simulations on a variety of boulder shapes. Different boulder shapes might however result in the same pile-boulder contact area considered in this report. It is therefore better to say that different contact areas should be considered.

What is not incorporated in this study are possible remedies regarding damage at the tip of the pile. As described there is no guidance for pile tip damage in the standards. In practice when driving through hard layers is expected, piles are sometimes equipped with pile shoes. This basically seals the bottom of the pile which will increase the pile tip resistance but is expected to reduce damage at the tip and improve drive-ability. The National Highway Institute (2006) report that 'a conical reinforced point should be used to prevent tip damage due to boulders'. This was out of the scope of this research, however might be a solution when severe pile-damage is suspected. Also the thickness of toe section is usually increased to prevent damage while driving. In reality piles also differ in diameter and thickness over the length of the pile and these irregular geometries were not considered in this research. These geometrical effects are suspected to influence the results significantly and is therefore recommended to incorporate to obtain more realistic values. When these geometric variations are incorporated in the model, also the depth of the boulder should be investigated. Global buckling did not occur in performed analyses, however might become a problem when a large obstacle or rock layer is encountered in shallow depths. The depth of the boulder is linked with the strength of the soil and better soil models should be included to obtain more realistic results. This is recommended to perform in further studies.

Another discussion point is modelling the soil. In this research a uniform medium-dense sand profile was used. Different soil characteristics influence the magnitude of pile tip damage as was seen in this study and more realistic soil profiles should be incorporated to obtain more realistic output that can be of use in industry. What is more, the method that was used to apply the soil to the model should be improved. Applying non-linear Winkler springs raises questions about its accuracy. P-y curves are often derived by integrating the normal stress distribution after the pile was displaced by a certain amount. This is true for smooth piles, but in reality piles are not smooth which results into shear stresses due to wall friction. The assumption made in this report assumes that the shear stresses are much smaller than the normal stresses so the shear stresses are neglected. This is an assumption which is usually made in p-y application. However, neglecting the shear effects might lead to an underestimated soil stiffness and it is recommended to check the error of neglecting these effects. Shear effects can be obtained by for example modelling the soil in a FE model in Plaxis 3D as was done in the MSc thesis by J. Velarde, (J. Velarde, 2006). Application of p-y curves is questionable regarding the kind of small-displacement studies since they are arrived for large deformations. Discrete uncoupled

springs are not a very good option for local deformation analysis unless you know the deformation pattern in advance. This is because the spring stiffness depends on the dimensions of the deformed shape. In general it would be better to model the soil using volume elements. Also, in this research the spring stiffnesses were generated according to the API-RP-2-GEO. This standard is valid for small diameter piles and the stiffness values should be corrected for large diameter piles. This is recommended to incorporate to improve the model. Concerning the lateral soil stiffness inside the pile, it was shown that including this support reduces local pile tip buckling and the global stability of the pile. The stiffness of the lateral soil support inside the pile was determined at 29.25 m depth. For more accurate results, it is recommended to vary this stiffness with depth. Finally, it is recommended to also take tip bearing resistance (e.g Q-z curves) by the soil into account at the part of the pile tip that is not covered by the boulder. The soil here will absorb part of the applied load to the pile, and this will likely reduce the force resultant acting on the pile and therefore reduce deformation at the tip.

The splitting resistance of rock was determined using the Brazilian test criteria. This is valid for cylinders under compression for low load rates. For larger boulders, a crack might be introduced that propagates after several blows. Crack propagation is a challenging task to investigate and might be interesting to investigate in future research. Displacing the boulder vertically can be approximated by bearing capacity formulations as was described in Chapter 3. The displacement of the boulder into the soil is however a dynamic process. After a hammer blow the resistance of the soil under the boulder might increase resulting in less movement of the boulder the next blow. Since the focus of the research is on the initiation of local deformation, the boulder was vertically constraint in this research.

It is important to notice that the stress results from GRLWEAP are rough estimations. GRLWEAP is a 1D program and for large diameter piles the results might be inaccurate since dispersion effects are neglected. The results were purely outputted as a way to link the research to drive-ability analyses. The dynamic FEM analyses should also be improved since several dynamic aspects were neglected. First, dynamic material effects were not taken into account. The strain-rate effects of steel are recommended to incorporate into the model. Furthermore, soil damping was conservatively neglected since incorporating soil damping will reduce the stresses at the pile tip. Realistic soil damping is very difficult to determine and is a whole field of research on its own. Also only one single dynamic case was ran and therefore the results are not well substantiated as is discussed in more detail in Section 7.

Performed research and the numerical model that was created is highly theoretical. Self-verification was done multiple times by performing test-runs as described in Chapter 4. Also the first linear buckling results and contact stresses were verified using existing theories. More complex results were not verified or validated since these results do not exist. Naturally this should be done and it is necessary to verify the results with other models or validate results possibly by experiments.

8.2. CONCLUSION

A numerical model was designed and a parametric study was performed to investigated the effect of several parameters on local pile tip deformation. It was shown that a fully non-linear model, using six solid elements over the thickness was required to establish accurate pile-boulder behaviour. It was shown that axial soil support does not influence the initial local deformation and that lateral soil support is necessary to capture local deformation.

Local tip deformation caused by the boulder was shown to be dominant compared to the deformation due to fabrication imperfections. A safety factor of 1.1 is recommended to include pile fabrication imperfections. Furthermore, it was shown that both the diameter and thickness influence pile tip damage, and that the thickness dominates this influence. This means that the D/t ratio cannot be used as a single design parameter as is often assumed, and that both D and t should be individually taken into account. This also shows that current design standards mentioning minimum D/t ratio's when hard driving is expected, are outdated or non-existent. It was also seen that the larger the size of the contact area, the better the force is distributed over the pile and this reduces the deformation. The size is however limited to a 2.0 m diameter boulder size. Larger boulders are not likely to be encountered offshore. When the position of the boulder was such that asymmetric interaction between the pile and the boulder was established, lower friction values resulted in a decrease in applied load to cause sliding of the pile's wall over the boulder's surface. A friction coefficient of 0.3 was chosen as an appropriate friction value to clarify different deformation mechanisms. It was shown that if $\alpha_{contact} > +10°$ (the contact angle between the pile and the boulder, positive is the boulder positioned outside the pile and negative inside the pile), the wall deforms locally inwards (local ovalisation) at the contact zone and the pile tends to slide over the boulder's surface, $-10° \leq \alpha_{contact} \leq +10°$ leads to local rippling of the wall and when $\alpha_{contact} < -10°$ the wall locally deforms outwards (local ovalisation) due to the pile sliding over the boulder's surface. Larger angles ($\alpha_{contact} < -10°$ and $\alpha_{contact} > +10°$) resulted in larger horizontal reaction forces on the boulder, pushing the boulder into the soil. Pushing the boulder away resulted in reduced damage to the pile tip. For designing wind-farms at locations where boulders might be encountered, small pile-boulder angles are therefore more relevant to take into design consideration. Pile drive-ability analyses in GRLWEAP showed that current typical offshore hammers can easily deliver the amount of force needed to initiate local deformation on the pile tip.

Relating pile tip damage to failure of the boulder showed that the pile is likely to cause local failure at the boulder's surface for soft rocks (sandstone), however the pile is unlikely to penetrate into harder rocks such as granite. Splitting the boulder is not likely to occur for the considered 2.0 m diameter boulder. It was nevertheless shown that smaller boulders are more prone to splitting. Splitting the boulder is beneficial considered to pile tip damage and this highlights the important of having prior knowledge of the boulder's shape and size, before installation of the pile.

This research was finished performing only a single dynamic simulation since thorough dynamic analyses was not the focus and out of the scope of the MSc thesis. Since just one dynamic run was performed these statements made in the report are not well substantiated, but should be seen as a start for a dynamic approach to the problem, which can be done in future studies. Comparing the dynamic to the static simulation showed that statically the global response of the structure is larger than for the dynamic simulation. In the dynamic simulation the entire structure does not have enough time to respond to global deformations. The local deformation shape at the tip looks similar for the static and dynamic simulation and therefore it seems possible to investigate failure mechanism based on static equilibrium. However, to obtain more realistic and usable values for the industry, dynamic analyses should be performed. Also propagation of the damage should be investigated using dynamic simulations and this is recommended to perform in future studies.

8.3. FURTHER RESEARCH

The research topic had to be constraint due to the complexity of the research and the many aspects connected to the research. Due to the constrained topic, several highly interesting aspects of pile-boulder interaction are still to be researched and the model that was designed can be improved. This potential research is likely to effect the performed research significantly since it is directly linked to the performed research. Several of these research topics are mentioned here. These might be follow-up MSc thesis projects or even PHD research work.

First and perhaps following-up on this thesis research, the dynamics should be investigated in detail to link the driving process to dynamic pile behaviour and its influence on pile tip damage. As was mentioned, only one dynamic run was performed and therefore well substantiated conclusions could not be made. The dynamic simulation method described in Chapter 7 should might be used as a start to investigate the dynamics in further research. The damage propagation is then interesting to relate to the total stability of the monopile. Perhaps simulations with shorter (deformed) piles can be performed to check the deformation limits on fatigue and ULS load cases. It is also important to relate the embedment depth of the boulder to the deformation since this obviously influences the damage size and possible propagation of the damage. It is however difficult to capture large deformation propagation in ANSYS or other FEM packages and therefore this research is a very challenging one. Results of this static model is important to take into account when investigating the dynamics. Combinations of friction values and pile-boulder contact angles are important to consider in the dynamic simulations since they result in different failure mechanisms. One should also think about crack development when deformation propagation is investigated since it was shown that in several cases the fracture limit was exceeded.

Second, the accuracy of the static model established in this MSc thesis can be significantly improved. These improvements can also be included when the research is continued focusing on dynamic analyses. Geometric variations over the length of the pile should be included. Geometrical or even material variations of the bottom can of the pile are then interesting to investigate for its influence on pile tip damage. Moreover, in this research a very simplistic uniform soil profile was assumed and hence the soil modelling can of course be improved. Finding accurate and fast models to model pile-soil interaction is a fascinating topic on its own. Currently a lot of research is done on this topic and the industry might benefit from using more reliable methods to model the soil than the currently frequently applied Winkler springs.

Third, failing of the boulder due to impact with the pile should be investigated in more detail. This might be done by doing FEM analyses of crack propagation in rocks and validated by experiments. The load that is necessary for certain types of rock to fail can then be compared to dynamic reaction loads on the rock caused by pile driving. As a result it might than be concluded that certain types and sizes of boulders do not form a problem when encountered in pile driving due to failure of the rock prior to damage initiation of the pile.

Finally, investigating methods to check the pile integrity during driving is another very interesting topic. Typical damage detection methods were briefly addressed in Section 2.3, however one might be able to find other ways to early detect pile damage at the pile toe in a financial affordable manner. This is also closely related to the detection of obstacles in the seabed which is not typically performed nowadays. Finding affordable ways to detect obstacles in the seabed has increasing potential since wind farms will be constructed in areas were obstacles are more likely to be present.

BIBLIOGRAPHY

AASHTO (2010), LRFD Bridge Design Specifications, Technical report, American Association of State Highway and Transportation Officials, 5th edition, Washington DC.

Aldridge, T.R., Carrington, T.M., Kee, N.R. (2005), *Propagation of pile tip damage during installation, in Proceedings of the International Symposium on Frontiers in Offshore Geotechnics*, Perth, Australia.

Alm, T., Snell, R.O., Hampson, K.M., Olaussen, A. (2004), Design and installation of the valhall piggyback structures, Offshore Technology Conference, Houston, Texas, U.S.A.

Amadei, B. (2015), 'Introduction to rock mechanics, lecture 8', University of Colorado.

American Petroleum Institute (2000), Recommended practice for planning, designing and constructing fixed offshore platforms–working stress design, Technical report, API Recommended Practice 2A-WSD (RP 2A-WSD), 21st Edition.

American Petroleum Institute (2011), Geotechnical and foundation design considerations, Technical report, ANSI/API Recommended Practice 2GEO.

ANSYS inc. (2017), 'ANSYS Help Viewer', Release 18.1.

Barnends, F. (1992), 'Application of stress-wave theory to piles', *Proceedings of the 14th International Conference on the Application of Stress-Wave Theory to Piles* p. 137.

Batdorf, S.B., Schildcrout, M., Stein, M. (1947), Critical stress of thin-walled cylinders in axial compression, Technical report, National Advisory Committee For Aeronautics.

Beter, B., Butcher, A., Holmes, R., Howard, J., Lewis, M., Musso, R. (2002), North sea geology, Technical report, British Geological Survey.

Bewick, R.P., Amann, F., Kaser, p.K., Martin, C.D. (2015), Interpretation of ucs test results for engineering design, The 13th International Congress of Rock Mechanics.

Cathie Associates (2017), Geological and geotechnical causes of pile tip buckling, Future Offshore Foundations.

Cathie Associates SA/NV (2015), Opile, integrated solutions for single pile analysis, Technical report.

Cohen, K.M., Gibbard, P.L., Weerts, H.J.T. (2014), 'North sea palaeogeographical reconstructions for the last 1 ma', *Netherlands Journal of Geosciences* **93**, 7–29.

Das, B.M. (2011), *Principles of Foundation Engineering*, 7th edn, Cengage Learning, Stamford, USA.

Das, B.M. (2016), *Principles of Foundation Engineering*, 8th edn, Cengage Learning, Stamford, USA.

Deeks, A.J., Randolph, M.F. (1993), 'Analytical modelling of hammer impact for pile driving', *International journal for numerical and analytical methods en geomechanics* **17**, 279–302.

Defense Nuclear Agency (1976), Measurements of dynamic friction between rock and steel, Technical report, Systems, Science and Software.

Det Norske Veritas AS, Germanischer Lloyd SE (2015), Fabrication and testing of offshore structures, Technical report, DNVGL-OS-C401.

Det Norske Veritas AS, Germanischer Lloyd SE (2016), Determination of structural capacity by non-linear finite element analysis methods, Technical report, DNVGL-RP-C208.

Erbrich, C.T., Barbosa-Cruz, E., Barbour, R. (2011), *Soil-pile interaction during extrusion of an initially deformed pile, in Frontiers in Offshore Geotechnics II*, Taylor and Francis Group, London.

Florida Department of Transportation (2014), Embedded data collectors.

Hoving, J. (2017), 'Lecture notes in the course bottom founded structures, lecture 12', TU Delft.

HSE (2001), A study of pile fatigue during driving and in-service and of pile tip integrity, Technical report, Prepared by MSL Engineering Limited for the Health and Safety Executive.

Jørgen Amdahl (2005), 'Tmr4205 - buckling and ultimate strength of marine structures', NTNU.

Laban, C., Van der Meer, J.J.M. (2011), 'Pleistocene glaciation in the netherlands', *Developments in Quaternary Science* **15**, 247–260.

Landvik, J.Y., Brook, E.J., Gualtieri, L., Linge, H., Raisnback, G., Salvigsen, O. (2012), 'Be exposure age constraints on the late weichselian ice-sheet geometry and dynamics in inter-ice-stream areas, western svalbard', *BOREAS* **42**, 43–56.

Likins, G., M.ASCE, P.E., Rausche, F. (2014), Pile damage prevention and assessment using dynamic monitoring and the beta method, Geo-Congress 2014, Atlanta, Georgia.

London, U. C. (2018), 'Earth materials - lecture 13', Technical presentation.

Long, J.H., Hendrix, J., Jaromin, D. (2009), Comparison of Five Different Methods for Determining Pile Bearing Capacities, Technical report, Wisconsin Department of Transportation.

Metrikine, A.V., Vrouwenvelder, A.C.W.M. (2017), 'Dynamics of structures – ct4140, part 2 - wave dynamics', TU Delft.

Nederlandse Norm (2016), Geotechnisch ontwerp van constructies - deel 1: Algemene regels, Technical report, NEN 9997-1:2016 nl.

Negrea, A., Predoi, M.V. (2012), 'The elastic contact of a sphere with an elastic half-space, a comparison between analytic and finite elements solutions', *University Politehnica of Bucharest Science Bulletin* **74**.

Palmstrom, A., Singh, R. (2011), 'The deformation modulus of rock masses-comparisons between in situ tests and indirect estimates', *Tunnelling and Underground Space Technology* **16**, 115–131.

Pando, A. (2013), 'Lecture notes in analyses of lateral loaded piles with p-y curves - observations on the effect of pile flexural stiffness and cyclic loading', UNC Charlotte.

Pile Dynamics Inc. (2000), 'CAPWAP: Case Pile Wave Analysis Program', Users Manual, PDI, U.S.A.

Pile Dynamics Inc (2010), 'GRLWEAP', Version 2-2-2020.

Pile Dynamics Inc. (2017), 'Pile Driving Analyzer', PDA-8G Brochure.

Prandtl, L. (1921), 'Über die eindringen festigkeit (härte) plastischer baustoffe und die festigkeit von schneide', *Zeitschrift fur Angewandte Mathematik und Mechanik* **1**(1), 15–20.

Rausche, F. (2013), The case method and the pile driving analyzer, Pile Dynamics, Inc, Houston, Texas, U.S.A.

Rausche, F., Goble, G.G. (1979), 'Determination of pile damage by top measurements', *American Society for Testing an Materials* pp. 500–507.

Rausche, F., Liang, L., Allin, R.C., Rancman, D. (2017), 'Application and correlations of the wave equation analysis program grlweap', Pile Dynamics Inc.

Sitharam, T. (2013), Advanced foundation engineering, Technical report, Indian Institute of Science.

Smith, E. (1960), 'Pile driving analysis by the wave equation', *Journal of the Soil Mechanics and Foundations Division* **86**.

Subsea, P. (2016), 'Sounding out risk for offshore installations', Technical presentation.

Terzaghi, K. (1943), 'Theoretical soil mechanics', *Wiley*.

The European Union (2006), Eurocode 3: Design of steel structures - part 1-5: General rules - plated structural elements, Technical report, EN 1993-1-5.

The European Union (2007), Eurocode 3: Design of steel structures - part 1-6: Strength and stability of shell structures, Technical report, EN 1993-1-6.

Tollmien, W., Schlichting, H., Görtler H., Riegels, F.W. (1961), *Über die Eindringungsfestigkeit (Härte) plastischer Baustoffe und die Festigkeit von Schneiden. In: Riegels F.W. (eds) Ludwig Prandtl Gesammelte Abhandlungen*, Springer, Berlin, Heidelberg.

United States Department of Agriculture (2012), Engineering classification of rock materials, Technical report.

Velarde, J. (2006), Design of Monopile Foundations to Support the DTU 10 MW Offshore Wind Turbine, MSc thesis, DTU, NTNU, TU Delft.

Verbeek, G.E.H., Goble, G. G. (2012), 'Re-evaluation of the method to determine pile damage using the Beta Method', Allnamics.

Verruit. A., van Baars, S. (n.d.).

Vulcan Iron Work Inc. (2017), 'Wave Equation Analysis'.
URL: *https://vulcanhammer.info/blog/page/2/*

Warrington, D.C., Wynn, R.H. (2000), 'Comparison of numerical methods to closed form solution for wave equation analysis of piles, internet edition', Published online at The Wave Equation Page for Piling.

A

- PILE DRIVING BACKGROUND

A.1. DERIVATION OF THE WAVE EQUATION

Consider a straight, prismatic rod as shown in Figure A.4(a). The co-ordinate x refers to a cross-section of the rod, while the longitudinal displacement of this section is given by $u(x,t)$. We presume the rod to be under a dynamically varying stress field $\sigma(x,t)$, so that adjacent sections are subjected to varying stresses. A body force $q(x,t)$ is also assumed present.

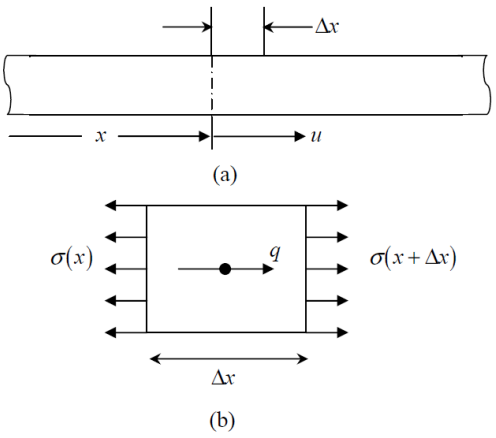

Figure A.1: A thin rod (a) with co-ordinate x and displacement u of a section and (b) the stresses acting on element Δx of the rod.

With these assumptions the equation of the rod motion in the $x-$ direction reads:

$$-\sigma(x)A+\sigma(x+\Delta x)A+qA\Delta x=\rho A\Delta x\frac{\partial^2 u}{\partial t^2} \tag{A.1}$$

Where ρ is the mass density of the rod material and A is the cross-sectional area of the rod. The latter is a constant in this development, since we are considering a prismatic rod. We note that tensile stress is assumed positive. By taking into account the following Taylor expansion of $\sigma(x+\Delta x)$

$$\sigma(x+\Delta x)\approx\sigma(x)+\frac{\partial\sigma}{\partial x}\Delta x \tag{A.2}$$

Equation A.1 reduces to:

$$\frac{\partial\sigma}{\partial x}+q=\rho\frac{\partial^2 u}{\partial t^2} \tag{A.3}$$

Substituting Hooke's law into Equation A.3 and assuming homogeneity, we obtain:

$$E\frac{\partial^2 u}{\partial x^2}+q=\frac{\partial^2 u}{\partial t^2} \tag{A.4}$$

In the absence of body forces, this Equation reduces to the wave equation:

$$\frac{\partial^2 u}{\partial x^2} = \frac{1}{c}\frac{\partial^2 u}{\partial t^2} \tag{A.5}$$

A.2. GRLWEAP DRIVEABILITY REFUSAL EXAMPLE

Table A.1: Hammer and pile properties

	Description	Value	Unit
Hammer	Type	MENCK MHU3000S	
		Direct drive, no cushion	
	Ram Weight	1647.52	kN
	Energy	3005.65	kJ/kW
	Efficiency	0.950	[-]
	Stroke	1.82	m
Steel pile	Length	36.0	m
	Diameter	5.00	m
	Wall thickness	5.55	cm
	Penetration	35.0	m
	Youngs modulus	210	GPa

Table A.2: Soil properties consisting of two layers

	Description	Value	Unit
Layer 1	Type	Medium sand	
	Depth	0.0-30.0	m
	Unit weigth	19.0	kN/m^3
	Toe and skin quake	2.540	mm
	Skin damping	0.164	s/m
	Toe damping	0.490	s/m
Layer 2	Type	Hard cohesive	
	Depth	30.0-35.0	m
	Unit weigth	26.5	kN/m^3
	Undrained shear strength	30.0	MPa
	Toe and skin quake	2.540	mm
	Skin damping	0.656	s/m
	Toe damping	0.490	s/m

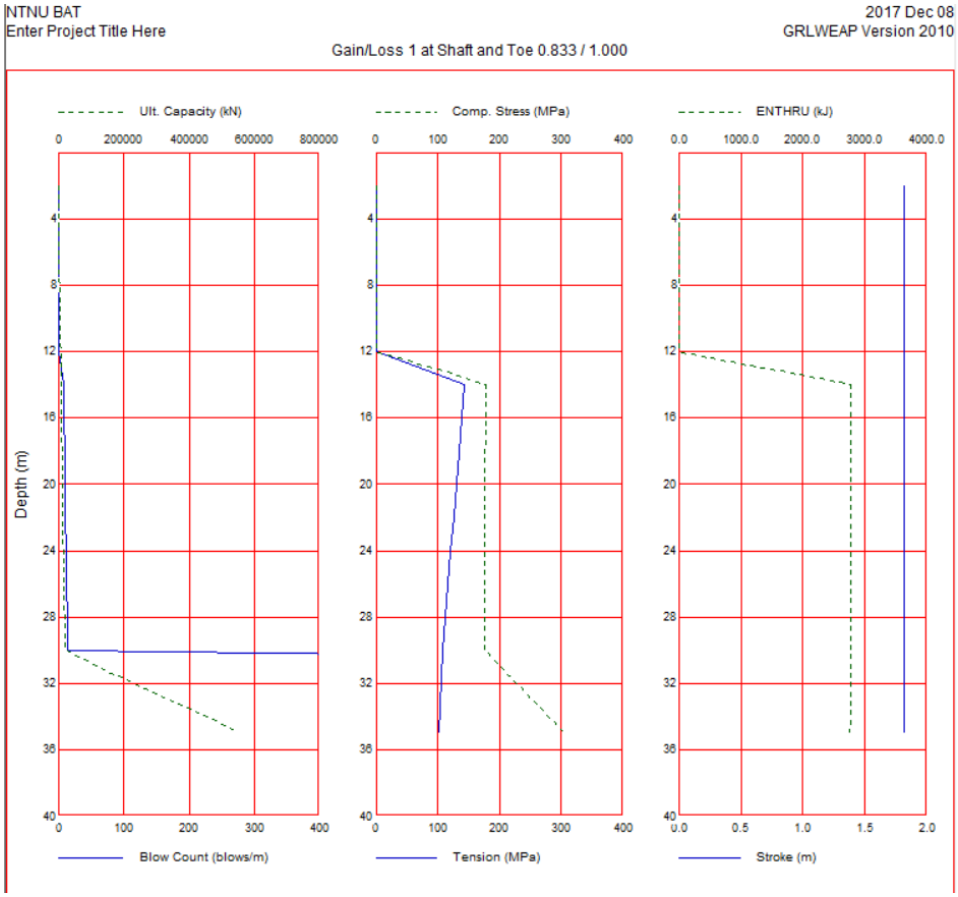

Figure A.2: Driveability analyses output from GRLWEAP

NTNU BAT
Enter Project Title Here

2017 Dec 08
GRLWEAP Version 2010

Gain/Loss 1 at Shaft and Toe 0.833 / 1.000

Depth m	Ultimate Capacity kN	Friction kN	End Bearing kN	Blow Count blows/m	Comp. Stress MPa	Tension Stress MPa	Stroke m	ENTHRU kJ
2.0	346.2	71.0	275.2	0.0	0.000	0.000	1.82	0.0
4.0	834.4	284.0	550.4	0.0	0.000	0.000	1.82	0.0
6.0	1464.6	639.0	825.6	0.0	0.000	0.000	1.82	0.0
8.0	2236.8	1136.1	1100.8	0.0	0.000	0.000	1.82	0.0
10.0	3151.0	1775.1	1375.9	0.0	0.000	0.000	1.82	0.0
12.0	4207.2	2556.1	1651.1	0.0	0.000	0.000	1.82	0.0
14.0	5405.5	3479.2	1926.3	7.6	177.320	-142.731	1.82	2768.3
16.0	6745.7	4544.2	2201.5	8.1	177.202	-138.919	1.82	2768.5
18.0	8228.0	5751.3	2476.7	8.6	176.966	-134.878	1.82	2768.7
20.0	9852.2	7100.3	2751.9	9.3	176.950	-130.621	1.82	2768.7
22.0	11618.5	8591.4	3027.1	10.0	176.943	-126.191	1.82	2768.8
24.0	13526.7	10224.5	3302.3	10.8	176.926	-121.594	1.82	2768.7
26.0	15577.0	11999.5	3577.5	11.8	176.875	-116.912	1.82	2768.6
28.0	17769.3	13916.6	3852.6	12.9	176.847	-112.348	1.82	2768.2
30.0	20103.5	15975.7	4127.8	14.1	176.764	-107.935	1.82	2767.6
30.0	20103.5	15975.7	4127.8	14.1	176.764	-107.935	1.82	2767.6
35.0	562977.1	330206.1	232771.0	9999.0	305.966	-101.854	1.82	2754.6

Refusal occurred; no driving time output possible

Figure A.3: Driveability analyses output from GRLWEAP

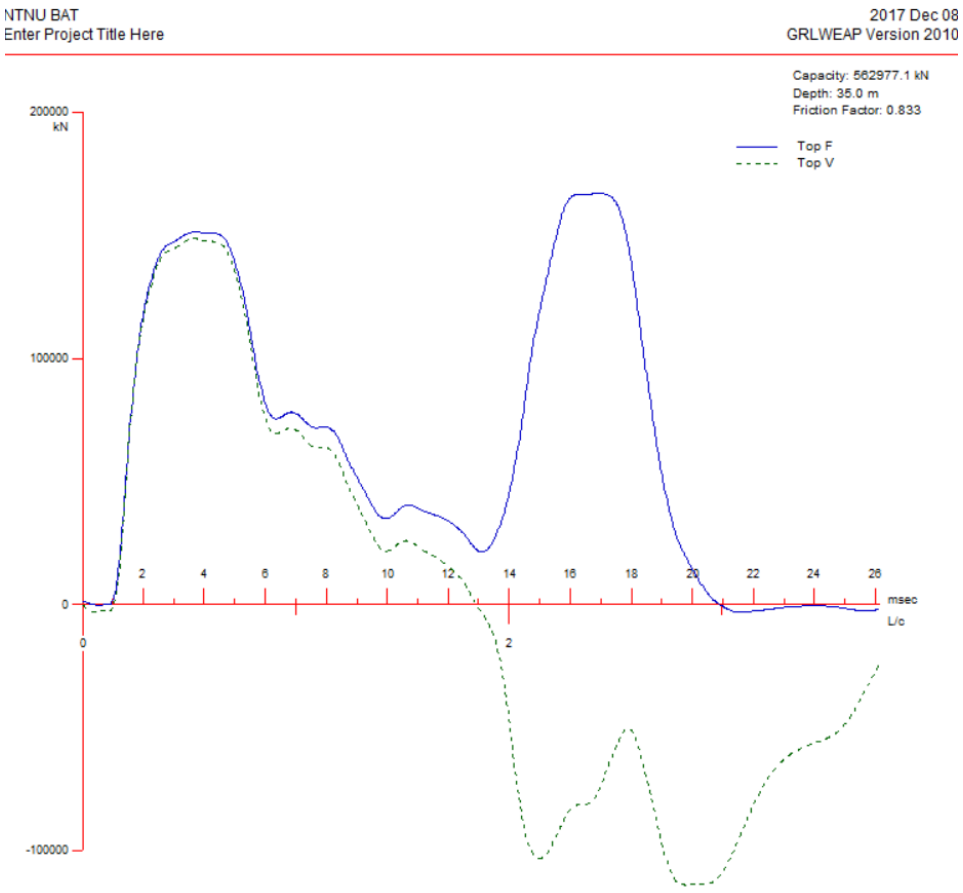

Figure A.4: Force and velocity time trace for the final blow. From driveability analyses in GRLWEAP

A.3. PILE DYNAMIC ANALYSES

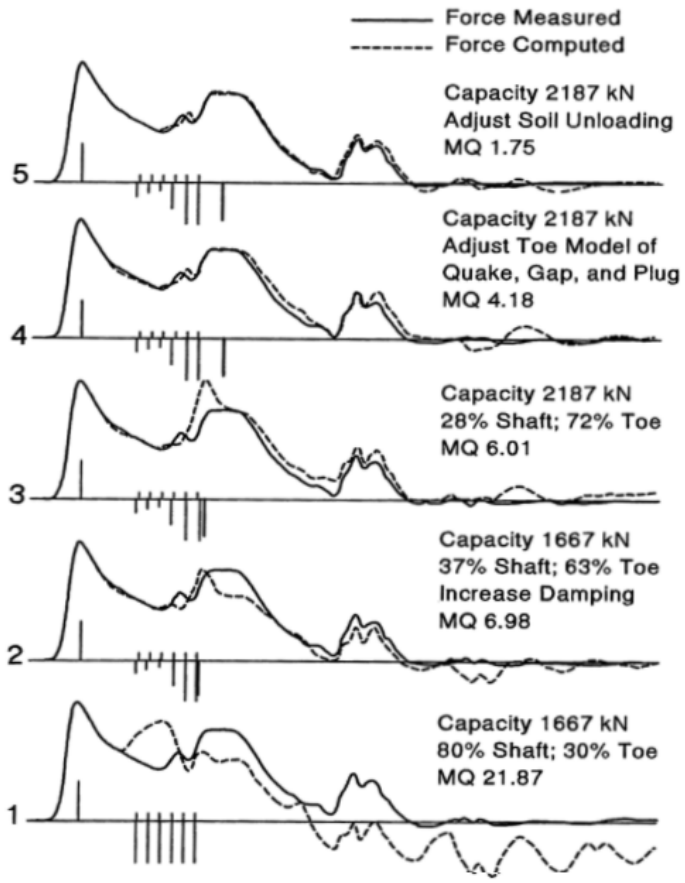

Figure A.5: CAPWAP signal matching, from bottom to top (Vulcan Iron Work Inc., 2017)

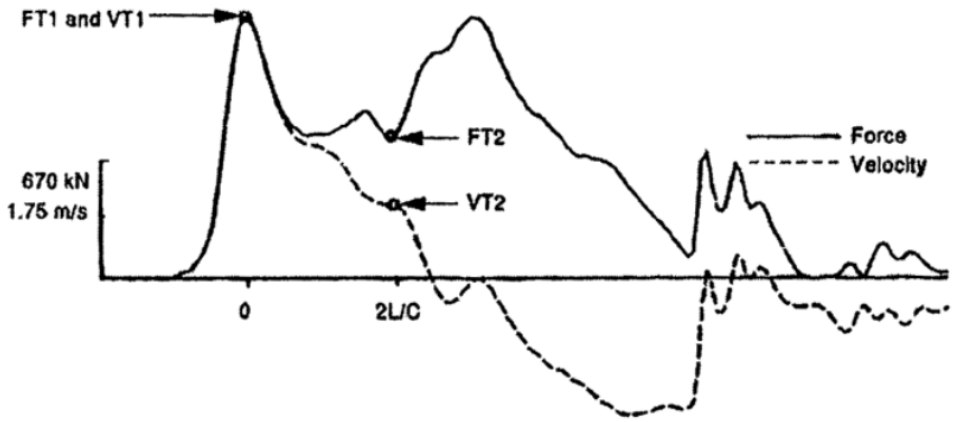

Figure A.6: The Case Method, RSP (Vulcan Iron Work Inc., 2017)

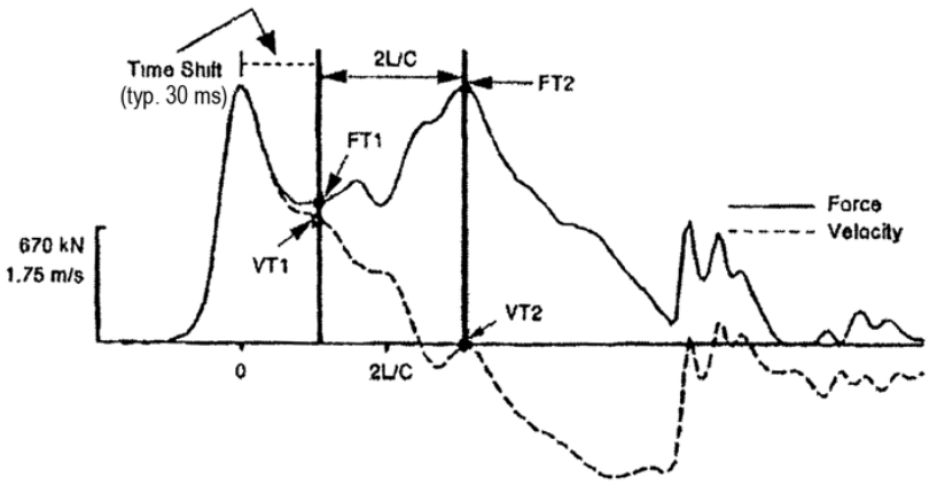

Figure A.7: The Case Method, RMX (Vulcan Iron Work Inc., 2017)

B

- DATA

B.1. STRESS STRAIN DATA

S355

Thickness [mm]	t≤ 16	16< t ≤ 40	40< t ≤ 63	63< t ≤ 100
E [N/mm^2]	210000	210000	210000	210000
σ_{prop} [N/mm^2]	320	311	301.9	284
σ_{yield} [N/mm^2]	357	346.9	336.9	316.7
σ_{yield2} [N/mm^2]	366.1	355.9	345.7	323.8
ε_{p_y1}	0.004	0.004	0.004	0.004
ε_{p_y2}	0.015	0.015	0.015	0.015
K [N/mm^2]	740	740	725	725
n	0.166	0.166	0.166	0.166

$$\sigma = K\left(\varepsilon_p + \left(\frac{\sigma_{yield\,2}}{K}\right)^{\frac{1}{n}} - \varepsilon_{p\_y2}\right)^n \quad for \quad \varepsilon_p > \varepsilon_{p\_y2}$$

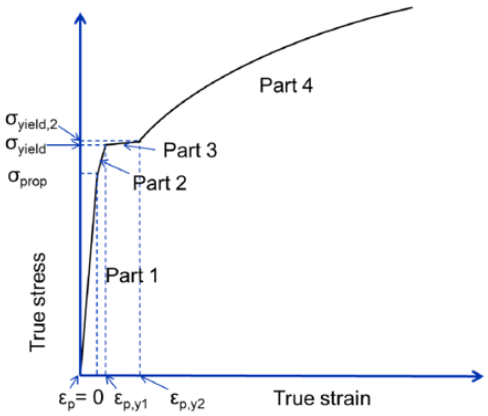

Figure B.1: S355-Steel stress-strain data (DNV-RP-C208, 2016)

C

- SOIL CHARACTERISTICS

P-y, Q-z, and T-z curves are generated for a uniform sand profile according to the American Petroleum Institute standard (API-RP-2-GEO, 2011). The approach to generate these curves is described briefly.

C.1. P-Y CURVES

The API-RP-2-GEO distinguish the ultimate lateral bearing capacity for shallow- (p_{us}) and deep (p_{ud}) foundations as is seen in Equation C.1 and C.2 respectively.

$$p_{us} = (C_1 \cdot z + C_2 \cdot D) y' z \tag{C.1}$$

$$p_{ud} = C_3 D y' z \tag{C.2}$$

Where:

- p_u is the ultimate lateral resistance at depth z [kN/m]
- y' is the submerged unit weight [kN/m^3]
- z is the depth below the original seafloor [m]
- ϕ is the angle of internal friction of sand [°]
- D is the pile outer diameter [m]
- C_1, C_2, C_3 are the coefficients determined as follows as function of ϕ [-]

$$C_1 = \frac{(\tan\beta)^2 \tan\alpha}{\tan(\beta-\phi)} + K_0 \cdot \left(\frac{\tan\phi \cdot \tan\beta}{\cos\alpha \cdot \tan(\beta-\phi)} + \tan\beta \cdot (\tan\phi \sin\beta - \tan\alpha)\right) \tag{C.3}$$

$$C_2 = \frac{\tan\beta}{\tan(\beta-\phi)} - K_a \tag{C.4}$$

$$C_3 = K_a \cdot ((\tan\beta)^8 - 1) + K_0 \cdot \tan\phi \cdot (\tan\beta)^4 \tag{C.5}$$

Where

- $\alpha = \frac{\phi}{2}$
- $\beta = 45 + \frac{\phi}{2}$
- $K_0 = 0.4$
- $K_a = \frac{1-\sin\phi}{1+\sin\phi}$

A plot of the ultimate lateral bearing capacity for a uniform sand layer with the data shown in Table 4.8, is seen in Figure C.1. It is mentioned in the standard that the lowest of the two lateral bearing capacities should be used. It is seen that for the considered sand layer, a depth till approximately 62 m is considered as shallow. The considered monopile has a maximum embedment depth of 35 m (yellow line) hence the shallow curve (blue line) should be used for modelling the lateral soil support.

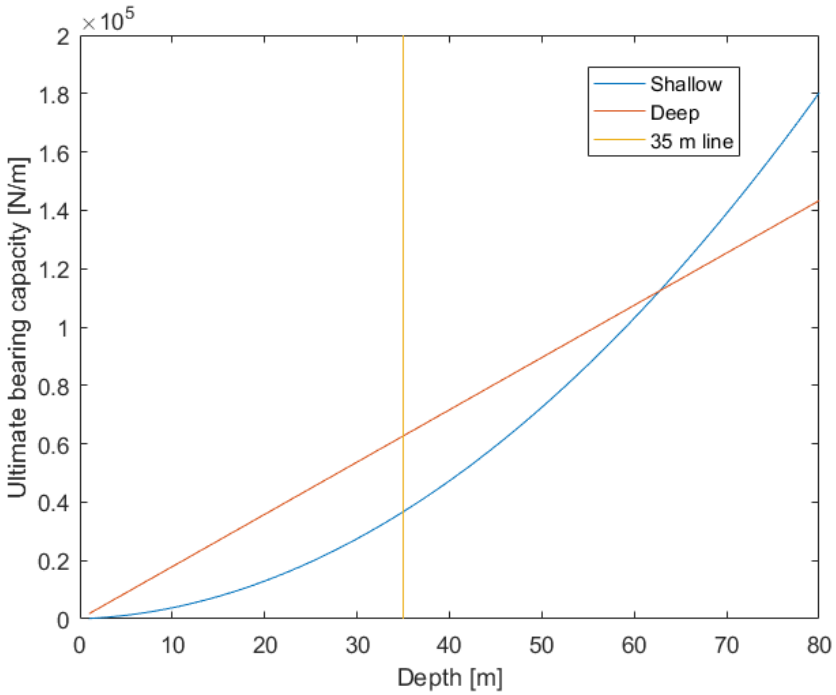

Figure C.1: Plot of the ultimate bearing capacity versus depth for shallow and deep assumptions

The lateral soil resistance-deflection relationship is shown in Equation C.6.

$$p = A \cdot p_u \cdot \tanh(\frac{k \cdot z}{A \cdot p_u} y) \tag{C.6}$$

Where:

- p is the lateral resistance of the soil [kN]
- $A = (3.0\text{-}0.8\frac{z}{D}) \leq 0.9$ for static loading [-]
- p_u is the ultimate lateral resistance per unit length at depth z [kN/m]
- k is the rate of increase with depth of initial modulus of subgrade reaction [kN/m^3]
- y is the lateral deflection at depth z [m]
- z is the depth below the original seafloor [m]

It is odd that the standard does not give any guidance on the discretization of the displacement y. Common industry practice is to discretize the displacement as a ratio of the diameter. Eight discretization steps of D/1000, D/800, D/600, D/400, D/200, D/100, D/50, and D/25 were used. A plot of the resistance-deflection curve for a medium-dense sand profile (Table 3.1) at a depth z of 0.125 m is seen in Figure C.2a. As was mentioned before, to apply the curve to the model in ANSYS, the tension part of the curve should be deleted since the springs can only be excited in compression (Figure C.2b).

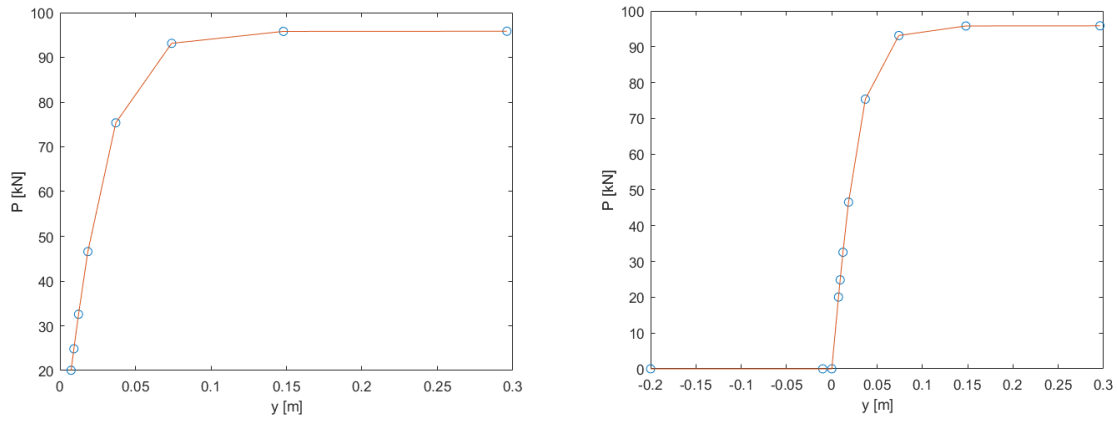

(a) (b)

Figure C.2: (a) Plot of the lateral resistance p versus the horizontal displacement y at a depth of 0.125. (b) Same curve shown as ANSYS input.

C.2. T-Z AND Q-Z CURVES

Axial shaft friction (T-z) and end bearing resistance (Q-z) curves can also be generated according to the API-RP-2-GEO. Required soil parameters for a medium-dense soil are given in the standard and are shown in Table C.1.

Table C.1: Soil data according to the American Petroleum Institute (API-RP-2-GEO, 2011)

Soil Type	**Relative density**	**Shaft friction coefficient β [-]**	**Limiting shaft friction value [kPa]**	**End bearing factor N_q [-]**	**Limiting unit end bearing values [MPa]**
Sand	Medium-dense	0.37	81	20	5

C.2.1. T-Z CURVES

The relation between the vertical displacement and the axial shaft friction according to the API-RP-2-GEO is seen in Equation C.7.

$$f(z) = \beta \cdot p_0'(z) \tag{C.7}$$

Where

- β is the dimensionless shaft friction factor [-]
- f(z) is the unit shaft friction at a given depth
- $p_0'(z)$ is the effective vertical stress at a depth z [Pa]

Recommended curve definitions are also provided by the standard as seen in Table C.2. z_{peak} is recommended to be equal to $0.01 \cdot D$. A plot of the maximum shaft friction versus the depth is shown in Figure C.3a. It is seen that at 22 m the limiting shaft friction of 81 kPa is reached. A plot of the shaft friction-deflection curve for a medium-dense sand profile (Table 3.1) at a depth z of 0.125 m is seen in Figure C.3b.

Table C.2: Axial shaft friction-displacement discretization for sand (API-RO-2-GEO, 2011)

z/z_{peak}	t/t_{max}
0.16	0.3
0.31	0.5
0.57	0.75
0.8	0.9
1	1.0
2	1.0
infinity	1.0

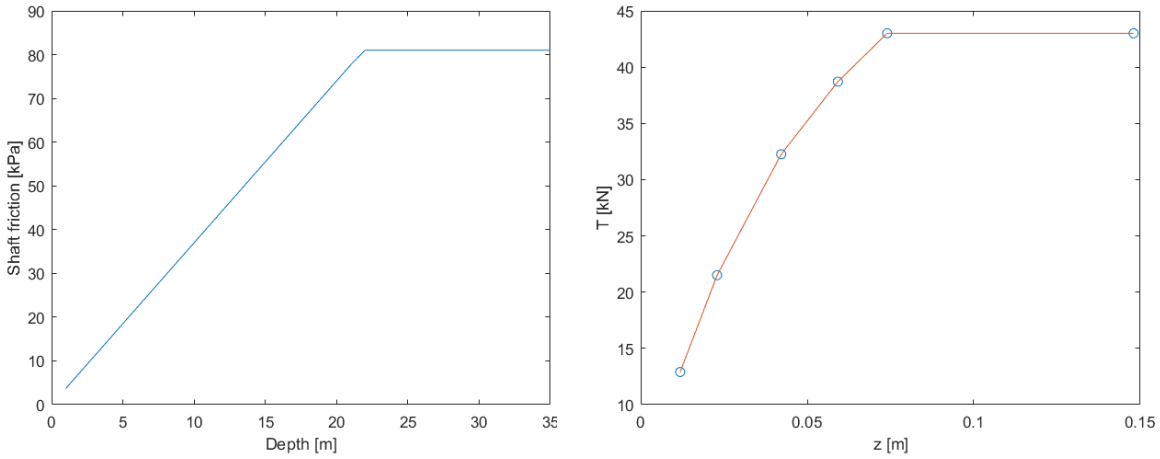

(a) (b)

Figure C.3: (a) The axial shaft friction value versus the depth. At 22 m the limiting shaft friction is reached. (b) Axial shaft friction value T versus the vertical displacement z at a depth of 0.125 m.

C.2.2. Q-Z CURVES

According to the API-RO-2-GEO, the end bearing resistance in cohensionless soils is calculated using Equation C.8.

$$q = N_q \cdot p'_{o,tip} \tag{C.8}$$

Where:

- $p'_{o,tip}$ is the effective vertical stress at the pile tip [Pa]
- N_q is the dimensionless bearing capacity factor [-]

Recommended curve definitions are shown in Table C.3.

Table C.3: Pile end bearing capacity-displacement discretization for sand (API-RO-2-GEO, 2011)

z/D	**Q/Qp**
0	0
0.002	0.25
0.013	0.50
0.042	0.75
0.073	0.90
0.100	1.00
infinite	1.00

Similar as for the P-y and T-z curves, a plot of a generated Q-z curve for a medium-dense sand soil at a depth of 0.125 m is shown in Figure C.4.

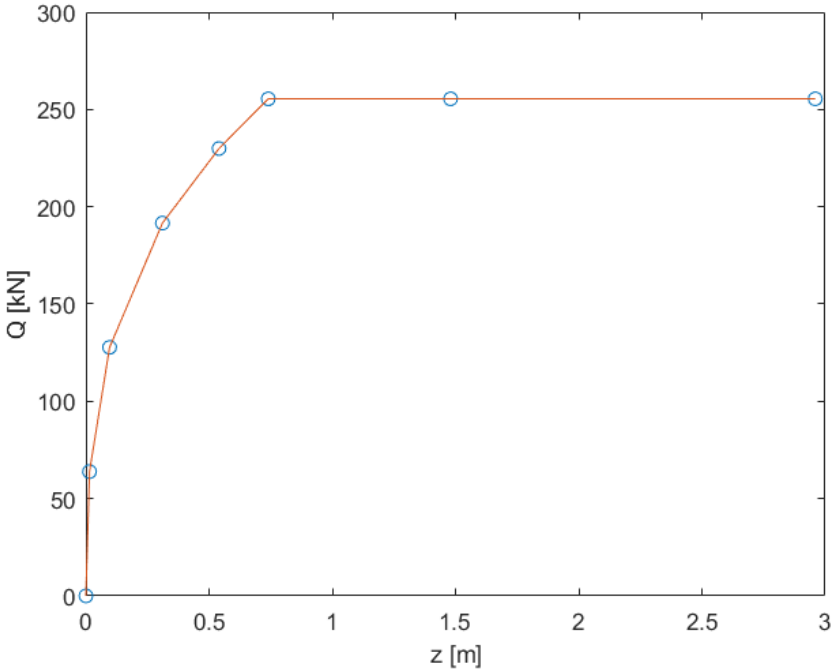

Figure C.4: Plot of the end bearing resistance Q versus the vertical displacement z at a depth of 0.125 m

D

- IMPERFECTION TOLERANCES

Detail	*Tolerance*	*Fig.*	*Comments*
Circular cylindrical shells. Local out of roundness. Local out of straightness.	Max. imperfection $\delta = \frac{0.01g}{1 + g/r}$	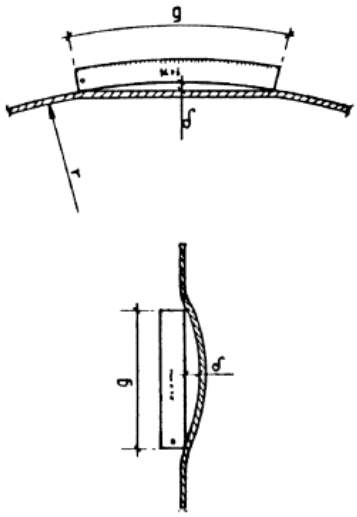	A circular template or straight rod held anywhere on the shell. g = length of template or rod. The length of the circular template shall be the smallest of: s, $1.15\sqrt{l\sqrt{rt}}$ and $\pi\frac{r}{2}$ s = stiffener spacing (of longitudinal stiffeners) l = distance between rings or bulkhead. The length of the straight rod shall be taken equal to the smallest of: l and $4\sqrt{rt}$.
Conical shells			The tolerance requirements given for cylindrical shells are applicable also for conical shells.
Circular cylindrical shells.	Max. deviation from the nominal radius measured at ring stiffener or bulkhead $\delta = (r_a - r) = 0.005\ r$		r_a = actual distance from the cylinder axis to the shell wall. r = nominal radius of the shell

Figure D.1: Imperfection tolerances according to the DNV (DNVGL-OS-C401, 2015)

E

- ANSYS PLOTS

E.1. ELEMENT OVER THICKNESS CONTACT PRESSURE

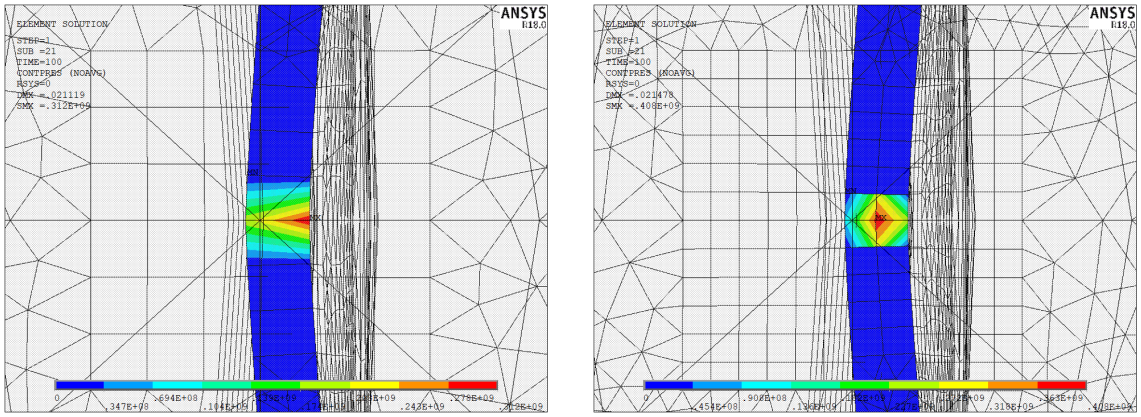

(a) 1 solid element over thickness

(b) 2 solid elements over thickness

Figure E.1: Plot of the contact pressure between monopile and boulder

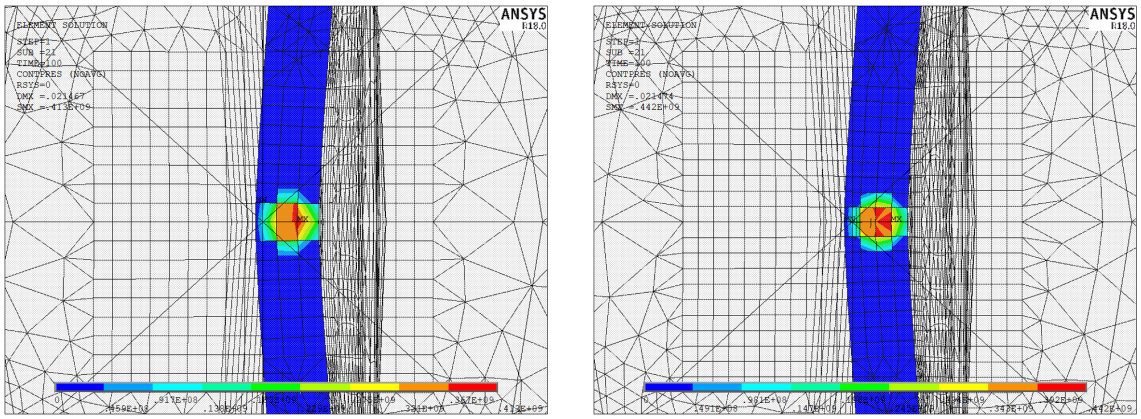

(a) 3 solid elements over thickness

(b) 4 solid elements over thickness

Figure E.2: Plot of the contact pressure between monopile and boulder

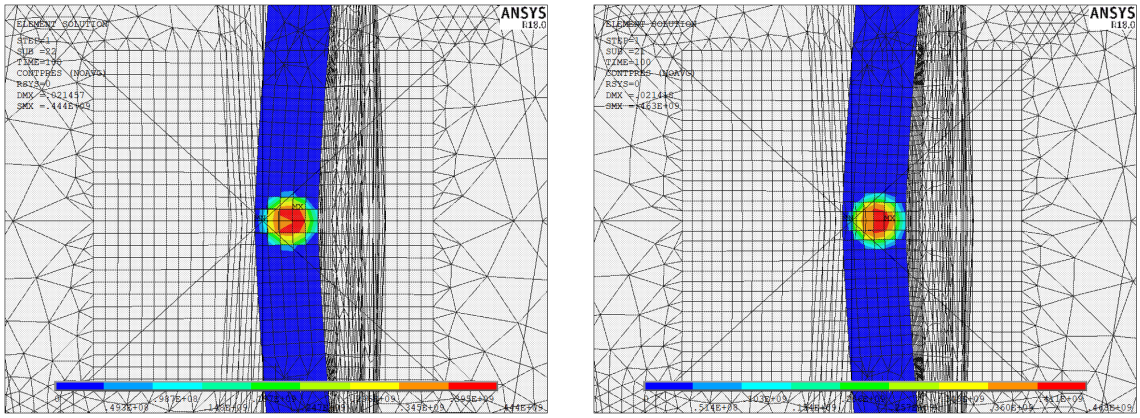

(a) 5 solid elements over thickness

(b) 6 solid elements over thickness

Figure E.3: Plot of the contact pressure between monopile and boulder

E.2. CONTACT DEFLECTS

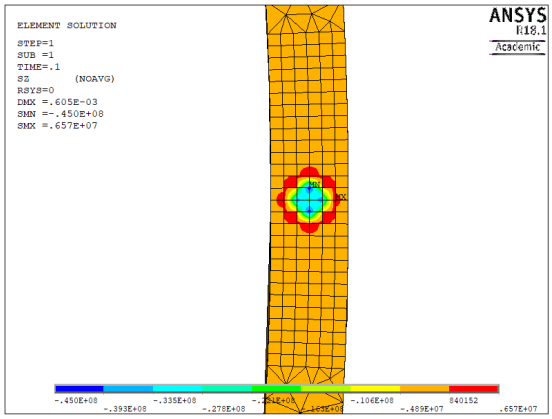

(a) At 1 percent of 25 MN applied hammer load

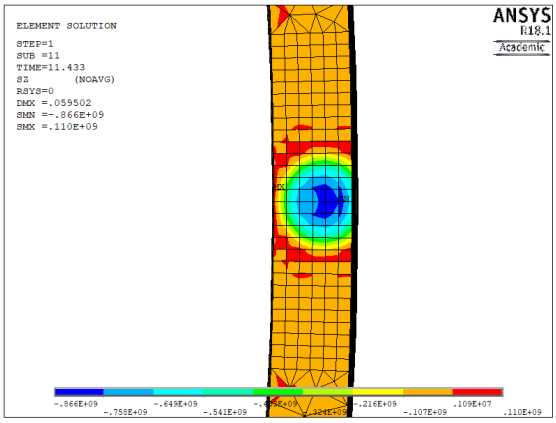

(b) At 11 percent of 25 MN applied hammer load

Figure E.4: Plot of the axial stress component at the pile tip, where pile-boulder contact is initiated. In this simulation an axial static hammer force of 25 MN was applied at the top of the pile. It is seen that the contact area moves to the outside of the wall, due to inwards deflection of the wall

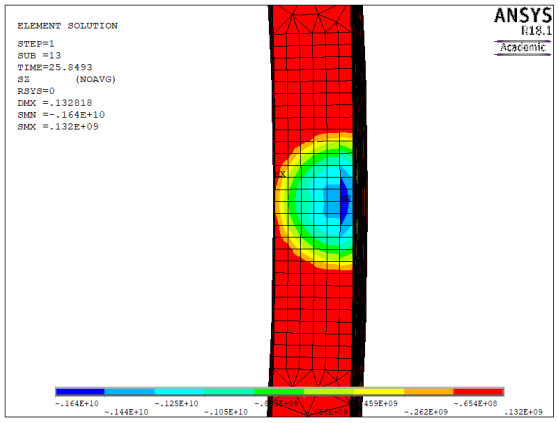

(a) At 26 percent of 25 MN applied hammer load

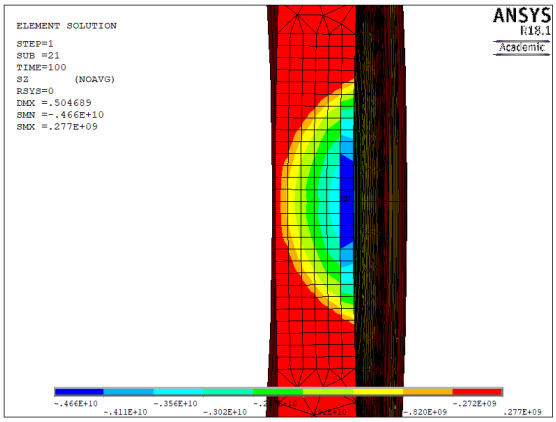

(b) At 100 percent of 25 MN applied hammer load

Figure E.5: Plot of the axial stress component at the pile tip, where pile-boulder contact is initiated. In this simulation an axial static hammer force of 25 MN was applied at the top of the pile. It is seen that the contact area moves to the outside of the wall, due to inwards deflection of the wall

E.3. BUCKLING MODES

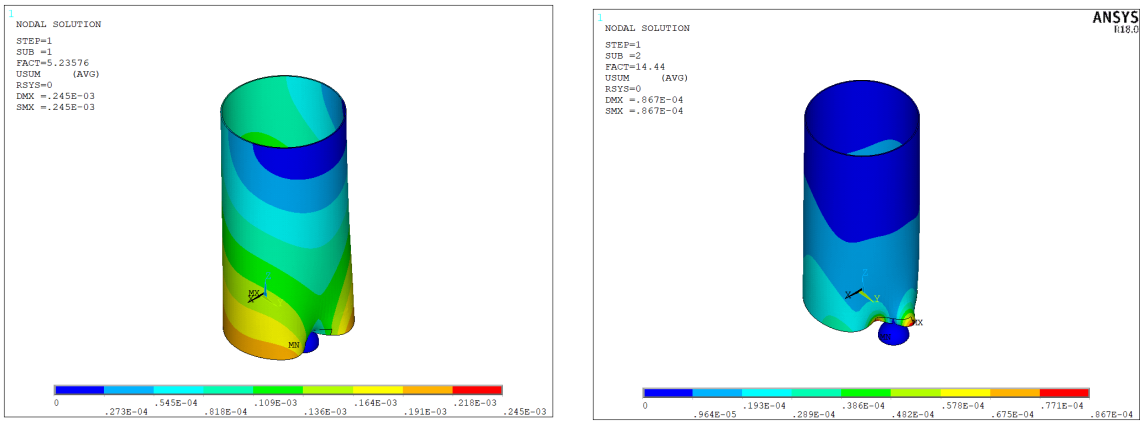

(a) First mode (b) Second mode

Figure E.6: Plot of the first (a) and second (b) buckling mode

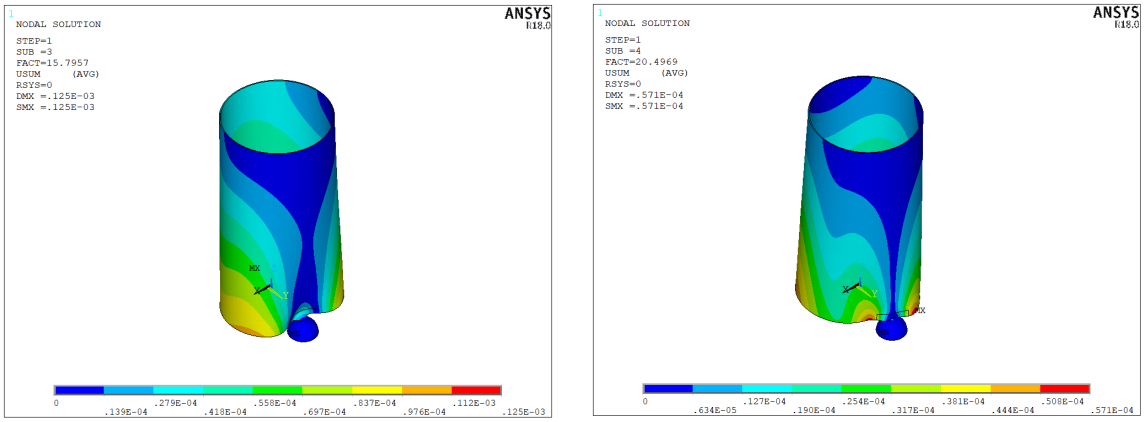

(a) Third mode (b) Fourth mode

Figure E.7: Plot of the third (a) and fourth (b) buckling mode

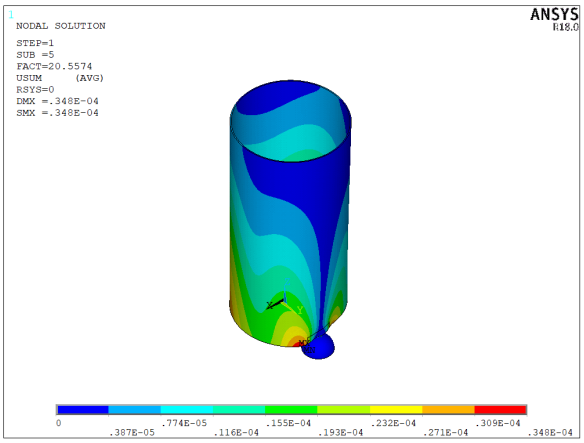

Figure E.8: Plot of the fifth buckling mode

E.4. LOCAL DISPLACEMENT INFLUENCE OF FIXED BOUNDARY CONDITION AT THE TOP

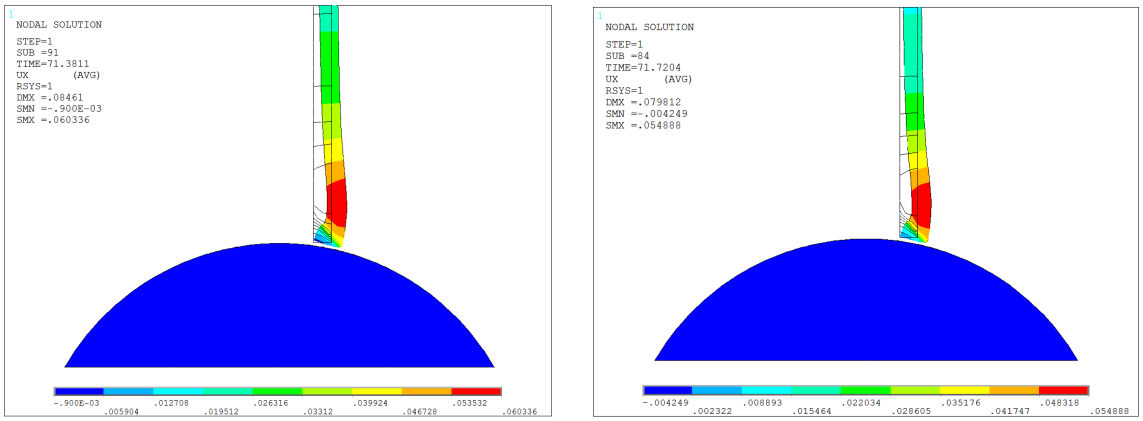

(a) (b)

Figure E.9: (a) Section-cut showing the radial displacement at the pile-boulder contact for 10.0 m modelled pile. (b) Section-cut showing the radial displacement at the pile-boulder contact for the full 78.5 m modelled pile. In (a) and (b) all other model parameters are similar (friction 0.3, $\alpha_{contact}$ = -10 °, boulder diameter = 2.0 m, and inside and outside soil support is included in radial and axial direction). The pile is fixed at the top in radial direction, hence restricting the rotation at the top of the pile.

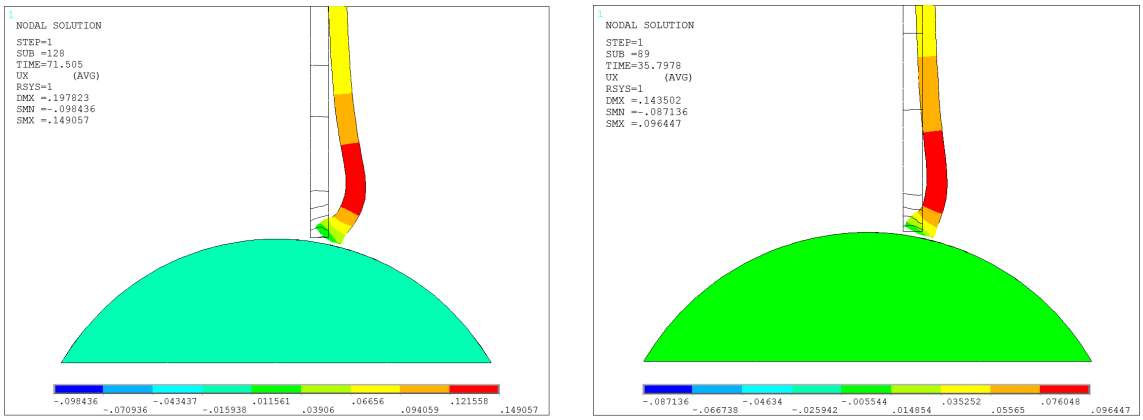

(a) (b)

Figure E.10: (a) Section-cut showing the radial displacement at the pile-boulder contact for 10.0 m modelled pile. (b) Section-cut showing the radial displacement at the pile-boulder contact for the full 78.5 m modelled pile. In (a) and (b) all other model parameters are similar (friction 0.3, $\alpha_{contact}$ = -10 °, boulder diameter = 2.0 m, and inside and outside soil support is included in radial and axial direction). The pile is free top rotate at the top of the pile.

E.5. ADDITIONAL PLOTS

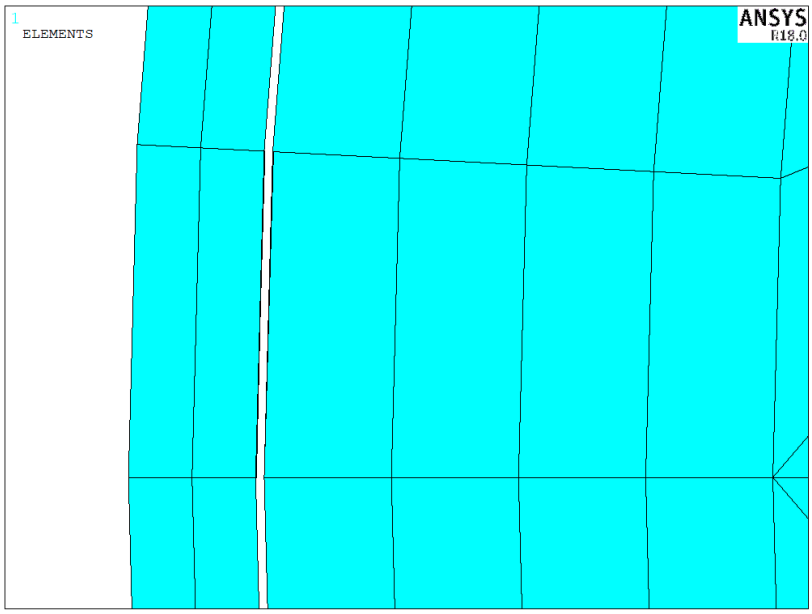

Figure E.11: Gab between the wall and soil inside the pile

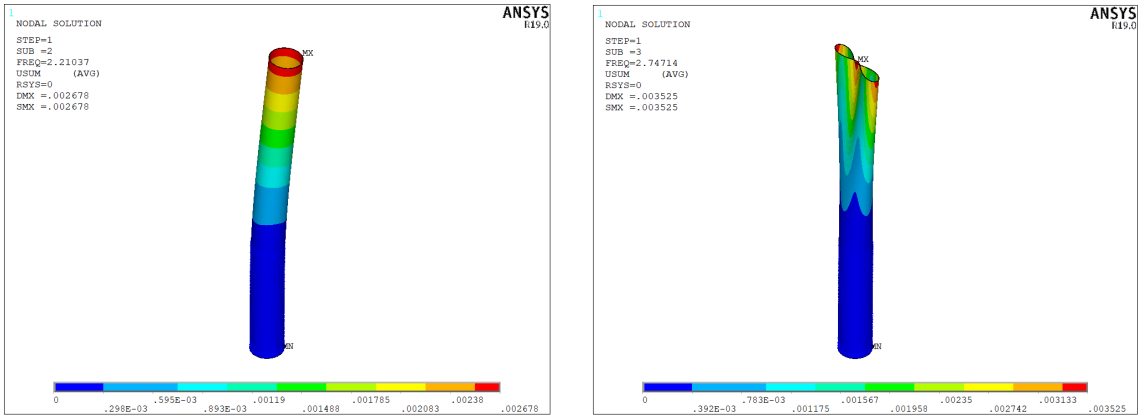

(a) First mode

(b) Third mode

Figure E.12: (a) First modal analyses mode. (b) Plot of the third modal analyses mode. In (a) and (b) the full monopile length of 78.5 m was modelled embedded in a medium-dense sand profile at a depth of 29.25 m.

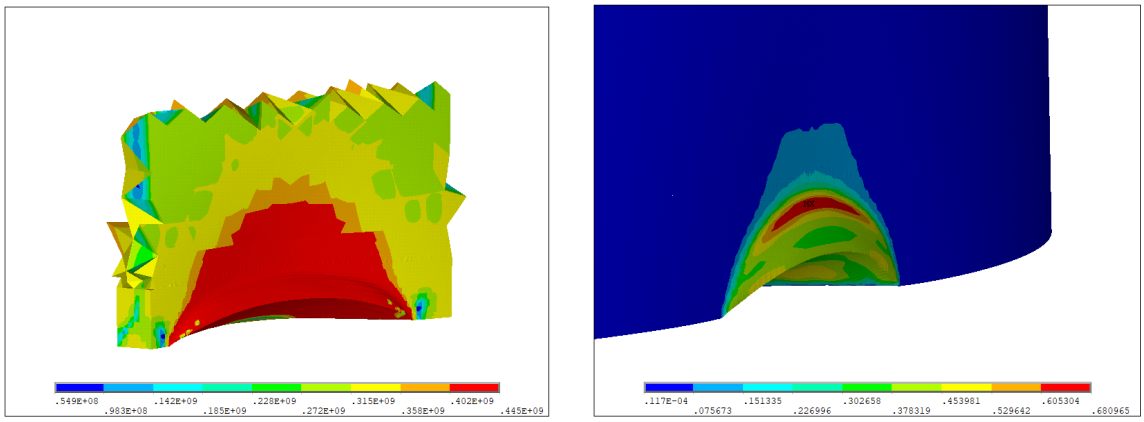

(a) Maximum stress (b) Maximum strain

Figure E.13: (a) Maximum stress in the material. (b) Maximum strain in the model. In (a) and (b) the applied load is 25.5 MN, $\alpha_{contact}$ = +20 degrees, the rock-steel friction = 0.3, model length = 10.0 m, diameter boulder is 2.0 m and lateral and axial soil support is included in the model.

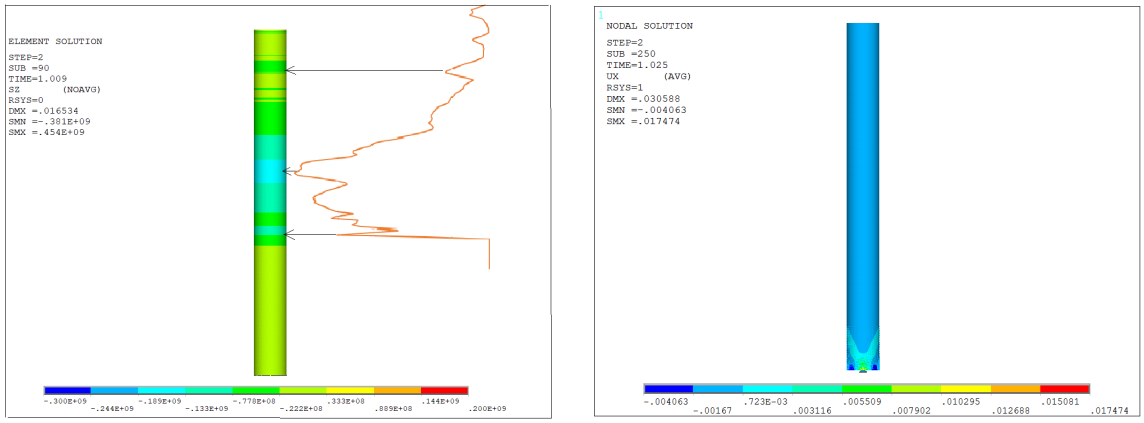

(a) (b)

Figure E.14: (a) Vertical stress in the monopile at 0.009 s, together with the pulse shape. The arrows indicate several peaks in the shape corresponding with the color peaks on the pile. (b) Radial displacement at 0.025 s for the dynamic simulation in order to check the rotation of the pile at the top